Metamorphic and geochronological constraints on the evolution of the Kalinjala Shear Zone, Eyre Peninsula

Kathleen Lane

Supervisor: Martin Hand

2011 Honours Student, Centre for Tectonics, Resources and Exploration

Geology and Geophysics, School of Earth and Environmental Sciences,

The University of Adelaide, Adelaide South Australia

ABSTRACT

In situ monazite U-Pb dating from metasedimentary rocks in the core of the crustal scale Kalinjala Shear Zone in the eastern Gawler Craton indicate that peak condition of > 9 kbar at temperatures of around 810 ºC occurred at *c.* 1700 Ma during the craton wide Kimban Orogeny. Detrital zircon ages in metasedimentary rocks that contain the peak metamorphic assemblages indicate that maximum depositional ages for rocks in the core of the shear zone were around 1780 Ma, indicating that sedimentation occurred in the interval *c.* 1780-1700 Ma. Metapelite contains an early assemblage preserved in garnet cores characterised by a kyanite-rutile association. The enclosing matrix contains a cordierite-bearing assemblage that formed during the development of the principle gneissic fabric within the shear zone and documents ~4 kbar of decompression of the shear zone core during deformation. Garnet-biotite diffusional modelling suggests that the shear zone core cooled > 50 ºCMyr^{-1} implying rapid exhumation of the core. Fe-mg garnet diffusional modelling suggests that on the flanks of the shear zone that exhumation and cooling rates were slower, and the maximum metamorphic pressures were less than in the core, suggesting that the central region of the Kalinjala Shear Zone was rapidly exhumed compared to the flanks of the shear zone. Where the shear zone reworks rocks belonging to the early Paleoproterozoic Carnot Gneiss, early formed high pressure, high temperature assemblages are overprinted by lower pressure granulite assemblages leading to the formation of secondary cordierite-spinel at the expense of garnet-sillimanite. In Mg-Al rich rocks these early assemblages include rare garnet-sillimanite-orthopyroxene assemblages which formed at the expense of early sapphirine-rutile bearing associations. The garnet-sillimanite-orthopyroxene assemblage has been overprinted by cordierite-spinel-sapphirine-biotite at *c.* 1745 Ma. This age is slightly older than

typically assigned to the Kimban Orogeny, and suggests that the event may be longer lived than previously thought. The timing of the earlier high pressure assemblage is equivocal, and could conceivably be related to the previously recognised *c.* 2450 Ma high-grade metamorphism in the Carnot Gneiss, and therefore not part of the Kimban-aged metamorphic architecture. The metamorphic constraints and age data from the core of the Kalinjala Shear Zone, combined with existing data, support a transpressional setting associated with the Kimban Orogeny. No evidence was found to support previously proposed models that include an extensional setting, or a *c.* 1850 Ma evolution of the shear system.

TABLE OF CONTENTS

INTRODUCTION

Unravelling the tectnothermal evolution of the Gawler Craton is hampered by poor outcrop exposure and a paucity of metamorphic and geochronological studies relative to the scale of the craton. In the southern Gawler Craton, the Kalinjala Shear Zone is recognised as the major structural boundary between the Archean nucleus of the craton and Paleoproterozoic domains further east. It is a generally non outcropping crustal-scale shear zone along the eastern Eyre Peninsula (Figure 1). The Kalinjala Shear Zone is interpreted to have facilitated differential exhumation and the extrusion of lower-crustal material into the mid-crust by transpression along the shear zone (Bendall 1994; Tong *et al.* 2004; Dutch 2009).

The tectonic events related to the evolution of the Kalinjala Shear Zone have been debated in a number of studies (Vassallo & Wilson 2001, 2002; Betts & Giles 2006; Payne *et al.* 2009; Fraser *et al.* 2010b; Stewart 2010). These studies have principally focussed on the structural character of the shear system, its potential significance for the construction of the eastern Gawler Craton, and its relationship to other regions in Proterozoic Australia. Despite the significance of the Kalinjala Shear Zone as a craton-scale structural element, there are limited constraints on the metamorphic conditions within the shear zone and the time and duration of deformation. For the shear zone to be placed in a consistent craton evolution model, the timing of the deformation must be comprehensively characterised. Presently the timing of deformation within the shear system is not well characterised with suggestions that it formed either at *c.* 1850 Ma (Stewart 2010) or at *c.* 1730 Ma (Betts & Giles 2006).

The aim of this study is to characterise the timing and conditions of deformation within the Kalinjala Shear Zone and immediately to the west of the shear zone. In places the shear zone is moderately well exposed, providing the opportunity to investigate its structural, metamorphic and geochronological record. Age constraints are provided by in-situ metamorphic monazite U-Pb geochronology and zircon U-Pb geochronology. These are combined with metamorphic constraints and diffusion-based garnet cooling information.

GEOLOGICAL SETTING AND PREVIOUS WORK

The Gawler Craton, southern Australia (Figure 1) consists of a late Archean to Paleoproterozoic core (Fanning *et al.* 1988; Daly & Fanning 1993; Daly *et al.* 1998; Swain *et al.* 2005a; Fanning *et al.* 2007; Hand *et al.* 2007), surrounded by Paleoproterozoic to Mesoproterozoic metasedimentary rocks and igneous suites (Fanning *et al.* 1988; Parker 1993; Daly *et al.* 1998; Ferris *et al.* 2002; Fanning *et al.* 2007). The craton preserves a protracted history of deformation, metamorphism, sedimentation and magmatism spanning approximately 1700 Myr from *c.* 3150 Ma to *c.* 1450 Ma; (Daly *et al.* 1998; Hand *et al.* 2007; Fraser *et al.* 2010a).

In the southern Gawler Craton on the Eyre Peninsula, the rocks record at least five tectonic events. These are: (1) *c.* 2480-2420 Ma Sleaford Orogeny with syn- and post-tectonic granite emplacement (Hand *et al.* 2007); (2) emplacement of granodiorititic magmas of *c.* 2000 Ma Miltalie Gneiss and Redbank Charnockite (Fanning *et al.* 1988); (3) *c.* 1850 Ma Cornian-Orogeny (Hoek & Schaefer 1998; Reid *et al.* 2008); (4) the craton-wide 1730-1690 Ma Kimban Orogeny (Payne *et al.* 2008; Dutch *et al.* 2010); and (5) *c.* 1600-1580 Ma deformation (Stewart & Betts 2010).

The oldest units belong to the late Archean to early-Paleoproterozoic (~2520-2400 Ma) Sleaford Complex (Fanning *et al.* 2007; Hand *et al.* 2007). These comprise metasedimentary lithologies, granites and felsic volcanics that form part of a larger system that comprises the core of the Gawler Craton (Swain *et al.* 2005a; Hand *et al.* 2007). The Sleaford Complex was metamorphosed at around 2480-2420 Ma during the Sleafordian Orogeny (Swain *et al.* 2005a), however the style and intensity of this metamorphic event has been obscured by later reworking associated with the development of the Kalinjala Shear system and associated structures (Vassallo & Wilson 2002; Dutch *et al.* 2008). The Sleaford Complex was intruded by felsic rocks at *c.* 2000 Ma (Miltalie Event) that were derived largely from melting of existing crust (Howard *et al.* 2009). These are interlayered with mafic dykes and sills of tholeiitic composition, that possibly in part triggered the crustal melting (Daly & Fanning 1993; Fanning 1997). Magmatic rocks associated with the Miltalie Event occur over a strike length of ~ 250 km along the western margin of the Kalinjala Shear Zone, suggesting that it may have been a larger event than generally appreciated (Fanning 1995). Although the *c.* 2000 Ma rocks are gneissic, the age of this deformation has not been established.

Unconformably overlying the Sleaford Complex and the Miltalie Gneiss are Paleoproterozoic sequences that were formerly collectively referred to as the Hutchison Group (Parker & Lemon 1982). However, recent work by Szpunar *et al.* (2011), has shown that the Hutchison Group comprises two temporally distinct packages. The older of these has been termed the Darke Peak Group, which was deposited at around 1865 Ma, and comprises quartzites, carbonates, and felsic volcanics. The volcanic rocks have a geochemical signature of enriched, alkaline,

intracontinental magmatism with A-type affinities, suggesting that the Darke Peake Group records rifting. The Darke Peak Group is stratigraphically overlain by the Cleve Group, which is a succession of dominantly psammitic and pelitic units deposited between 1780 Ma and 1730 Ma. The depositional setting of the Cleve Group is not well constrained. However the sequence contains mafic units that may have been volcanics, and has detrital zircons whose ages are consistent with derivation from the older rock systems in the southern Gawler Craton (Szpunar *et al.* 2011), suggesting that it may have been a rift setting.

To the east of this system of Archean and Paleoproterozoic rocks is the voluminous 1860-1845 Ma Donington Granitic Suite (Hoek & Schaefer 1998; Reid *et al.* 2008; Howard *et al.* 2009) which forms a domain up to 500km by 70km in extent (Fairclough & Daly 1995). The Donington Suite ranges from monzonitic to granitic in composition and has been intruded by numerous mafic dykes. Country rocks to the Donington Suite are rare. Where they do occur, metasedimentary units contain detrital zircon grains down to *c.* 1870 Ma in age (Howard 2006; Howard *et al.* 2009), suggesting that the Donington Suite intruded soon after a period of basin development.

The Donington Suite and the Neoarchean and Paleoproterozoic rocks to the west are juxtaposed by the crustal scale Kalinjala Shear Zone (Figure 1; Fairclough & Daly 1995; Hoek & Schaefer 1998; Vassallo & Wilson 2002). This belt of high-strain deformation can be geophysically traced along the extent of the eastern Eyre Peninsula (Figure 1), disappearing northward beneath the *c.* 1590 Ma Gawler Range Volcanics. Southward its apparent extension can be traced in to the East Antarctic

Shield (Dalziel 1991; Moores 1991; Zhao *et al.* 2002). Due to sparse outcrop, it is difficult to estimate the effective width of the shear zone, however in central eastern Eyre Peninsula highly strained orthogneisses of the Donington Suite form a zone ~ 4km wide, providing a minimum width estimate (Fanning 2007). On northern Eyre Peninsula the shear zone breaks up into a series of splays (Fraser *et al.* 2010a). Seismic imaging in northern Eyre Peninsula suggests this set of shear splays dip gently east into the lower crust (Fraser *et al.* 2010a). Further south, in central eastern and southern Eyre Peninsula, the shear zone is defined by a single zone of deformation. Electromagnetic imaging suggests that in this region the shear zone has a steep westerly dip to at least 20km depth (Thiel *et al.* 2005).

Previous workers have suggested that the Kalinjala Shear Zone formed as an extensional structure that accommodated deposition of the Darke Peake Group, although provided no geochronological basis for this interpretation (Stewart 2010). Fraser *et al.* (2010a), suggested that the Kalinjala Shear Zone in northern Eyre Peninsula was an extensional structure during the 1730-1690 Ma Kimban Orogeny based on the presence of high-grade *c.* 1730 Ma metamorphism west of the shear zone, and its absence to the east. However there are presently no age constraints on the timing of the northern Eyre Peninsula shear fabrics or the magnitude of apparent vertical offset on the zone. This extensional interpretation differs to that of Vassallo et al (2001), Vassallo & Wilson (2002), Hand *et al.* (2007), Dutch *et al.* (2008) and Stewart & Betts (2010), who all suggest that it was a transpressional structure during the Kimban Orogeny.

In the southern Eyre Peninsula, Vassallo and Wilson (2002) recognised two distinct periods of deformation associated with the Kimban Orogeny (and by inference the Kalinjala Shear Zone). The first, termed KD_1, led to the formation of north-verging non-cylindrical folds (Vassallo & Wilson 2002) within rocks to the west of the shear zone, and was accompanied by prograde metamorphism with peak PT estimates of 850-900 ºC and 9-10 kbar (Tong *et al.* 2004). High-grade metamorphism associated with this event is best exposed on southern Eyre Peninsula, and forms a domain approximately 35 km wide that is bounded to the west against low-grade metamorphic rocks by a N-S trending structure (Dutch *et al.* 2010). This high-grade domain appears to narrow dramatically northward, to the extent that it is no longer present in central eastern Eyre Peninsula ~ 50km to the north (Schwarz *et al.* 2002). The second phase of deformation (KD2), is interpreted to reflect east-to northeast-verging thrusts west of the Kalinjala Shear Zone, and development of the Kalinjala Shear Zone during dextral transpression (Vassallo & Wilson 2002). Tong *et al.* (2004) suggests that conditions during KD2 were 700-750 ºC and 5-6 kbar. However in all probability there would have been a continuous evolution reflected by a clockwise P-T history, and subsequently there are no distinct P-T conditions associated with KD2 (e.g. Dutch *et al.* 2010). Further north in the Port Neill region, peak metamorphic conditions in the core of the shear zone were ~ 10 kbar and 800 ºC, and bound by steep metamorphic field gradients (Dutch *et al.* 2010), suggesting that the core of the shear zone may have been extruded during transpressional deformation (e.g. Dutch *et al.* 2008; Dutch *et al.* 2010). Magmatism was contemporaneous with the Kimban Orogeny to the west of the shear zone. Pre-orogenic magmatism between ca. 1740 Ma and 1730 Ma (Fanning *et al.* 2007; Fraser *et al.* 2010a), and the syn- to post-orogenic ca. 1710-1700 Ma Moody Suite (Fanning *et al.* 2007), constrain the timing for

regional deformation. However, Electron Probe Micro-Analysis (EPMA) monazite dating of shear fabrics suggest that major shear zone activity persisted until ca. 1680 Ma (Swain *et al.* 2005b; Dutch *et al.* 2008; Dutch *et al.* 2010).

Fraser (2010b) interpreted the Kalinjala Shear Zone as an east dipping structure based on seismic lines across the northern Eyre Peninsula. It was suggested to be active during the Kimban Orogeny with the differing metamorphic grade of the rocks west of the shear zone compared to the east interpreted to reflect extensional movement. Using an analysis of overprinting fabrics Stewart (2010) interpreted the Kalinjala Shear Zone to have formed during the *c.* 1850 Ma Cornian Orogeny (Reid *et al.* 2008) and was subsequently reworked during the 1730-1690 Ma Kimban Orogeny. The high pressure event (850-900 ºC and 9-10 kbar), previously interpreted as the first phase of the Kimban Orogeny (Tong *et al.* 2004), was reinterpreted to record suturing of the Archean core of the Gawler Craton and rocks to the east correlated with the North Australian Craton at *c.* 1850 Ma during the Cornian Orogeny. The Kimban Orogeny was suggested to be a lower grade event that acted to exhume and retrogress (700-750 ºC and 5-6 kbar, Tong *et al.* 2004), the granulite-grade rocks formed during the Cornian Orogeny. However this interpretation was not based on any geochronological work on the structurally mapped fabrics.

In this study the timing of deformation within the Kalinjala Shear zone will be investigated at two locations: in the structurally and thermally reworked Carnot Gneiss, southern Eyre Peninsula, and at Bratten Cairn, ~115 km to the north in the central-eastern Eyre Peninsula (Figure 1).

LITHOLOGICAL UNITS

Bratten Cairn, Central Eastern Eyre Peninsula

The rocks in the Bratten Cairn area have been described in detail by Marmo (1993) and Stewart (2010). They are dominated by generally steeply dipping, north-trending quartzofeldspathic gneisses and mylonites that are interspersed with mafic gneiss and pegmatite. Stewart (2010) describes a complex sequence of deformation that involved the early formation of the peak metamorphic assemblage which was then overprinted by a series of mylonitic fabrics and associated fold events. The peak metamorphic fabric (S1) and associated mineral assemblages are preserved in boudins that range from centimetre to metre scale. The foliation within these boudins is generally more granoblastic in intensity compared to the surrounding mylonitic foliations (Figure 2A). In quartzofeldspathic gneiss, peak metamorphism produced coarse-grained garnet-bearing leucosomes that have been partially replaced by orthopyroxene-bearing anatectic assemblages (Figure 2B). In metapelitic gneiss peak metamorphism produced garnet porphyroblasts up to 1.5 cm in diameter, associated with partial melting. In mafic gneiss, peak metamorphic partial melting produced coarse-grained orthopyroxene-bearing segregations.

Some boudins containing the peak S1 fabric have morphologies that suggest dextral shear along the enclosing S2 gneissic fabric was subsequently reworked by S4 sinistral shear (Figure 2C; Goscombe *et al.* 2004). The S2 fabric is a coarse-grained layering (Figure 2D). The S2 fabric was intruded by pegmatites that locally occupy the axial planes of north-trending upright folds that formed during mylonitic reworking of the S2 fabric or lie within discrete mylonitic shear bands that overprint the S2 fabric (Figure 2E). Preservation of aligned dextrally sheared boudins in weakly

foliated pegmatites suggests that the pegmatites also intruded along the S2 fabric during deformation. In places the pegmatites are unfoliated, but more commonly have been overprinted by predominantly steeply dipping NE-trending S3 mylonitic fabrics that have a generally gently south-plunging lineation. Where these fabrics are planar they define the bulk trend of the Kalinjala Shear Zone at Bratten Cairn. However, in places, the mylonitic deformation resulted in complex fold patterns (Figure 2F), and multiple local generations of mylonitic fabric development. There appears to be a continuum of fabric development and melt mobility, with mylonitic fabrics being crosscut by melt veins and also overprinting them in a progressively more discrete manner, leading to the development of cm-scale ultramylonite. The mylonitic fabrics show a predominance of dextral shear sense (Figure 2G) along the NE-trending foliation. However, in some instances well-defined S4 sinistral shear can also be observed in the same NE-trending fabric orientation (Figure 2H), both within the pegmatites but also within the surrounding fabric.

Carnot Gneiss, Southern Eyre Peninsula

The structural framework for the Carnot Gneiss has been described in detail by Vassallo & Wilson (2001, 2002), Tong *et al.* (2004), and Dutch *et al.* (2008). The rocks are predominantly metasedimentary in origin but also contain granitic gneiss, granodioritic gneiss and mafic rocks that form part of the Sleaford Complex with protolith ages 2520-2400 Ma (Fanning *et al.* 2007; Hand *et al.* 2007; Dutch & Hand 2010). The metasedimentary rocks contain combinations of garnet-cordierite-spinel-sillimanite and garnet-orthopyroxene-biotite, with rare garnet-sillimanite-orthopyroxene-spinel- sapphirine-bearing assemblages. A minimum age for the protoliths is given by the intrusion of *c.* 2000 Ma granodioritic gneiss at Redbanks,

north of Cape Carnot (Fanning, 1997). The first recognised phases of deformation, termed KD1 (Vassallo & Wilson 2001, 2002), led to the formation of north-verging non-cylindrical folds within rocks to the west of the shear zone, and was accompanied by peak metamorphism (Figure 3A, 3B), with peak PT estimates of 850-900 ºC and 9-10 kbar (Tong *et al.* 2004). Fold plunges are parallel to a primary linear fabric (KD1) defined by prolate-shaped mineral aggregates which are also parallel to the strike of the subvertical Kalinjala Shear Zone. A strongly developed, high-grade metamorphic fabric lies subparallel to the lithological layering and was associated with extensive partial melting. The initial orientation of the KD1 fabric envelope is difficult to determine, however it appears to have been gently dipping, possibly southward (Vassallo & Wilson 2001, 2002).

The second phase of deformation (KD2) is interpreted to reflect east-to northeast-verging thrusts west of the Kalinjala Shear Zone, and development of the Kalinjala Shear Zone during dextral transpression (Vassallo & Wilson 2001, 2002). KD2 deformation was associated with lower pressure granulite conditions relative to KD1 (Tong *et al.* 2004; Dutch & Hand 2010). KD2 folds are upright with open to tight profiles and sometimes display chevron-like morphologies with fold packets bound by subvertical north-trending granulite fabric high-strain zones (Figure 3C, 3D). These record either flattening or dextral shear (Figure 3E) associated with partial melting (Figure 3F). Outside the KD2 high-strain zones, flattening is recorded by the development of melting-bearing conjugate shear zones that record decompressional-style mineral assemblages (Figure 3G, 3H).

Recently Stewart (2010) proposed that the high pressure metamorphism on the Eyre Peninsula was associated to *c.* 1850 Ma deformation. Stewart (2010) interpreted that Kalinjala Shear Zone to be a suture between rocks of the North Australian Craton and rocks to the west that they assign to continental ribbons that collided with the North Australian Craton.

The timing of the early KD1 fabric is still unclear. Vassallo & Wilson (2001, 2002) interpreted all the metamorphism and deformation to be associated with the 1730-1690 Ma Kimban Orogeny. However, at Shoal Point, approximately 15km north of Cape Carnot, Dutch *et al.* (2010) obtained an in-situ Electron Probe Micro-Analysis monazite age of 2455 ± 7 Ma from a metapelitic boudin within granulite-facies gneiss, and a partially reset Sm-Nd garnet age of 2128 ± 33 Ma, suggesting that high-grade metamorphism may have occurred during the *c.* 2450 Ma Sleafordian Orogeny. Dutch *et al.* (2008) and Dutch & Hand (2009) also obtained several in-situ EPMA ages between *c.* 1760 Ma and *c.* 1740 Ma for granulite-grade assemblages that record P-T conditions up to 10 kbar and 850 ºC. This suggests that the Kimban Orogeny was responsible for the overall structural and metamorphic character of the Carnot Gneiss. Problematic for the collisional model of Stewart (2010) is an apparent absence of *c.* 1850 Ma metamorphic ages in the Carnot Gneiss despite the preservation of high P-T mineral assemblages that have been interpreted to record *c.* 1850 Ma collision. Part of the goal for this study is to address these different hypotheses.

SAMPLE PETROGRAPHY

Samples were taken from the Bratten Cairn area north of Port Neill and on the southern Eyre Peninsula from Cape Carnot and Black Point. These areas are

interpreted to lie within the core of the shear zone and immediately to the west (Figure 1). At Bratten Cairn samples for detrital and metamorphic geochronology, phase diagram analysis and garnet-biotite diffusional modelling were selected from within the gneissic S2 fabric and north-south trending S3 fabric (Figure 2D, 2E and 2G). Samples contained mineral assemblages interpreted to be metasedimentary rocks and garnet-biotite rich mafic rocks. Along the southern Eyre Peninsula samples for detrital and metamorphic geochronology, and to investigate the high-grade metamorphic mineral assemblages were selected from the low strain east-west trending KD1 fabric and the overprinting high strain north-south trending KD2 fabric (Figure 3C and 3D).

Bratten Cairn

IGC24 – biotite-garnet gneiss

This is a garnet-bearing felsic gneiss containing an S2 fabric defined by biotite. Garnet forms porphyroblasts up to 6mm in diameter. Garnets may contain inclusions of sillimanite, plagioclase, biotite and rare rutile (Figure 4a). S2 biotite is sparsely distributed in a granoblastic matrix composed principally of perthitic K-feldpsar and quartz with lesser plagioclase (Figure 4b).

IGC29 – biotite-sillimanite-garnet gneiss

This sample is a felsic gneiss containing an S2 fabric defined by biotite. Garnet forms porphyroblasts up to 5mm in diameter. Garnets may contain inclusions of sillimanite, plagioclase, biotite and rare spinel. S2 biotite is distributed in a granoblastic matrix composed principally of plagioclase and quartz with lesser K-feldspar. Sillimanite also defines S2, and spinel sometimes forms a matrix mineral in S2 but is rare (Figure 4c).

IGC31 – orthopyroxene-garnet gneiss

Orthopyroxene forms large crystals (up to 15mm) that are located in coarse-grained segregations that also contain plagioclase, garnet and minor quartz and biotite. In outcrop these segregations appear to have been migmatitic, and are now boudinaged in the S2 fabric (Figure 4d). Within the segregations, garnet occurs as small rounded grains within plagioclase. The plagioclase also forms distinct moats that separate garnet from orthopyroxene (Figure 4e). Garnet also occurs as inclusions in the coarse-grained orthopyroxene, and the textural relationships imply that an early garnet-bearing assemblage was replaced by coarse-grained orthopyroxene and plagioclase within migmatitic style segregations. The enclosing S2 fabric domains contain porphyroblastic garnet up to 6mm that is enclosed by S2 biotite. Biotite also encloses porphyroblasts of plagioclase and is paralleled by coarse-grained elongate domains of quartz that define granoblastic ribbon domains. In places the coarse gained quartz and plagioclase matrix has been modified by recrystallisation to finer grained granoblastic aggregates whose grain size is controlled by the distribution of S2 biotite. The S2 fabric is paralleled by narrow mylonitic zones that are defined by fine-grained S3 biotite. Adjacent to these zones the S2 quartz and plagioclase matrix has been texturally modified by dynamic recrystallisation (Figure 4f).

IGC33 – plagioclase-garnet gneiss

This is a garnet-bearing felsic gneiss containing an S2 fabric defined by biotite. Garnet occurs as porphyroblasts up to 3mm in diameter. Garnets may contain inclusions of biotite and rare quartz. S2 biotite is distributed in a granoblastic matrix composed principally of plagioclase and quartz with lesser K-feldspar (Figure 5a).

The S2 fabric is paralleled by narrow S3 domains defined by fine-grained biotite and dynamically recrystallised quartz and feldspar.

BC 2011-011 – garnet-cordierite-biotite gneiss

Garnet forms porphyroblasts up to 15mm that are enclosed by a matrix comprising cordierite, biotite, quartz, plagioclase and minor K-feldspar. Garnet contains inclusions of rutile, ilmenite, plagioclase, quartz, aluminosilicate and spinel (Figure 5b and 5d). Most of the aluminosilicate is sillimanite, however in one instance a higher relief grain contains prominent 75 degree cleavages indicating kyanite (Figure 5c). Spinel is included along the grain boundary of this kyanite grain. In the same garnet, sillimanite occurs as pseudomorphs after grain shapes with typical kyanite habit (Figure 5e). Within garnet, ilmenite occurs as an isolated phase, but also with coronas of rutile (Figure 5f). In places, sillimanite and garnet have been replaced by cordierite, and cordierite has embayed garnet at its contact with the S2 matrix (Figure 5g). The matrix contains coarse-grained cordierite and quartz with a strongly developed S2 fabric defined by biotite. Cordierite contains inclusions of quartz, occasionally ilmenite and very rarely sillimanite (Figure 5h) suggesting that the growth of cordierite at least initially occurred in a sillimanite-bearing matrix.

Carnot Gneiss

BP 2011-008 (Black Point) – garnet-cordierite-sillimanite-spinel-sapphirine gneiss

This high Mg-Al metapelite comes from a low-strain domain that is enclosed by a strong KS2 fabric. The KS2 fabric has well developed dextral shear sense along a shallow-south plunging KS2 lineation. Within the sample, biotite defines two foliations, the younger of which parallels the enclosing KS2 fabric (Figure 6a). To

stay consistent with the structural framework of Vassallo & Wilson (2002), the earlier foliation is designated KS1. The biotite is distributed in a matrix dominated by cordierite. The matrix also locally contains plagioclase. Garnet forms irregular shaped grains up to 6 mm in diameter which have been partially replaced by both the KS1 and KS2 biotite-cordierite association. Garnet may contain inclusions of plagioclase, rutile, ilmenite and sapphirine (Figure 6b). The matrix also contains relic orthopyroxene (Figure 6a), and large (up to 4mm by 1 mm) domains of intergrown cordierite-spinel, or cordierite-spinel-sapphirine (Figure 6a and 6d). Where sapphirine is present in these intergrowths, the proportion of sapphirine varies from < 5% to > 25%. Rarely these cordierite-spinel ± sapphirine-bearing domains contain relic sillimanite, confirming that sillimanite was once part of a pre-KS1/KS2 assemblage containing garnet-orthopyroxene-sillimanite. The cordierite mantles associated with the spinel +/- sapphirine intergrowths are weakly elongate in the KS2 fabric (Figure 6c), suggesting that replacement of sillimanite may have accompanied KD2 deformation.

CG01/IGC44 (Redbanks) – biotite-cordierite-garnet gneiss

This sample contains an intense north-south trending foliation that is correlated with KS2. The foliation is defined by cordierite, biotite, minor ilmenite and elongate garnet that is paralleled by coarse granoblastic domains of K-feldspar that also contain quartz. Garnet contains inclusions of sillimanite, biotite and occasionally spinel, and has been heavily embayed by cordierite in association with the development of minor spinel. In the matrix this replacement process may in part be responsible for the elongate character of the garnet grains (Figure 6e). In the matrix, spinel primarily occurs in cordierite-rich, biotite-poor domains that are elongate parallel to the overall

foliation. In places these domains contain relic sillimanite (Figure 6f), suggesting that the cordierite –spinel associated replaced sillimanite during the development of KS2.

Shoal Point East

ASE-01 – K-feldspar-garnet-biotite gneiss

This is a garnet-bearing felsic gneiss containing an S2 fabric defined by biotite. Garnet forms porphyroblasts up to 7mm in diameter. Garnets may contain inclusions of sillimanite, plagioclase, quartz and biotite. S2 biotite is sparsely distributed in a granoblastic matrix composed of granoblastic K-feldspar, quartz and plagioclase.

Shoal Point

The petrography of the metasedimentary succession at Shoal Point has been described in detail by Dutch *et al.* (2010).

SP6 – cordierite-spinel-garnet gneiss

This sample is a representative of Assemblage 2 of Dutch *et al.* (2010). It contains anhedral garnet grains between 1 and 8mm in length. These are enclosed by KS2 assemblage consisting of biotite, quartz and plagioclase. Garnet contains inclusions of biotite, sillimanite and occasionally spinel. The matrix contains large grains of cordierite that commonly occur with intergrowths of spinel. These composite cordierite-spinel domains contain relics of garnet and sillimanite suggesting they formed at the expense of garnet-sillimanite.

SP7 – garnet-biotite gneiss

This sample is a felsic gneiss containing KS2 fabric defined by biotite. Garnet forms porphyroblasts up to 7mm in diameter. Garnet grains may contain inclusions of plagioclase, quartz and biotite. Garnets appear to contain evidence for two stages of growth. The S2 biotite in a coarse-grained granoblastic matrix composed of plagioclase, quartz and ilmenite.

SP9 –garnet-orthopyroxene-biotite gneiss

This is a garnet-orthopyroxene-biotite bearing quartz-rich gneiss. Garnet forms large porphyroblasts up to 11mm in diameter. Garnet contains inclusions of quartz, biotite and ilmenite, which occurs both as small grains, and as a "dusty" distribution of very fine grains. The garnets appear to have undergone two stages of growth, with a core rich in inclusions (particularly ilmenite), enclosed by a rim that is largely inclusion free (Figure 6g). In general the inclusion-poor rim is ~ 30% of the radial extent of garnet grains. The enclosing S2 fabric is defined by orthopyroxene and coarse-grained biotite that is associated with coarse-grained quartz and lesser plagioclase. Garnet is locally embayed by plagioclase and orthopyroxene.

ANALYTICAL METHODS

Bulk rock and mineral chemistry

Phase equilibria calculations were used in this study to estimate the thermal and physical pressure-temperature conditions of metamorphism at Bratten Cairn. Whole rock geochemical analysis was used to determine the bulk composition of sample BC 2011-011. A representative slice of sample BC 2011-011 was crushed and milled to < 75µm. Bulk-rock chemical compositions were obtained from Amdel Laboratories, Adelaide (Table 1). The concentration of major and trace elements was analysed through solution ICP-MS. A subsample was initially fused with lithium metaborate

followed by dissolution in nitric acid before being presented for ICP-MS analysis (see Payne *et al.* 2010). Chemical analyses of minerals were obtained using a Cameca SX51 electron microprobe at the University of Adelaide. A beam current of 20 nA and accelerating voltage of 15 kV was used for all point analyses.

Zircon U-Pb LA-ICPMS geochronology

Samples for zircon geochronology were crushed, milled sieved and subsequently separated by standard density and magnetic separation techniques to those reported in (Payne *et al.* 2006b; Wade *et al.* 2007). Approximately 250 zircon grains per sample were randomly hand picked and mounted in an epoxy resin disc. Zircons were imaged using a Philips XL20 SEM with attached Gatan cathode-luminescence (CL) detector at Adelaide Microscopy to determine internal chemical zonation of grains. U-Th-Pb analysis of zircon was undertaken using an Agilent 7500cs ICP-MS with a New Wave 213 nm Nd–YAG laser in a He ablation atmosphere at Adelaide Microscopy, University of Adelaide, following the method of Payne *et al.* (2008). Ablation of zircon grains was performed with a spot size of 30μm, laser intensity of (6-8 Jcm^{-2}) 75% and frequency of 5 Hz. A 50 second background was measured, followed by a 50 second sample analysis. The laser was fired for 10 seconds with the shutter closed at 40 seconds prior the ablation. Analyses measured isotopes ^{204}Pb, ^{206}Pb, ^{207}Pb, ^{208}Pb, ^{232}Th and ^{238}U for 10, 15, 30, 10, 10, 15 ms, respectively. As with in-situ monazite geochronology common lead was not corrected for.

Zircon data was reduced using 'Glitter' software (Griffin *et al.* 2008). Elemental fractionation was corrected using the standard GJ-1 (TIMS normalisation data: $^{207}Pb/^{206}Pb$ = 607.7 ± 4.3 Ma, $^{206}Pb/^{238}U$ = 600.7 ± 1.1 Ma and $^{207}Pb/^{235}U$ = 602.0 ±

1.0 Ma: Jackson *et al.* 2004). Internal standard Plesovice (TIMS normalisation data: 206Pb/238U = 337.13 ± 0.37 Ma: Sláma *et al.* 2008) was used to assess the accuracy of unknown analyses. Plesovice average ages over the course of this study were $^{206}Pb/^{238}U$ = 336 ± 1 Ma (n=62, MSWD = 0.71), $^{207}Pb/^{206}Pb$ = 342 ± 9 Ma (MSWD = 0.78), $^{207}Pb/^{235}U$ = 337 ± 1 Ma (MSWD = 0.59). As all samples analysed are greater than 1000 Ma all ages quoted are in $^{207}Pb/^{206}Pb$ unless stated otherwise.

In-situ monazite U-Pb LA-ICPMS geochronology

Monazite geochronology was undertaken to determine the age of the metamorphism in the Kalinjala Shear Zone. Monazites grains were located and imaged to determine textural location and compositional variability using back-scattered electron (BSE) imaging on a Philips XL30 FEGSEM at Adelaide Microscopy, University of Adelaide. Operating procedures included an accelerating voltage of 15kV, spot size of 3 and working distance of 10mm. U–Pb isotopic analyses were acquired using a New Wave 213 nm Nd–YAG laser in a He ablation atmosphere connected to an Agilent 7500cs ICP-MS at Adelaide Microscopy, the University of Adelaide, following the method of Payne *et al.* (2008). Ablation of monazites was performed with a spot size of 15µm, laser intensity of 75% (8-9 Jcm^{-2}) energy and a frequency of 5 Hz. Each analysis was acquired over a total time of 90 seconds. This included 30 seconds of background measurement, 10 seconds with the shutter closed to allow beam and crystal stabilisation and 50 seconds of sample analysis. Analyses measured ^{204}Pb, ^{206}Pb, ^{207}Pb, and ^{238}U for 10, 15, 30 and 15 ms, respectively. Common lead was not corrected in age calculations, however the ^{204}Pb isotope peak was monitored during acquisition and analyses removed if appreciable amounts of common lead were observed.

Monazite data was reduced using 'Glitter' software. Elemental fractionation was corrected using the external monazite standard 44069 (TIMS normalisation data: 206Pb/238U = 426 ± 3 Ma: Aleinikoff *et al.* 2006) for Redbanks CG01, IGC24 and half of the data collection for IGC29. The monazite standard MAdel (TIMS normalisation data: $^{207}Pb/^{206}Pb$ = 491.0 ± 2.7 Ma, $^{206}Pb/^{238}U$ = 518.37 ± 0.99 Ma and $^{207}Pb/^{235}U$ = 513.13 ± 0.19 Ma: Payne *et al.* 2008) was used for BC 2011-011, BP 2011-008, ASE-01, SP6, SP7 and half of the data collection for IGC29 due to within run issues with 44069. The accuracy of the corrected data was verified using the in-house standard 222 (c. 450 Ma, Payne *et al.* 2008) and MAdel (Payne *et al.* 2008). Throughout this study the weighted mean $^{206}Pb/^{238}U$ age for 222 was 446.9 ± 2.4 Ma (n=30 MSWD = 0.49) and 520.1 ± 4.7 Ma (n=10, MSWD = 0.25) for MAdel.

Quantified metamorphic analysis

The bulk composition of sample BC 2011-011 was determined from whole rock geochemical analysis. A pressure-temperature (P-T) pseudosection was calculated for BC 2011-011 using the phase equilibria modelling program THERMOCALC v3.33 (June 2009 update of Powell & Holland 1988) using the internally consistent dataset of Holland and Powell (1998; data set tc-ds55, updated Nov. 2003) for the geologically realistic system NCKFMASHTO (Na2O-CaO-K2O-FeO-MgO-Al2O3-SiO2-H2O-TiO2-Fe2O3). The P-T calculations use the *a-x* relationships of White *et al.* (2007) for biotite, garnet and silicate melt, White *et al.* (2000) for ilmenite, Holland and Powell (2003) for K-feldspar plagioclase and White *et al.* (2002) for magnetite and orthopyroxene.

Temperature-time modelling

Temperature-time models were constructed using the diffusion modelling code THERMAL HISTORY of Robl *et al.* (2007) based on diffusion rates of Fe-Mg between garnet and biotite. The modelling code calculates the diffusion equation using a series of input parameters for the Fe-Mg diffusion within garnet, enabling a measured diffusion-related compositional profile to be matched to a cooling rate and/or explore compositional profiles that would result from a specified heating/cooling history. The extent of Fe-Mg re-equilibration is both temperature and rate of cooling dependent (Ehlers & Powell 1994; Ehlers *et al.* 1994; Hauzenberger *et al.* 2005; Robl *et al.* 2007). The application of the diffusion modelling code of Robl *et al.* (2007) comes with a number of assumptions: (1) all garnet crystals being modelled are spherical and completely surrounded by an infinite biotite reservoir, and there is uninterrupted chemical equilibrium between the two mineral phases, (2) only the binary exchange of Fe and Mg is considered, (3) the garnet crystal has no zoning and zoning occurred only during retrogression/cooling, and (4) there is infinitely fast diffusion within the biotite reservoir and as a consequence there is no chemical zonation in biotite (Ehlers & Powell 1994; Ehlers *et al.* 1994; Hauzenberger *et al.* 2005; Robl *et al.* 2007). Each assumption for use in the diffusion modelling code was deemed to be reasonable in relation to this study's samples. The Fe-Mg diffusional constants of Ganguly *et al.* (1998) were used to model the diffusion between garnet and biotite. Samples were selected based on garnet being in direct contact with coarse and/or abundant biotite as well as the measured chemical zonation profile. Garnet compositional profiles with considerable fluctuations of Mg at the outermost rim coupled with relatively compositionally flat cores were favoured, notably the radial section from the garnet core to the outermost rim in contact with biotite. EPMA

compositional data integrated with diffusive properties of two samples were chosen to model the thermal and cooling regime. Sample ASE-01 from Shoal Point East contains garnet porphyroblasts with coarse biotite and exhibits minimal retrograde textures. Sample IGC24 from Bratten Cairn contains garnet porphyroblasts with sparse biotite. Garnets exhibit retrograde textures. Various cooling rates were experimented with to enable cooling histories to be developed that created to the garnet profile analysed.

RESULTS

Mineral Chemistry

Table 2 provides a summary of garnet and biotite analysed in IGC24 and ASE-01. Analyses were conducted on a Cameca SX51 microprobe at Adelaide Microscopy with an accelerating voltage of 15kV and beam current of 20 nA.

Garnet

Sample IGC24 is dominated by almandine-rich garnet with X_{Fe} [Fe/(Mg+Fe+Ca+Mn)] values of 0.59-0.75 and X_{Mg} [Mg/(Mg+Fe+Ca+Mn)] of 0.2-0.38. Garnet grains contain manganese of X_{Mn} [Mn/(Mg+Fe+Ca+Mn)] of approximately 0.01, increasing towards the rim to 0.025. Garnets have low grossular of X_{Ca} [Ca/(Mg+Fe+Ca+Mn)] of approximately 0.018.

Sample ASE-01 is dominated by almandine-rich garnet with X_{Fe} [Fe/(Mg+Fe+Ca+Mn)] values of 0.72-0.78 and X_{Mg} [Mg/(Mg+Fe+Ca+Mn)] of approximately 0.16-0.2. Garnet grains contain very little manganese with X_{Mn} [Mn/(Mg+Fe+Ca+Mn)] of approximately 0.055, manganese increases towards the rim

of the garnets to approximately 0.068. Garnets have low grossular of X_{Ca} [Ca/(Mg+Fe+Ca+Mn)] of approximately 0.038.

Biotite

Sample IGC24 biotite has X_{Mg} [Mg/(Mg+Fe+Ca+Mn)] value of approximately 0.63, titanium content of 2.73-3.33 wt.% and aluminium content of 16.08–17.37 wt.%. Sample ASE-01 biotite has X_{Mg} [Mg/(Mg+Fe+Ca+Mn)] value of approximately 0.5, titanium content of 2.92-3.92 wt.% and aluminium content ranges from 16.29–18.82 wt.%.

LA-ICPMS Geochronology

All zircon analyses from this study are shown in Appendix 2A

All monazite analyses from this study are shown in Appendix 2B

Bratten Cairn – Zircon Geochronology

IGC31 (metasediment)

Seventy analyses were conducted on sixty three grains targeting weakly luminescent to luminescent cores and rims. Fifty three analyses were on cores and oscillatory zones in multiple populations from 2730 ± 18 Ma to 1771±15 Ma (n=8, MSWD = 0.56) (Figure 7a and 7b). Five age populations were identified within this range: a single analysis on a moderately luminescent core 2730 ± 18 Ma; 2451 ± 61 Ma (n=9, MSWD = 15); 2181 ± 45 Ma (n=7, MSWD = 5.4); and a younger group of grains older than 1800 Ma, 1871±13 Ma (n=26, MSWD = 1.7) (Figure 7c and 7d). The youngest age population of moderately luminescent oscillatory zones (Figure 7d: A) gives a weighted mean $^{207}Pb/^{206}Pb$ age 1771 ±15 Ma (n=8, MSWD = 0.56) and is

interpreted as the maximum depositional age for IGC31. Two analyses on a dark metamorphic rim gave $^{207}Pb/^{206}Pb$ ages of 1631 ± 33 Ma and 1650 ± 37 Ma.

IGC33 (metasediment)

Thirty eight zircon analyses were collected over multiple LA-ICPMS sessions targeting weakly-moderately oscillatory and concentric zoned luminescent cores and weakly luminescent rims. Eight analyses had a concordancy of 100 ± 10 % (Figure 8b), with the majority of analyses discordant (Figure 8b). Discordant analyses correspond to contrastingly bright and dark oscillatory zones and dark featureless cores. These zones are interpreted to have experienced Pb-loss during subsequent deformation events. The concordant analyses fall into three groups (Figure 8c) dominated by the age range 2480-2575 Ma (Figure 8d: B and C) with single analyses at 2776 ± 19 Ma and 2062 ± 20 Ma. Due to the low number of analyses it cannot be ruled out that some age populations were not sampled. From the analysed concordant grains the youngest age of 2062 ± 20 Ma (Figure 8d: A) is interpreted as a best estimate of the maximum age of deposition.

Bratten Cairn – Monazite Geochronology

IGC24

Six analyses on four monazite grains were conducted targeting both light and dark domains. Heterogeneous internal morphologies corresponded to different ages. Dark cores correspond to older ages relative to the rims (Figure 9b). One analysis was discarded as an outlier to the main population ($^{207}Pb/^{206}Pb$ age: 1875 ± 18 Ma). One age population is present in IGC24 (Figure 9a), with a weighted average $^{207}Pb/^{206}Pb$ age of 1713 ± 18 Ma (n=4, MSWD = 0.02).

IGC29

Forty analyses were conducted on thirty nine monazite grains that were texturally located within garnet and the biotite matrix. One analysis was discarded due to poor concordancy (91%) compared to all other analyses (99-101%; Figure 9c). Despite variations in textural relationships of monazite grains to other minerals, one age population is apparent (Figure 9d: A and B). Thirty nine analyses yielded a weighted average $^{207}Pb/^{206}Pb$ age of 1709 ± 7 Ma (MSWD = 0.23). The quoted weighted average is the estimate of metamorphism for this sample and is consistent with the interpreted metamorphic age of proximal sample IGC24.

BC 2011-011

Three analyses were conducted on one monazite grain texturally located within a garnet that is also host to a single kyanite grain (Figure 9f). Analyses gave a weighted average $^{207}Pb/^{206}Pb$ age of 1714 ± 25 Ma (MSWD of 0.16) (Figure 9e).

Carnot Gneiss – Zircon Geochronology

IGC44 (metasediment)

Thirty analyses on twenty eight zircon grains were conducted over multiple LA-ICPMS sessions in order to minimize any inaccuracy of results due to potential variability of the LA-ICP-MS. The analysis targeted luminescent to weakly luminescent cores and weakly luminescent rims. Dark featureless cores and rims correspond to discordant analyses and are interpreted as metamorphic zircon while luminescent and concentrically zoned cores are interpreted as detrital igneous zircon grains (Figure 10b: A). Analysis yielded a $^{207}Pb/^{206}Pb$ age weighted average range from 2649 ± 14 Ma (n=6, MSWD = 0.03) to 2314 ± 31 Ma (n=2, MSWD = 0.94) and a concordance range from 90-102% (Figure 10a). Age populations are *c.* 2650 Ma, *c.*

2520-2450 Ma, *c.* 2400 Ma and *c.* 2300 Ma (Figure 10d). *Circa.* 2500-2300 Ma zircon grains exhibit features typical of metamorphic resetting (Figure 10b: B) and are therefore disregarded from the detrital zircon age population. The youngest concordant population of interpreted detrital zircon grains at *c.* 2544 ± 45 Ma is interpreted as the maximum deposition age of this sample. Interpreted metamorphic zircon is present in a spread from *c.* 2500-2300 Ma. Constraint on the deposition to near the maximum depositional age and suggests that it was deposited and subsequently metamorphosed during the Sleafordian Orogeny.

Carnot Gneiss – Monazite Geochronology

CG01

Sixteen monazite analyses were obtained on 13 grains that were microstructurally hosted in perthitic feldspar or biotite. Compositional variation was observed with BSE imaging with darker cores and light rims on some grains but analyses in each zone were within error (Figure 10e: A-B). These analyses were slightly reversely discordant (Figure 10d) but are considered robust as the standards were within error of the TIMS age data (Payne *et al.* 2008; updated with additional TIMS data). The ages range from 1717-1666 Ma with one outlier at 1742 ± 18 Ma (95% concordancy) and do not fall into two or more age populations but are evenly spread and due to this a weighted mean of 1693.4 ± 9 Ma (n=16, MSWD = 1.07) is used.

BP 2011-008

Ten analyses were conducted on five monazite grains in biotite matrix (Figure 11c: A and B) and sapphirine reaction microstructures (Figure 11c: C). One analysis was discarded due to the variable nature of the isotopic signal and inability for a portion of the signal with a sufficient integration time to be selected. Two analyses on a

monazite grain texturally located within sapphirine reaction texture (Figure 11c: C) yield reversely discordant ages with $^{207}Pb/^{206}Pb$ ages 2365 ± 31 Ma (98 % concordancy) and 2201 ± 23 Ma (97 % concordancy) (Figure 11a). The younger age population of seven analyses (Figure 11b) yields a weighted average $^{207}Pb/^{206}Pb$ age of 1745 ± 14 Ma (MSWD of 0.32).

Shoal Point – Monazite Geochronology

SP6

Eighteen analyses were conducted on five monazite grains hosted by spinel, cordierite and plagioclase (Figure 12b). Two analyses were discarded due to variable nature of the isotopic signal and inability for a portion of the signal with a sufficient integration time to be selected. One age population is apparent (Figure 12a) with sixteen analyses yielding a weighted average $^{207}Pb/^{206}Pb$ age of 1717 ± 12 Ma (MSWD = 0.41).

SP7

Sixteen analyses were conducted on fifteen monazite grains microstructurally located in garnet and the biotite matrix (Figure 12d: A-B). Three analyses were discarded due to the variable nature of the isotopic signal and inability for a portion of the signal with a sufficient integration time to be selected. Despite variable textural relationships of monazite grains with other minerals one age population is apparent (Figure 12c). Thirteen analyses give a weighted average $^{207}Pb/^{206}Pb$ age of 1712 ± 10 Ma (MSWD of 0.25).

Shoal Point East

ASE-01

Eighteen analyses were conducted on eighteen monazite grains microstructurally located within garnet and the matrix (Figure 12f). One analysis was discarded due to the variable nature of the isotopic signal and inability for a portion of the signal with a sufficient integration time to be selected. One analysis was discarded as a reversely discordant outlier to the main population (Figure 12e). Sixteen analyses give a weighted average $^{207}Pb/^{206}Pb$ age of 1706 ± 9 Ma (MSWD of 0.59).

Temperature-time modelling

A summary of garnet-biotite modelling conditions is presented in Table 3.

Temperature-time modelling was used to constrain the cooling histories of the rocks within the core of the shear zone at Bratten Cairn and on the flank of the shear zone at Shoal Point East.

Bratten Cairn – IGC24

Manganese content increases towards the garnet rims of this sample (Figure 13d). The garnet profile is subsequently a result of advective and diffusive transport and therefore garnet diffusional modelling is strictly not possible. However, while the near rim profile has been modified by resorption (Figure 13d), based on the small absolute change in X_{Mn} the amount of garnet that has been consumed is small. Assuming the that X_{Mn} was originally the same value across the garnet only around 100 microns of the garnet rim has been consumed (e.g. Kohn & Spear 2000). In order to preserve the observed interior composition in the presence of the matrix biotite composition of 0.64 X_{Mg}, requires cooling from a peak of ~810 °C to have occurred faster than ~50

°CMy^{-1} (Figure 13b and 13c). Based on the matrix biotite composition the garnet composition at the rim corresponds to a temperature of ~500 °C.

Shoal Point East – ASE-01

Garnet diffusion-based modelling of the cooling rate within the large garnet of this sample (Figure 14a and 14d) records a core Fe-Mg exchange thermometry temperature of ~660 ºC and a rim temperature of 300 ºC (Figure 14b and 14c). A curve with an estimation of X_{Mg} within biotite prior to diffusion of 0.50 shows as the best fitting rate (Figure 14b). In order to preserve this profile the garnet cooled from a peak temperature of ~660 ºC through 300 ºC in *c.* 50 Myr. This implies an average cooling rate of ~7 ºCMyr^{-1}. The diffusion profile is best described by a power law cooling calculation where the rate of cooling increases with time (Figure 14c), suggesting that the rate of cooling increased rapidly after ~30 Myr.

Phase Diagram Analysis

BC 2011-011

A pressure-temperature pseudosection was constructed for the kyanite-bearing cordierite-garnet gneiss sample BC 2011-011. The P-T pseudosection shown in Figure 15 was derived using a whole rock bulk composition, assuming a Fe^{2+}/Fe^{3+} ratio of 0.96. This value is within range typically adopted for metapelitic rocks that lack appreciable oxide phases and do not contain magnetite (e.g. White *et al.* 2000; White *et al.* 2001). There has been no attempt to investigate the sensitivity of the computed phase relations as a function of varying Fe^{2+}/Fe^{3+} ratio. Additionally, the H_2O content is likely to have been underestimated compared to what would have been present on the prograde path. However, the presence of un-retrogressed cordierite in the sample

suggests that melt loss occurred either during prograde evolution or high-temperature retrograde conditions (e.g. White *et al.* 2001; White *et al.* 2007). However, composition, volume and timing of melt is difficult to constrain, and the phase relations shown in Figure 15 are based on the bulk composition after melt loss, and therefore are likely to only approximate the quantitative P-T evolution. Nevertheless, the phase relations in the P-T pseudosection of BC 2011-011 (Figure 15) appear to account for the important textural evolution of sample BC 2011-011.

Garnet in this sample contains inclusion of ilmenite, rutile, spinel, plagioclase, sillimanite, kyanite, quartz and biotite (Figure 5b). Blocky sillimanite aggregates pseudomorph kyanite (Figure 5e) and rutile sometimes occurs as coronas on ilmenite (Figure 5f). The presence of ilmenite both with and without rutile coronas suggests an early assemblage of ilmenite-kyanite-plagioclase-biotite-quartz. The presence of rutile coronas on ilmenite within garnet imply that garnet growth accompanied the development of rutile in the sample, and in all probability garnet was present during the development of the rutile-free and rutile-bearing assemblage. The transition from ilmenite to ilmenite-rutile suggests an up-pressure evolution, although the maximum pressure is poorly constrained. However, Dutch (2009) reported pressures of 10-11 kbar from within the Kalinjala Shear zone at Port Neill, approximately 10 km to the south.

Spinel occurs as inclusion in garnet (Figure 5c) and most likely formed during the breakdown of zinc-bearing staurolite on the prograde path (Kawakami & Motoyoshi 2004; Kawakami & Hokada 2010). Spinel and staurolite are some of the few minerals that will take in zinc; therefore it is likely that this sample contained zinc-bearing

staurolite that reacted to form zinc bearing spinel with kyanite. The kyanite-spinel association within garnet implies that the breakdown of staurolite occurred within the kyanite stability field, most likely via the reaction: staurolite = kyanite + garnet + spinel (Kawakami & Motoyoshi 2004; Kawakami & Hokada 2010). It is difficult to calculate the position of Zn-bearing equilibria at present as the activity relationships are not easily modelled (White *et al.* 2007) and so it is difficult to predict where these reactions would plot in P-T space. However, Cutts *et al.* (2011) modelled a similar reaction for the breakdown of staurolite to the assemblage garnet-kyanite-plagioclase-biotite-rutile-ilmenite-quartz. This breakdown reaction occurred at 7-8 kbar and ~640 ºC. This suggests that the breakdown of staurolite to spinel + kyanite in BC 2011-011 occurred on the prograde path prior to the rock crossing into the peak pressure metamorphic field garnet-biotite-kyanite-plagioclase-quartz-ilmenite-rutile-K-feldspar-spinel. The peak mineral assemblage is constrained to > 8 kbar and 600-850 ºC. The presence of spinel and quartz inclusions in garnet in BC 2011-011 appears to occur at temperatures lower than typically associated with quartz-spinel assemblages (e.g. Kelsey, 2007), suggesting that the spinel contains sufficient zinc to lower its temperature stability.

While peak pressures cannot be tightly constrained at Bratten Cairn, the assemblage garnet-kyanite-rutile-ilmenite-plagioclase-biotite is stable to beyond 12 kbar at temperatures < 850 ºC (Figure 15). The S2 fabric in the sample consists of post-peak biotite-cordierite-K-feldspar-plagioclase-ilmenite-quartz. Cordierite has locally embayed garnet and consumed sillimanite that formed after kyanite (Figure 5g). The development of the cordierite-bearing S2 assemblage implies a steep decompressional evolution following peak pressures.

DISCUSSION

Age and Provenance of Protoliths

Bratten Cairn Metasediments – provenance and geological implications

The provenance, age of deposition and subsequent timing of deformation of the Bratten Cairn metasedimentary rocks has not previously been studied. The rocks are interpreted to lie within the core of the Kalinjala Shear Zone and its western edge (Stewart 2010) but have not been correlated with any known rock unit.

IGC31

The zircon grains of sample IGC31 fall into five age populations between *c.* 2800-1770 Ma. The distribution of ages within this range display similarities with the eastern Eyre Peninsula Cleve Group Mangalo Schist of Szpunar *et al.* (2011; Figure 16a and 16b). The minor Archean peaks and *c.* 2500-2300 Ma and *c.* 2250-2100 Ma populations are similar in age and population distribution to the Mangalo Schist. The maximum depositional age of 1771 ± 15 Ma is within error of the maximum deposition of the *c.* 1790 Ma Mangalo Schist. The dominant age peak of *c.* 1770-1900 Ma in IGC31 is represented in the Mangalo Schist and also displays similar bimodal distribution. On the basis of these correlations the metasedimentary rocks of IGC31 are interpreted as a stratigraphically equivalent unit to the Mangalo Schist of the Cleve Group.

IGC33

The zircon grains of IGC33 are interpreted to have been subjected to large amounts of Pb-loss during subsequent Kimban-related deformation. Sample IGC33 has a $^{207}Pb/^{206}Pb$ maximum age of deposition of 2062 ± 20 Ma but due to the low number

of analyses it is possible that some detrital zircon populations were not sampled in this study. From the available data the maximum age of deposition is interpreted as *c.* 2000 Ma. The population distribution of IGC33 is broadly similar to that of the lower Cleve Group unit the Darke Peak Group of Szpunar *et al.* (2011; Figure 16c and 16d). The Darke Peak Group was deposited at *c.* 1865 Ma and is stratigraphically located below the Mangalo Schist (Szpunar *et al.* 2011). Although IGC33 does not include concordant detrital zircon grains at *c.* 1860 Ma the strongly recrystallised nature of the zircon grains means this cannot be discounted. IGC33 is tentatively suggested to be stratigraphically equivalent to the Darke Peak Group.

The Bratten Cairn metasedimentary rocks are interpreted as stratigraphic equivalents of the Cleve Group of Szpunar *et al.* (2011). Therefore the sources of sedimentary detritus are also likely to be similar. The prominent U-Pb detrital zircon ages recorded in the Bratten Cairn metasediments are *c.* 2700 Ma, *c.* 2500 Ma, *c.* 2200 Ma, *c.* 1860 Ma and *c.* 1770 Ma (Figure 16a and 16c). Potential Archean source rocks in the Gawler Craton containing zircon of *c.* 2500 Ma and *c.* 2700 Ma ages include the basement to the Cleve Group, i.e. the Late Archean Sleaford Complex and the Mulgathing Complex (Swain *et al.* 2005a). *Circa* 2200 Ma zircon is unknown in the Gawler Craton (Swain *et al.* 2005a; Fanning *et al.* 2007), however *c.* 2200 Ma zircon has been found in Antarctica (Goodge & Fanning 2010), which is interpreted to be attached to Southern Australia during the Paleoproterozoic (Dalziel 1991; Borg & Depaolo 1994; Flöttmann & Oliver 1994). A possible nearby source of *c.* 1860 Ma zircon grains is the voluminous *c.*1850 Ma intrusive Donington Suite which is juxtaposed against the Bratten Cairn units by the Kalinjala Shear Zone. However, using zircon Lu-Hf and Sm-Nd isotopic analysis in conjunction with U-Pb

geochronology and REE whole rock geochemistry Szpunar *et al.* (2011) concluded that the Donington Suite was too enriched in REE and fractionated compared to the Cleve Group and therefore unlikely to have been a significant source component of the Cleve Group. Therefore by inference it is also likely that *c.* 1860 Ma zircon in the Bratten Cairn rocks were not sourced from the Donington Suite, although as a full isotopic study of the Bratten Cairn zircon grains has not been completed it cannot be discounted. The *c.* 1860 Ma zircon grains may have been sourced from outside the Gawler Craton. Payne *et al.* (2006a; 2009) and Barovich and Hand (2008) suggested a provenance for two major Proterozoic basins in the Gawler Craton that included the Mt. Isa Inlier Province and the Arunta region of the North Australian Craton. Zircon grains sourced from granitoids of *c.* 1870-1750 Ma Arunta region and *c.* 1860-1850 Ma felsic igneous rocks of the Mt. Isa Province (Hooper 2001) could account for the younger peaks in the Bratten Cairn metasedimentary rocks but further isotopic work is need to resolve this.

Possible sources within the Gawler Craton for *c.* 1770 Ma zircon are the *c.* 1790 Ma Myola Volcanics which lie close to the Cleve Group on the northern Eyre Peninsula. The *c.* 1790 Ma Tidnamurka Volcanics which lie north east of the Gawler Craton are also a possible source although it is beyond the scope of this study to unequivocally determine the provenance of this unit.

The detrital zircon data suggests that metasedimentary rocks within the Bratten Cairn segment of the shear zone are equivalents of the Cleve Group (Szpunar *et al.* 2011) with a maximum depositional age of *c.* 1780 Ma. This precludes there being any pre-Kimban deformation in the metasedimentary rocks. The metasedimentary rocks

contain the peak metamorphic fabrics *c.* 1713-1709 Ma. Therefore it is unlikely that there is any significant structural preservation of pre-Kimban events as required by the model of Stewart (2010) as that would require there to be tectonic slices of the Archean-Early Paleoproterozoic basement within the shear zone. As no overt structural evidence of early structural domains wrapped by the fabrics that contain the pelites was observed this is considered unlikely.

Carnot Gneiss Metasediments – provenance and geological implications
IGC44

The sample IGC44 of the Redbanks area has a maximum depositional age of 2544 ± 45 Ma. Interpreted metamorphic zircon at *c.* 2500-2400 Ma constrains deposition to close to the maximum depositional age. The age distribution of *c.* 2650 Ma, *c.* 2500 Ma, and metamorphic *c.* 2400 Ma corresponds to the Archean Sleaford Complex on the Eyre Peninsula (Figure 16e and 16f; Swain *et al.* 2005a) and therefore this sample is interpreted to be part of the Carnot Gneiss of the Sleaford Complex.

Provenance of IGC44

The prominent detrital zircon components from IGC44 are *c.* 2650 Ma, *c.* 2500 Ma and *c.* 2400 (Figure 16e). There are no known units of *c.* 2650 Ma in the Gawler Craton but the presence of *c.* 2700 Ma basement units is indicated by inherited *c.* 2650 Ma zircon in the 2520-2500 Ma Hall Bay Volcanics and the 2460 Ma Wangary Gneiss from the southern Gawler Craton (Fanning *et al.* 2007). If these older Archean successions were exposed at the surface prior to, or during deposition of IGC44 they may have contributed to the sediment. Antarctica is interpreted to represent an extension of the Gawler Craton during the Archean, representing a possible source of *c.* 2650 Ma and *c.* 2500 Ma zircon (Goodge & Fanning 2010; Boger 2011). However,

due to a paucity of outcrop the age of the Antarctic basement is not well constrained (Borg & Depaolo 1994; Veevers *et al.* 1997; Peucat *et al.* 1999; Zhao *et al.* 2002). Swain *et al.* (2005a) noted that the there is an overlap between the maximum depositional age and age of metamorphism of the Sleaford Complex, suggesting that the Carnot Gneiss was deposited up until the beginning of the Sleafordian Orogeny, consistent with the small age gap between youngest detrital zircon grain and metamorphic zircon grains in IGC44.

Age of Metamorphism

At granulite facies conditions monazite typically records an age along the metamorphic P-T path (Rubatto *et al.* 2001; Rubatto *et al.* 2006; Kelsey *et al.* 2008). Earlier authors interpreted that under high temperature conditions U-Pb ages of monazite typically represents the timing of the rocks passing through closure temperatures of ~700 ºC (Vavra & Schaltegger 1999; Rubatto *et al.* 2001). More recently it has been suggested that monazite has closure temperatures much higher, approximately 950 ºC for a 20 µm monazite at 10 ºCMyr^{-1} (Cherniak & Watson 2001; Cherniak *et al.* 2004) and is able to preserve growth ages for the duration of a typical metamorphic event. Taking this into account, the monazite ages quoted in this study are interpreted to be representative of monazite growth during metamorphism, most likely on the retrograde path.

Bratten Cairn

Monazite grains analysed in Bratten Cairn samples yield the same metamorphic age within uncertainty (Samples IGC24 = 1713 ± 18 Ma, IGC29 = 1709 ± 7 Ma, BC 2011-011 = 1714 ± 25 Ma). Within the core of the shear zone at Bratten Cairn the S2

fabric is parallel to the trend of the shear zone and is constrained to ~1710 Ma based on the monazite ages obtained in this study. Additionally, monazite included within garnet that contains the peak pressure kyanite-rutile assemblage also gives an age of ~1710 Ma. The peak and post-peak metamorphism recorded by the rocks at Bratten Cairn is interpreted to be associated with the Kimban Orogeny. This is also supported by the maximum depositional age of *c.* 1780 Ma obtained from interlayered metasediments that contain peak (S1) and retrograde (S2 and S3) mineral assemblages.

Carnot Gneiss

Monazite at Redbanks (Sample CG01) was dated at 1693 ± 9 Ma. This age is within error of *c.* 1708-1690 Ma EPMA monazite ages found by Dutch & Hand (2009) from Carnot Gneiss at Fishery Bay ~1 km east. The timing of peak to post-peak metamorphism is interpreted as 1693 ± 9 Ma.

At Black Point (Sample BP 2011-008) the relict high pressure assemblage has retrogressed to a cordierite-sapphirine-spinel-garnet assemblage. Monazite is microstructurally located within the matrix biotite and spinel-sapphirine-cordierite and therefore is interpreted to postdate the high pressure garnet-sapphirine assemblage. The majority of the analyses gave an average age of 1745 ± 14 Ma. The two old analyses 2365 ± 31 Ma (98 % concordancy) and 2201 ± 23 Ma (97 % concordancy) were located on a single monazite within retrogressive spinel-sapphirine of the matrix (Figure 11c: C). The rocks of the Carnot Gneiss record the *c.* 2480-2420 Ma Sleaford Orogeny (Fanning *et al.* 2007) and it is likely that these older analyses record this event and were only partially reset during the 1730-1690 Ma Kimban Orogeny. The concordant average age at 1745 ± 14 Ma is within error of the early

Kimban Orogeny and may indicate a longer duration of the Kimban than previously thought (Hand *et al.* 2007; Dutch *et al.* 2008; Payne *et al.* 2008). Another possibility is that like the older analyses this younger population of monazites were originally Sleafordian in age and were partially reset during the Kimban Orogeny.

Shoal Point

Metamorphism at Shoal Point and Shoal Point East is constrained to 1714 ± 7 Ma and 1706 ± 9 Ma respectively. The ages are similar to EPMA metamorphic monazite ages of *c.* 1700 Ma of by Dutch & Hand (2009).

Evidence of pre-Kimban metamorphism

Existing monazite EPMA and LA-ICPMS age data from within the Kalinjala Shear Zone and its flank to the west yields ages of *c.* 1760-1740 (Figure 17) (Dutch 2009; Dutch & Hand 2009; 2010; this study). All monazites were analysed in-situ and microstructurally constrained within the peak and/or retrograde assemblages. It is evident from Figure 17 that metamorphism is predominantly *c.* 1700 Ma in age, with the preservation of *c.* 2450 Ma Sleafordian metamorphism in parts of the Carnot Gneiss. Importantly there is no evidence for the metamorphic ages required by the *c.* 1850 Ma suture model of Stewart (2010).

An intriguing feature of the geochronology presented here is the presence of *c.* 1745 Ma monazite within the high Mg-Al metapelite in the Carnot Gneiss (Sample BP 2011-008), as well as minor evidence of similar aged monazite in some other samples along the southern coast of the Eyre Peninsula (Samples CG01, SP6 and ASE-01). These ages are older than what is typically assigned to the Kimban Orogeny (Bendall

1994; Myers *et al.* 1996; Hoek & Schaefer 1998; Tong *et al.* 2004; Dutch *et al.* 2008; Dutch 2009; Dutch & Hand 2010; Dutch *et al.* 2010) and their significance is unclear. One possibility is that they record an early stage of the Kimban Orogeny, which would make the event of at least 50 Ma in duration. However, monazite within the high Mg-Al metapelite (Sample BP 2011-008) was microstructurally located within the matrix assemblage that overprints the relic peak pressure assemblage of garnet-sillimanite-orthopyroxene. If the *c.* 1745 Ma monazite formed during the growth of the matrix, it implies that the peak pressure assemblage is older than *c.* 1745 Ma, providing some support for the suggestion above that the high pressure assemblage is pre-Kimban.

Rates of cooling across the Kalinjala Shear Zone

In this study the diffusion rates were used to assess cooling histories of two samples, one on the western flank of the shear zone at Shoal Point East and in the core of the shear zone at Bratten Cairn. At Shoal Point East garnet preserves a profile that requires cooling from a peak temperature of ~660 ºC through 300 ºC over 50 Myr. This is an average cooling rate of ~7 ºCMyr^{-1}.

Within the core of the Kalinjala Shear Zone at Bratten Cairn garnet diffusional modelling was not possible due to the near rim profile of garnets being modified by resorption. However the garnet core records a peak temperature of ~810 °C which has been preserved by the rock cooling faster than ~50 °CMyr^{-1}. While this is only an approximation due to the presence of rim resorption, it is generally consistent with the results obtained by Dutch (2009), who inferred cooling rates of ~60 °CMyr^{-1} in the core of the Kalinjala Shear Zone approximately 10 km south at Port Neill.

These cooling rate estimations provide evidence of differential exhumation across the Kalinjala Shear Zone. Cooling rates from the rocks at Bratten Cairn within the core of the shear zone indicate comparatively rapid cooling compared to Shoal Point East. This rapid cooling is interpreted to result from vertical movement of hot lower crustal rocks into the middle crust, along a near isothermal decompressional P-T evolution which is recorded by the P-T pseudosection in Figure 15.

Additionally, the compositional modelling of garnet can be used to make some general inferences about the peak metamorphic P-T conditions at Bratten Cairn. The required peak temperature needed to produce a garnet core composition of Figure 13b and 13d provides an additional constraint on the PT conditions shown in Figure 15. For the observed mineral assemblage of kyanite-rutile-ilmenite within garnet to be stable, the minimum pressure at ~810 ºC is 9.4 kbar. Furthermore the garnet composition at the rim corresponds to a temperature of ~500 ºC. If this temperature estimate is valid, the results of the cooling modelling imply that it would have taken no more than a few million years for the rocks at Bratten Cairn to have been exhumed from the lower crust. Using the mineral assemblages in BC 2011-011, with reference to the phase diagram in Figure 15, the decompressional history from > 9 kbar and ~810 ºC to around 5 kbar at temperatures > 500 ºC would have had to have been achieved in a few million years, suggesting that the core of the Kalinjala Shear Zone underwent comparatively rapid exhumation.

Metamorphism across the Kalinjala Shear Zone

Figure 17 shows a compilation of existing monazite EPMA and LA-ICPMS age data as well as metamorphic constraints and cooling data (Dutch *et al.* 2008; Dutch & Hand 2009; Dutch *et al.* 2010; this study). It is evident from Figure 17 that the metamorphism within the core and on the flanks of the shear zone is predominantly *c.* 1700 Ma in age with minor preservation of the *c.* 2450 Ma Sleafordian Orogeny within the Carnot Gneiss.

At Shoal Point, within the Carnot Gneiss, granulite facies peak metamorphism is constrained to 8-9 kbar at 820-850 ºC, followed by near isothermal decompression to metamorphic conditions < 6 kbar and 790-850 ºC (Dutch 2009). This P-T path is characterised as steeply decompressional (Figure 17.1).

Tong *et al.* (2004) and Dutch *et al.* (2010) have shown that the Carnot Gneiss records peak pressures of around 10 kbar, with the later formation of lower-pressure cordierite-bearing assemblages associated with the N-S trending KS2 fabric. This P-T evolution interpretation is consistent with the petrological relationships observed in sample BP 2011-008 which contains an early garnet-orthopyroxene-sillimanite assemblage and garnet contains inclusions of sapphirine and rutile. Subsequently orthopyroxene has been replaced by biotite-cordierite and sillimanite has been replaced by intergrowths of cordierite-spinel and cordierite-spinel-sapphirine in the presence of KS2 parallel biotite. The replacement of garnet-orthopyroxene-sillimanite by a later cordierite-spinel-sapphirine assemblage is consistent with high-temperature decompression (Kelsey *et al.* 2005). At present it is difficult to calculate the stability fields of spinel and sapphirine in P-T space (White *et al.* 2007). However, Kelsey *et*

al. (2005) modelled a similar reaction for the replacement of garnet-orthopyroxene-sillimanite-sapphirine by biotite-sapphirine-cordierite. This reaction is considered analogous enough to the mineral reaction observed in sample BP 2011-008 for the purpose of qualitatively describing the retrograde P-T path most likely experienced by the rocks during deformation. The reaction shows a large decrease in pressure over a small temperature range suggesting the retrogressive P-T path of the rock is steeply decompressional (Figure 17.2).

Mine Creek is located on the western flank of the shear zone. Peak metamorphic conditions are constrained to 6-7 kbar at *c.* 750 ºC with retrogressive conditions of 3-4 kbar at 600-660 ºC (Dutch 2009). These conditions define a shallower retrograde P-T path for Mine Creek compared to samples within the core of the shear zone (Figure 17.3).

The metapelitic assemblages at Bratten Cairn preserve peak metamorphic conditions of > 9 kbar and ~810 ºC. This was followed by rapid decompression to 5 kbar at temperatures > 500 ºC. These conditions define a steep decompressional P-T path in the core of the shear zone (Figure 17.4).

It is evident from Figure 17 that the metamorphic grade, rate of cooling and P-T path differs across the Kalinjala Shear Zone. The highest pressures and temperatures are observed in the Carnot Gneiss at Shoal Point (Figure 17.1) and Black Point (Figure 17.2), and to the north within the metapelitic rocks of Bratten Cairn (Figure 17.4). On the flank of the shear zone Mine Creek (Figure 17.3) is characterised by lower metamorphic grades and slower cooling. This pattern of isothermal decompression

within the shear zone but not outside it is indicative of differential exhumation across the shear zone.

The metapelitic assemblages at Bratten Cairn, coupled with existing P-T constraints from the Port Neill area south of Bratten Cairn (Dutch 2009), preserve evidence for a burial path to depths of around 30 km (i.e. 8-10 kbar; for typical crustal densities: 1 kbar = ~3.25 km), at temperatures > 750 ºC. This was followed by a steep decompressional path that lead to the formation of cordierite-bearing S2 assemblages at the expense of the earlier garnet-aluminosilicate assemblages. The absolute magnitude of the decompression is difficult to constrain, but appears to have been on the order of 5 kbar (= ~16 km).

Tong *et al.* (2004) and Dutch *et al.* (2010) have shown that the Carnot Gneiss records a quantitatively similar P-T evolution to that determined of the Bratten Cairn metasedimentary rocks. This path involved peak pressures of around 10 kbar, with the later formation of lower-pressure cordierite-bearing assemblages associated with the N-S trending KS2 fabric (Dutch *et al.* 2010). The KS2 fabric in the Carnot Gneiss is parallel to the trend of the Kalinjala Shear Zone in southern Eyre Peninsula and is interpreted to have formed in response to dextral transpression (Vassallo & Wilson 2002): Figure 3e. It is broadly correlated with the S2 fabric at Bratten Cairn which also records dextral shear at high grade conditions (Figure 2c and 2g). This structural correlation is strengthened by the *c.* 1700 Ma monazite ages obtained from the fabrics in both areas (Dutch & Hand 2009; Dutch *et al.* 2010; this study).

While at face value the metamorphic evolution in both regions appears similar, Dutch *et al.* (2010) showed that granulite-grade metamorphism also occurred in the Carnot Gneiss at *c.* 2450 Ma (Sleafordian Orogeny). The existence of this event is also suggested by the presence of minor amounts of old monazite in sample BP 2011-008. Dutch *et al.* (2010) interpreted the Sleafordian Orogeny as a comparatively low-pressure event that was overprinted by the high-pressure metamorphism associated with the Kimban Orogeny. The key constraint provided by Dutch *et al.* (2010) was the presence of cordierite-garnet-biotite assemblages in rocks with *c.* 2450 Ma monazite. However in order for these assemblages to be preserved during the later Kimban peak metamorphism requires that the Sleafordian cordierite survived meta-stably during the Kimban Orogeny. While this is possible in rocks that have been dehydrated, it is surprising that there is no evidence of secondary garnet growth at the expense of cordierite in these samples, as would have been expected on the basis of metamorphic phase relations (Dutch *et al.* 2010). Texturally Dutch *et al.* (2010) showed that cordierite postdates garnet in the *c.* 2450 Ma assemblages. Therefore it is possible that the cordierite in these assemblages is associated with the Kimban Orogeny and that the monazite did not recrystallise, preserving its original growth ages. Monazite has the potential to survive later metamorphism provided the rocks do not a) melt significantly, or b) experience fluid flow (e.g. Kelsey *et al.* 2008). If the texturally late cordierite is Kimban-aged, it suggests that the Sleafordian metamorphism may have been higher pressure that the Kimban overprint, whose main effect was to grow cordierite-spinel-biotite bearing assemblages at the expense of Sleafordian aged garnet-sillimanite-bearing assemblages.

If this suggestion is correct it implies that the decompressional paths recorded in the Carnot Gneiss may be artefacts of metamorphic overprinting between two unrelated events (e.g. Hand et al. 1992; Dutch et al. 2005). It also implies that the extent of exhumation associated with the Kimban Orogeny west of the Kalinjala Shear Zone is significantly less than previously suggested (Tong et al. 2004; Dutch et al. 2010) with Kimban pressures around 5 kbar, rather than 9 kbar. This possibility is more in line with the extent of exhumation west of the Kalinjala Shear Zone further north (Hand & Bendall 1995; Dutch et al. 2010), and the rapid decrease in metamorphic grade north of the Carnot Gneiss (Dutch *et al.* 2010). However in order to assess the possibility that the peak pressure metamorphism in the Carnot Gneiss is associated with Sleafordian metamorphism requires further work. One possibility is to directly date garnets associated with the relic peak pressure assemblage to see if they preserve evidence for ages older than Kimban. (Dutch & Hand 2010) showed that garnet cores preserved Sm-Nd ages of c. 2150 Ma which they interpreted to reflect partially reset Sleafordian ages, providing some support for the suggestion that peak pressures are Sleafordian. Another avenue for investigation would be to constrain the peak metamorphic conditions of the c. 2000 Ma Red Banks Charnockite within the Carnot Gneiss at Cape Carnot, ~2 km to the west of Black Point (Fanning 1997; Fanning et al. 2007). These intrusive rocks are associated with the c. 2000 Ma Miltalie Event and did not experience the Sleafordian Orogeny (Daly et al. 1998; Fanning et al. 2007). Therefore, peak metamorphic conditions preserved by the Red Banks Charnockite are likely to be related to the Kimban Orogeny and could be used clarify whether the Kimban Orogeny was a high-pressure or low-pressure event within the Carnot Gneiss.

Tectonic Implications

There have been several interpretations placed on the development and tectonic significance of the Kalinjala Shear Zone. Vassallo & Wilson (2002) interpreted the overall setting of the shear system to be dextral transpressional, with the shear zone forming an axial structure flanked by smaller scale shear zones to the east and fold systems to the west. Geophysical imaging (Thiel *et al.* 2005) suggest that the shear zone in it southern extent is subvertical to a depth of ~20 km , supporting the large-scale architecture suggested by Vassallo & Wilson (2002). More recently, Fraser *et al.* (Fraser *et al.* 2010b) interpreted the shear zone to be an extensional structure, based on seismic reflection imaging of moderately east-dipping structures across the northern segment of the shear zone. The extensional interpretation was based on the pattern of metamorphic grade change across the shear zone which shows that the highest grade rocks were located in the footwall. However the timing of exhumation of the high-grade rocks has not been established and could predate or postdate the development of the shear zone. Betts & Giles (2006) and Stewart (2010) interpreted the shear zone to be the suture between rocks to the east that they assigned to the North Australian Craton, and rocks to the west that they assigned to continental ribbons that collided with the North Australian Craton. Betts & Giles (2006) suggested that this collision occurred at *c.* 1700 Ma, while Stewart (2010) suggested that collision occurred at *c.* 1850 Ma associated with the Cornian Orogeny (Reid *et al.* 2008). In both cases the Kalinjala Shear Zone was interpreted to be a compressional-transpressional feature.

It is beyond the scope of this study to evaluate if the shear zone is a suture. However Szpunar & Fraser (2010) and Szpunar *et al.* (2011) showed that basin formation

occurred between *c.* 1790-1730 Ma on both sides of the shear zone and that basins to the west of the shear zone have detrital zircon ages similar to the *c.* 1850 Ma Donington Suite to the east. This suggests that the Donington Suite was proximal to the western basins by *c.*1790 Ma and, as a result, if the shear zone is a suture it predates *c.* 1790 Ma. This would support the model of Stewart (2010), although as indicated previously the presence of metasedimentary rocks within the shear zone with maximum depositional ages of < 1800 Ma would appear to rule out the interpretation of Stewart (2010). The lack of *c.* 1850 Ma metamorphic monazite on the Eyre Peninsula (Figure 17; Dutch 2009; Dutch & Hand 2009; 2010; this study) is also problematic for the model of Stewart (2010).

The exhumation of lower crustal rocks generally occurs through large-scale erosion of orogenic belts, or large-scale extension (Hill & Baldwin 1993; Carson *et al.* 1995; Thompson *et al.* 1997b, a; Fossen & Tikoff 1998; Konstantinovskaia & Malavieille 2005; Ring & Brandon 2008). In the central segment of the Kalinjala Shear Zone Bendall (1994), Hand & Bendall (1995) and Dutch & Hand (2009) showed that the high-pressure rocks appear to be restricted to a narrow domain along the trace of the shear zone (Thiel *et al.* 2005). Therefore, geophysically, the high-pressure rocks occur within a narrow subvertical domain that extends to at least 20 km depth. This structural configuration does not support the extensional model for the Kalinjala Shear Zone as suggested by Fraser *et al.* (2010b). One possibility is that the structures inferred by Fraser *et al.* (2010b) relate to deformation that preceded or postdates the main phase of deformation within the shear system.

The metamorphic data from Bratten Cairn indicates that the high-pressure rocks in the shear zone underwent a strongly decompressional path. This is in contrast to the rocks of the Mine Creek region that underwent only a minor cooling-decompression path (Dutch 2009). Additionally the rocks within the core of the shear zone appear to have cooled faster from peak temperatures than rocks on the flank (Dutch 2009; this study). At Bratten Cairn, cooling from a peak temperature of ~810 ºC was calculated to have occurred at > 50 $^{o}CMy^{-1}$. Interpretation of the P-T path for Bratten Cairn metasedimentary rock sample BC 2011-011 with reference to this cooling rate also implies exhumation from > 9 kbar to < 5 kbar occurred over a maximum of a few million years. This is a faster rate of exhumation than on the flank of the shear zone (Dutch 2009). Therefore it appears that not only does the core of the shear zone contains high pressure rocks, they were also exhumed more quickly than rocks on the flank of the shear zone.

One possibility is that the large amount of exhumation in the core of the shear zone is a record of extrusion. A number of workers (Fossen & Tikoff 1998; Tikoff & Peterson 1998; Goscombe *et al.* 2005; Jones *et al.* 2006) have suggested that transpression could lead to focussed exhumation of material within the cores of transpressional deformation systems. If these models apply to the Kalinjala Shear system then extrusion of the core of shear zone is consistent with the shear zone being a transpressional feature (e.g. Vassallo & Wilson 2002)).

Within the Kalinjala Shear Zone the high strain zone is approximately 5 km wide, and at the surface the fabrics are mostly sub-vertical and are dominated by dextral and flattening-style fabrics (Vassallo & Wilson 2002). However, the strain history is

complex with sinistral shear zones also developed parallel to the main foliation trend (this study). Metamorphically the shear zone contains lower crustal rocks (Bendall 1994; Hand & Bendall 1995; Tong *et al.* 2004; Dutch *et al.* 2008; Dutch 2009; this study) and appears to be flanked by lower pressure rocks on both sides. This simple metamorphic architecture is complicated by the exposure of high pressure rocks in the Carnot Gneiss west of the shear zone. However as discussed in this study there are ambiguities about whether these high grade rocks formed during an earlier and unrelated tectonic event.

CONCLUSIONS

U-Pb dating from metasedimentary rocks in the core of the Kalinjala Shear Zone indicates peak conditions of > 9 kbar at temperatures of around 810 ºC occurred at *c.* 1700 Ma during the Kimban Orogeny. Detrital zircon ages in the metasedimentary rocks of Bratten Cairn that contain the peak metamorphic assemblage indicate that maximum depositional ages were *c.* 1780 Ma. Garnet-biotite diffusional modelling suggests that the shear zone core cooled at > 50 ºCMyr^{-1} implying rapid exhumation of the core from depths of 30 km to mid-crustal levels (16 km). Modelling suggests that on the flanks of the shear zone exhumation and cooling rates were slower, and the maximum metamorphic pressures were less than in the core. The metamorphic constraints and age data from the core of the Kalinjala Shear Zone, combined with existing data, support a transpressional setting associated with the Kimban Orogeny. No evidence was found to support previously proposed models that include an extensional setting, or a *c.* 1850 Ma evolution of the shear system.

Where the shear zone reworks the early Paleoproterozoic Carnot Gneiss, early formed high pressure high temperature assemblages are overprinted by lower pressure granulite assemblages. The timing of the earlier high pressure assemblage is ambiguous, and could conceivably be related to the previously recognised *c.* 2450 Ma high-grade metamorphism in the Carnot Gneiss, and therefore not part of the Kimban-aged metamorphic architecture.

ACKNOWLEDGMENTS

I would like to thank my fantastic supervisor, Martin Hand for his help and advice throughout the year. Thank you to Dave Kelsey, Anthony Reid, Justin Payne, Katie Howard, Alec Walsh, Jade Anderson and Laura Morrissey for their endless assistance. Thank you to my family and friends for supporting me and putting up with my long absences. A very special mention to Josh, for always believing in me, being there to support me and cheering me up when I needed it. And cheers to the 2011 Honours group, you guys made this the best year and helped keep me sane!

REFERENCES

ALEINIKOFF J. N., SCHENCK W. S., PLANK M. O., SROGI L. A., FANNING C. M., KAMO S. L. & BOSBYSHELL H. 2006. Deciphering igneous and metamorphic events in high-grade rocks of the Wilmington Complex, Delaware: Morphology, cathodoluminescence and backscattered electron zoning, and SHRIMP U-Pb geochronology of zircon and monazite. *Geological Society of America Bulletin* **118**, 39-64.

BAROVICH K. & HAND M. 2008. Tectonic setting and provenance of the Paleoproterozoic Willyama Supergroup, Curnamona Province, Australia: Geochemical and Nd isotopic constraints on contrasting source terrain components. *Precambrian Research* **166**, 318-337.

BENDALL B. 1994. Metamorphic and geochronological constraints on the Kimban Orogeny, southern Eyre Peninsula. Honours thesis, School of Earth and Environmental Sciences, The University of Adelaide, Adelaide (unpubl.).

BETTS P. G. & GILES D. 2006. The 1800-1100 Ma tectonic evolution of Australia. *Precambrian Research* **144**, 92-125.

BOGER S. D. 2011. Antarctica — Before and after Gondwana. *Gondwana Research* **19**, 335-371.

BORG S. G. & DEPAOLO D. J. 1994. Laurentia, Australia, and Antarctica as a Late Proterozoic supercontinent - constraints from isotopic mapping. *Geology* **22**, 307-310.

CARSON C. J., DIRKS P., HAND M., SIMSON J. P. & WILSON C. J. L. 1995. Compressional and extensional tectonics in low-medium pressure granulites from the Larsemann Hills, East Antarctica. *Geological Magazine* **132**, 151-170.

CHERNIAK D. J. & WATSON E. B. 2001. Pb diffusion in zircon. *Chemical Geology* **172**, 5-24.

CHERNIAK D. J., WATSON E. B., GROVE M. & HARRISON T. M. 2004. Pb diffusion in monazite: a combined RBS/SIMS study. *Geochimica et Cosmochimica Acta* **68**, 829-840.

CUTTS K., HAND M. & KELSEY D. E. 2011. Evidence for early Mesoproterozoic (ca. 1590 Ma) ultrahigh-temperature metamorphism in southern Australia. *Lithos* **124**, 1-16.

DALY S. J. & FANNING C. M. (Editors) 1993. *Archean*. (The Geology of South Australia; Volume 1, The Precambrian Bulletin 54.). Geological Survey of South Australia.

DALY S. J., FANNING C. M. & FAIRCLOUGH M. C. (Editors) 1998. *Tectonic evolution and exploration potential of the Gawler Craton South Australia.* (Geology and Mineral Potential of Major Australian Mineral Provinces. AGSOJournal of Australian Geology and Geophysics, Vol. 17).

DALZIEL I. W. D. 1991. Pacific margins of Laurentia and East Antarctica-Australia as a conjugate rift pair - evidence and implications for an Eocambrian supercontient. *Geology* **19**, 598-601.

DUTCH R. 2009. Reworking the Gawler Craton: Metamorphic and geochronologic constraints on Palaeoproterozoic reactivation of the southern Gawler Craton, Australia. Doctor of Philosophy in the Faculty of Science thesis, School of Earth and Environmental Sciences, University of Adelaide, Adelaide (unpubl.).

DUTCH R. & HAND M. 2009. EPMA monazite constraints on the timing of deformation and metamorphism in the southern Kalinjala Shear Zone, Gawler Craton. *MESA Journal, PIRSA* **53**.

DUTCH R. & HAND M. 2010. Retention of Sm-Nd isotopic ages in garnets subjected to high-grade thermal reworking: implications for diffusion rates of major and rare earth elements and the Sm-Nd closure temperature in garnet. *Contributions to Mineralogy and Petrology* **159**, 93-112.

DUTCH R., HAND M. & KINNY P. D. 2008. High-grade Paleoproterozoic reworking in the southeastern Gawler Craton, South Australia. *Australian Journal of Earth Sciences* **55**, 1063-1081.

DUTCH R. A., HAND M. & CLARK C. 2005. Cambrian reworking of the southern Australian Proterozoic Curnamona Province: constraints from regional shear-zone systems. *Journal of the Geological Society* **162**, 763-775.

DUTCH R. A., HAND M. & KELSEY D. E. 2010. Unravelling the tectonothermal evolution of reworked Archean granulite facies metapelites using in situ geochronology: an example from the Gawler Craton, Australia. *Journal of Metamorphic Geology* **28**, 293-316.

EHLERS K. & POWELL R. 1994. An empirical modification of Dodson equation for closure temperature in binary-systems. *Geochimica et Cosmochimica Acta* **58**, 241-248.

EHLERS K., POWELL R. & STUWE K. 1994. Cooling rate histories from garnet plus biotite equilibrium. *American Mineralogist* **79**, 737-744.

FAIRCLOUGH M. C. & DALY S. J. 1995. *Interpreted basement geology for the western Gawler Craton. South Australian Department of Mines and Energy, Digital Data Set (unpublished)* Energy S. A. D. o. M. a.

FANNING C. M. 1995. *Geochronological synthesis of southern Australia. Part II. The Gawler Craton. South Australia. Open file Envelope, 8918 (unpublished).* Department of Mines and Energy Resources.

FANNING C. M. 1997. Geological synthesis of southern Australia. Part II: The Gawler Craton. South Australia. Open file Envelope, 8918 (unpublished). *Department of Primary Industries and Resources South Australia*.

FANNING C. M., FLINT R. B., PARKER A. J., LUDWIG K. R. & BLISSETT A. H. 1988. Refined Proterozoic evolution of the Gawler Craton, South Australia, through U-Pb zircon geochronology. *Precambrian Research* **40-41**, 363-386.

FANNING C. M., REID A. J. & G.S. T. 2007. *A geochronological framework for the Gawler Craton, South Australia.* Survey S. A. G.**:** 55.

FERRIS G. M., SCHWARZ M. P. & HEITHERSAY P. (Editors) 2002. *The geological framework, distribution and controls of Fe-oxide and related alteration, and Cu-Au mineralisation in the Gawler Craton South Australia. Part I: geological and tectonic framework.* . (Hydrothermal Iron Oxide Copper-Gold and Related Deposits: A Global Perspective.). PGC Publishing, Adelaide.

FLÖTTMANN T. & OLIVER R. 1994. Review of Precambrian-Palaeozoic relationships at the craton margins of southeastern Australia and adjacent Antarctica. *Precambrian Research* **69**, 293-306.

FOSSEN H. & TIKOFF B. 1998. Extended models of transpression/transtension and application to tectonic settings. . *in Continental Transpression and Transtension Tectonics*, 15-33.

FRASER G., MCAVANEY S., NEUMANN N., SZPUNAR M. & REID A. 2010a. Discovery of early Mesoarchean crust in the eastern Gawler Craton, South Australia. *Precambrian Research* **179**, 1-21.

FRASER G. L., BLEWETT R. S., REID A., KORSCH R. J., DUTCH R., NEUMANN N., MEIXNER A. J., SKIRROW R. G., COWLEY W. M., SZPUNAR M., PREISS W. V., FOMIN T., HOLZSCHUH J., THIEL S., MILLIGAN P. R. & BENDALL B. R. 2010b. *Geological interpretation of deep seismic reflection and magnetotelluric line 08GA-G1: Eyre Peninsula, Gawler Craton, South Australia*. Geological Survey P., Adelaide.

GANGULY J., CHENG W. J. & CHAKRABORTY S. 1998. Cation diffusion in aluminosilicate garnets: experimental determination in pyrope-almandine diffusion couples. *Contributions to Mineralogy and Petrology* **131**, 171-180.

GOODGE J. W. & FANNING C. M. 2010. Composition and age of the East Antarctic Shield in eastern Wilkes Land determined by proxy from Oligocene-Pleistocene glaciomarine sediment and Beacon Supergroup sandstones, Antarctica. *Geological Society of America Bulletin* **122**, 1135-1159.

GOSCOMBE B., GRAY D. & HAND M. 2005. Extrusional tectonics in the core of a transpressional orogen; the Kaoko Belt, Namibia. *Journal of Petrology* **46**, 1203-1241.

GOSCOMBE B. D., PASSCHIER C. W. & HAND M. 2004. Boudinage classification: end-member boudin types and modified boudin structures. *Journal of Structural Geology* **26**, 739-763.

GRIFFIN W. L., POWELL W. J., PEARSON N. J. & O'REILLY S. Y. (Editors) 2008. *GLITTER: data reduction software for laser ablation ICP-MS*. (In: Sylvester, P. (Ed.), Laser Ablation ICP-MS in the Earth Sciences: Current Practices and Outstanding Issues. Mineralogical Association of Canada. Short Course Series 40, pp. 308–311.).

HAND M. & BENDALL B. R. 1995. Metamorphic evidence for Paleoproterozoic oblique convergence in the eastern Gawler Craton. *Geological Society of Australia Abstracts 40*, 59.

HAND M., DIRKS P., POWELL R. & BUICK I. S. 1992. How well established is isobaric cooling in Proterozoic orogenic belts - an example from the Arunta Inlier, Central Australia. *Geology* **20**, 649-652.

HAND M., REID A. & JAGODZINSKI L. 2007. Tectonic framework and evolution of the Gawler craton, southern Australia. *Economic Geology* **102**, 1377-1395.

HAUZENBERGER C. A., ROBL J. & STUWE K. 2005. Garnet zoning in high pressure granulite-facies metapelites, Mozambique belt, SE-Kenya: constraints on the cooling history. *European Journal of Mineralogy* **17**, 43-55.

HILL E. J. & BALDWIN S. L. 1993. Exhumation of high-pressure metamorphic rocks during crustal extension in the Dentrecasteauz Region, Papua-New Guinea. *Journal of Metamorphic Geology* **11**, 261-277.

HOEK J. D. & SCHAEFER B. F. 1998. Palaeoproterozoic Kimban mobile belt, Eyre Peninsula: timing and significance of felsic and mafic magmatism and deformation. *Australian Journal of Earth Sciences* **45**, 305-313.

HOLLAND T. & POWELL R. 2003. Activity-composition relations for phases in petrological calculations: an asymmetric multicomponent formulation. *Contributions to Mineralogy and Petrology* **145**, 492-501.

HOLLAND T. J. B. & POWELL R. 1998. An internally consistent thermodynamic data set for phases of petrological interest. *Journal of Metamorphic Geology* **16**, 309-343.

HOWARD K. E. 2006. Honours Thesis (unpublished). Earth and Environmental Sciences, University of Adelaide (unpubl.).

HOWARD K. E., HAND M., BAROVICH K. M., REID A., WADE B. P. & BELOUSOVA E. A. 2009. Detrital zircon ages: Improving interpretation via Nd and Hf isotopic data. *Chemical Geology* **262**, 277-292.

JACKSON S. E., PEARSON N. J., GRIFFIN W. L. & BELOUSOVA E. A. 2004. The application of laser ablation-inductively coupled plasma-mass spectrometry to in situ U–Pb zircon geochronology. *Chemical Geology* **211**, 47-69.

JONES R. R., HOLDSWORTH R. E., HAND M. & GOSCOMBE B. 2006. In: Law, R.D., Searle, M.P., Godin, L. (eds). Channel Flow, Ductile Extrusion and Exhumation in Continental Collision Zones. . *Geological Society, London, Special Publications, 268*, 201-219.

KAWAKAMI T. & HOKADA T. 2010. Linking P-T path with development of discontinuous phosphorus zoning in garnet during high-temperature metamorphism - an example from Lutzow-Holm Complex, East Antarctica. *Journal of Mineralogical and Petrological Sciences* **105**, 175-186.

KAWAKAMI T. & MOTOYOSHI Y. 2004. Timing of attainment of the spinel plus quartz coexistence in garnet-sillimanite leucogneiss from Skallevikshalsen, Lutzow-Holm Complex, East Antarctica. *Journal of Mineralogical and Petrological Sciences* **99**, 311-319.

KELSEY D. E., CLARK C. & HAND M. 2008. Thermobarometric modelling of zircon and monazite growth in melt-bearing systems: examples using model metapelitic and metapsammitic granulites. *Journal of Metamorphic Geology* **26**, 199-212.

KELSEY D. E., WHITE R. W. & POWELL R. 2005. Calculated phase equilibria in K2O-FeO-MgO-Al2O3-SiO2-H2O for silica-undersaturated sapphirine-bearing mineral assemblages. *Journal of Metamorphic Geology* **23**, 217-239.

KOHN M. J. & SPEAR F. 2000. Retrograde net transfer reaction insurance for pressure-temperature estimates. *Geology* **28**, 1127-1130.

KONSTANTINOVSKAIA E. & MALAVIEILLE J. 2005. Erosion and exhumation in accretionary orogens: Experimental and geological approaches. *Geochemistry Geophysics Geosystems* **6**.

MARMO B. 1993. The structural development and retrograde cooling history of the Bratten Cairn area, South Australia. Bachelor of Science (Honours) thesis, Department of Geology, University of Melbourne, Melbourne (unpubl.).

MOORES E. M. 1991. Southwest United-States-East Antarctica (SWEAT) connection - a hypothesis *Geology* **19**, 425-428.

MYERS J. S., SHAW R. D. & TYLER I. M. 1996. Tectonic evolution of Proterozoic Australia. *Tectonics* **15**, 1431-1446.

PARKER A. J. 1993. *Paleoproterozoic*. Australia G. S. o. S. **1:** 50-105.

PARKER A. J. & LEMON N. M. 1982. Reconstruction of the early Proterozoic stratigraphy of the Gawler Craton, South Australia. *Journal of the Geological Society of Australia* **29**, 221-238.

PAYNE J. L., BAROVICH K. A. & HAND M. 2006a. Provenance of metasedimentary rocks in the northern Gawler Craton, Australia: Implications for palaeoproterozoic reconstructions. *Precambrian Research* **148**, 275-291.

PAYNE J. L., FERRIS G., BAROVICH K. M. & HAND M. 2010. Pitfalls of classifying ancient magmatic suites with tectonic discrimination diagrams: An example from the Paleoproterozoic Tunkillia Suite, southern Australia. *Precambrian Research* **177**, 227-240.

PAYNE J. L., HAND M., BAROVICH K. M. & WADE B. P. 2008. Temporal constraints on the timing of high-grade metamorphism in the northern Gawler Craton:

implications for assembly of the Australian Proterozoic. *Australian Journal of Earth Sciences* **55**, 623-640.

PAYNE J. L., HAND M., BAVORICH K. M., REID A. & EVANS D. A. D. 2009. Correlations and reconstruction models for the 2500-1500 Ma evolution of the Mawson Continent. *Geological Society special publication (0305-8719), 323 (1) p. 319.*

PAYNE J. L., WADE B. P., HAND M., BAROVICH K. & CLARK C. 2006b. Optimising the spatial resolution, fractionation and temporal precision of monazite U-Pb LA-ICP-MS geochronology. *Geochimica et Cosmochimica Acta* **70**, A476-A476.

PEUCAT J. J., MENOT R. P., MONNIER O. & FANNING C. M. 1999. The Terre Adelie basement in the East-Antarctica Shield: geological and isotopic evidence for a major 1.7 Ga thermal event; comparison with the Gawler Craton in South Australia. *Precambrian Research* **94**, 205-224.

POWELL R. & HOLLAND T. J. B. 1988. An internally consistent thermodynamic dataset with uncertainties and correlations: 3. Applications to geobarometry, worked examples and a computer program. *Journal of Metamorphic Geology* **6**, 173-204.

REID A., HAND M., JAGODZINSKI E., KELSEY D. & PEARSON N. 2008. Paleoproterozoic orogenesis in the southeastern Gawler Craton, South Australia. *Australian Journal of Earth Sciences* **55**, 449-471.

RING U. & BRANDON M. T. 2008. Exhumation settings, part I: Relatively simple cases. *International Geology Review* **50**, 97-120.

ROBL J., HERGARTEN S., STUWE K. & HAUZENBERGER C. 2007. THERMAL HISTORY: A new software to interpret diffusive zoning profiles in garnet. *Computers & Geosciences* **33**, 760-772.

RUBATTO D., HERMANN J., RG & BUICK I. S. 2006. Temperature and Bulk Composition Control on the Growth of Monazite and Zircon During Low-pressure Anatexis (Mount Stafford, Central Australia). *Journal of Petrology* **47**, 1973-1996.

RUBATTO D., WILLIAMS I. S. & BUICK I. S. 2001. Zircon and monazite response to prograde metamorphism in the Reynolds Range, central Australia. *Contributions to Mineralogy and Petrology* **140**, 458-468.

SCHWARZ M. 2003. *LINCOLN map sheet. South Australia. Geological Survey. Geological Atlas 1:250 000 Series – Explanatory Notes.*

. Geological Survey P., Adelaide.

SCHWARZ M., BAROVICH K. M. & HAND M. 2002. *A plate margin setting for the evolution of the southern Gawler Craton evidence from detrital zircon and Sm-Nd isotopic data of the Hutchison Group. In: Preiss, W.V. (Ed.), Geoscience 2002: Expanding Horizons 16th Australian Geological Convention. Adelaide Convention Centre, Adelaide, S.A. Australia, p. 70.*, Adelaide.

SLÁMA J., KOSLER J., CONDON D. J., CROWLEY J. L., GERDES A., HANCHAR J. M., HORSTWOOD M. S. A., MORRIS G. A., NASDALA L., NORBERG N., SCHALTEGGER U., SCHOENE B., TUBRETT M. N. & WHITEHOUSE M. J. 2008. Plesovice zircon -- A new natural reference material for U-Pb and Hf isotopic microanalysis. *Chemical Geology* **249**, 1-35.

STEWART J. R. 2010. Chapter 7: Deformation sequence preserved within the Paleoproterozoic central Kalinjala Shear Zone: Continental transcurrent reactivation of a major extensional structure? School of Geosciences, Monash University (unpubl.).

STEWART J. R. & BETTS P. G. 2010. Late Paleo-Mesoproterozoic plate margin deformation in the southern Gawler Craton: Insights from structural and aeromagnetic analysis. *Precambrian Research* **177**, 55-72.

SWAIN G., WOODHOUSE A., HAND M., BAROVICH K., SCHWARZ M. & FANNING C. M. 2005a. Provenance and tectonic development of the late Archaean Gawler Craton, Australia; U-Pb zircon, geochemical and Sm-Nd isotopic implications. *Precambrian Research* **141**, 106-136.

SWAIN G. M., HAND M., TEASDALE J., RUTHERFORD L. & CLARK C. 2005b. Age constraints on terrane-scale shear zones in the Gawler Craton, southern Australia. *Precambrian Research* **139**, 164-180.

SZPUNAR M. & FRASER G. L. 2010. *Age of deposition and provenance of Paleoproterozoic basins on the north-eastern Eyre Peninsula South Australia*. Resources D. o. P. I. a., Adelaide.

SZPUNAR M., HAND M., BAROVICH K., JAGODZINSKI E. & BELOUSOVA E. 2011. Isotopic and geochemical constraints on the Paleoproterozoic Hutchison Group, southern Australia: Implications for Paleoproterozoic continental reconstructions. *Precambrian Research* **187**, 99-126.

THIEL S., HEINSON G. & WHITE A. 2005. Tectonic evolution of the southern Gawler Craton, South Australia, from electromagnetic sounding. *Australian Journal of Earth Sciences* **52**, 887-896.

THOMPSON A. B., SCHULMANN K. & JEZEK J. 1997a. Extrusion tectonics and elevation of lower crustal metamorphic rocks in convergent orogens. *Geology* **25**, 491-494.

THOMPSON A. B., SCHULMANN K. & JEZEK J. 1997b. Thermal evolution and exhumation in obliquely convergent (transpressive) orogens. *Tectonophysics* **280**, 171-184.

TIKOFF B. & PETERSON K. 1998. Physical models of transpressional folding. . *Journal of Structural Geology* **20**.

TONG L., WILSON C. J. L. & VASSALLO J. J. 2004. Metamorphic evolution and reworking of the Sleaford Complex metapelites in the southern Eyre Peninsula, South Australia. *Australian Journal of Earth Sciences* **51**, 571-589.

VASSALLO J. J. & WILSON C. J. L. 2001. Structural repetition of the Hutchison Group metasediments, Eyre Peninsula, South Australia. *Australian Journal of Earth Sciences* **48**, 331-345.

VASSALLO J. J. & WILSON C. J. L. 2002. Palaeoproterozoic regional-scale non-coaxial deformation: an example from eastern Eyre Peninsula, South Australia. *Journal of Structural Geology* **24**, 1-24.

VAVRA G. & SCHALTEGGER U. 1999. Post-granulite facies monazite growth and rejuvenation during Permian to Lower Jurassic thermal and fluid events in the Ivrea Zone (Southern Alps). *Contributions to Mineralogy and Petrology* **134**, 405-414.

VEEVERS J. J., WALTER M. R. & SCHEIBNER E. 1997. Neoproterozoic tectonics of Australia-Antarctica and Laurentia and the 560 Ma birth of the Pacific Ocean reflect the 400 my Pangean supercycle. *Journal of Geology* **105**, 225-242.

WADE B. P., PAYNE J. L., HAND M. & BAROVICH K. M. 2007. Petrogenesis of ca 1.50 Ga granitic gneiss of the Coompana Block: filling the 'magmatic gap' of Mesoproterozoic Australia. *Australian Journal of Earth Sciences* **54**, 1089-1102.

WHITE R. W., POWELL R. & CLARKE G. L. 2002. The interpretation of reaction textures in Fe-rich metapelitic granulites of the Musgrave Block, central

Australia: constraints from mineral equilibria calculations in the system K2O-FeO-MgO-Al2O3-SiO2-H2O-TiO2-Fe2O3. *Journal of Metamorphic Geology* **20**, 41-55.

WHITE R. W., POWELL R. & HOLLAND T. J. B. 2001. Calculation of partial melting equilibria in the system Na2O-CaO-K2O-FeO-MgO-Al2O3-SiO2-H2O (NCKFMASH). *Journal of Metamorphic Geology* **19**, 139-153.

WHITE R. W., POWELL R. & HOLLAND T. J. B. 2007. Progress relating to calculation of partial melting equilibria for metapelites. *Journal of Metamorphic Geology* **25**, 511-527.

WHITE R. W., POWELL R., HOLLAND T. J. B. & WORLEY B. A. 2000. The effect of TiO2 and Fe2O3 on metapelitic assemblages at greenschist and amphibolite facies conditions: mineral equilibria calculations in the system K2O-FeO-MgO-Al2O3-SiO2-H2O-TiO2-Fe2O3. *Journal of Metamorphic Geology* **18**, 497-511.

ZHAO G. C., CAWOOD P. A., WILDE S. A. & SUN M. 2002. Review of global 2.1-1.8 Ga orogens: implications for a pre-Rodinia supercontinent. *Earth-Science Reviews* **59**, 125-162.

FIGURE CAPTIONS

1. Interpreted strike of Kalinjala Shear Zone on the Eyre Peninsula overlain on aeromagnetic Total Magnetic Intensity image (adapted from Schwarz 2003; Dutch et al. 2010). Sample locations are labelled.
2. Photographs of field structures at Bratten Cairn: (A) peak metamorphic (S1) granoblastic fabric preserved in boudins. (B) Garnet porphyroblast within leucomsome partially replaced by orthopyroxene and plagioclase. (C) Boudin containing peak S1 fabric. Fabric wrapping the boudin gives (S4) sinistral shear sense. Sharp boundary between the S1 fabric and wrapping fabric is not consistent with progressive shear band boudinaged, boudin is interpreted as originally S2 dextral domino boudin that was later reworked by S4 sinistral shear (Goscombe et al. 2004). (D) S2 coarse-grained fabric. (E) Pegmatite intrusive along S4 mylonitic shear band overprinting S2. (F) Complex folding. (G) Dextral S3 mylonitic reworking. (H) Pegmatite with S4 sinistral shear fabric.
3. Photographs of field structures within the Carnot Gneiss: (A) KD1 peak metamorphic mineral assemblage garnet-orthopyroxene-plagioclase-biotite. (B) Garnetiferous KD1 peak metamorphic assemblage. (C) Flat KD1 fabric reworked by high strain zone of KD2. (D) KD1 fabric folded and reworked by KD2 high strain zone. (E) Garnet porphyroblast, dextral shear. (F) Partial melting within KD2 high strain zone. (G) Melting crosscutting KD2 gneissic fabric with patches of retrograde cordierite. (H) decompressional-style mineral assemblage of blue cordierite replacing garnet.

4. Bratten Cairn petrological images, scale refers to width of picture: (a) IGC24: inclusions of sillimanite within garnet porphyroblast. (b) IGC24: perthitic feldspar and biotite. (c) IGC29: sillimanite-spinel defining S2 fabric. (d) IGC31: orthopyroxene-plagioclase-garnet-biotite segregation boudinaged by S2 biotite. (e) Plagioclase moat around garnet within orthopyroxene. (f) IGC31: plagioclase and quartz ribbons defining S3.
5. Bratten Cairn petrological images, scale refers to width of picture: (a) IGC33: garnet porphyroblasts within granoblastic S2 fabric and parallel S3 biotite and dynamically recrystallised quartz and plagioclase. (b) BC 2011-011: Garnet with inclusions of kyanite, rutile and ilmenite. (c) BC 2011-011: kyanite grain within garnet displaying prominent 75º cleavage and spinel along grain boundary. (d) BC 2011-011: cross-polarised view of garnet with inclusions of sillimanite and cordierite. (e) BC 2011-011: cross-polarised view of high birefringence sillimanite pseudomorph of kyanite. (f) BC 2011-011: within garnet, ilmenite with coronas of rutile. (g) BC 2011-011: cordierite replacing garnet. (h) BC 2011-011: cordierite with inclusions of sillimanite.

6. Carnot Gneiss petrological images, scale refers to width of picture: (a) BP 2011-008: KS1 coarse biotite crosscut by KS2 biotite with dextral shear, KS1 and KS2 biotite-cordierite association replacing garnet, relic orthopyroxene present. (b) BP 2011-008: sapphirine and rutile inclusions in garnet (c) BP 2011-008: intergrowth of cordierite-spinel-sapphirine weakly elongate along KS2 fabric. (d) BP 2011-008: sapphirine-spinel-cordierite intergrowth with symplectic texture. (e) IGC44/CG01: elongate garnet grains embayed by cordierite. (f) IGC44/CG01: spinel within cordierite, elongate to the foliation, relic sillimanite. (g) SP9: garnet with inclusion-rich core and inclusion-free rim indicative of 2 stages of garnet growth.
7. (a) IGC31: Concordia plot of all zircon analyses. (b) IGC31: Concordia plot of 90-110% concordant analyses. (c) IGC31: Probability distribution of $^{207}Pb/^{206}Pb$ ages, (grey) concordant zircon analyses and (white) all zircon analyses, maximum depositional age and dominant age peaks labelled. (d) IGC31: Zircon CL images with analytical spots and $^{207}Pb/^{206}Pb$ age; A: zircon representative of youngest population showing bright zone and a dark metamorphic rim; B: ~1860 Ma zircon population, euhedral with clear luminescent core; C: ~2400 Ma zircon population with dark core; D: (030-15) ~1900 Ma zircon, (030-33) Kimban-aged metamorphic overgrowth.

8. (a) IGC33: Concordia plot of all zircon analyses, highly discordant zircon grains. (b) IGC33: Concordia plot of 90-110% concordant analyses. (c) IGC33: Probability distribution of $^{207}Pb/^{206}Pb$ ages, (grey) concordant zircon analyses and (white) all zircon analyses, maximum depositional age and dominant age peaks labelled. (d) IGC33: Zircon CL images with analytical spots and $^{207}Pb/^{206}Pb$ age; A: zircon representative of youngest population showing 'soft' luminescence characteristic of metamorphic recrystallisation; B: ~2550 Ma zircon population, euhedral with clear core; C: ~2550 Ma zircon population with concentric zoning.
9. (a) IGC24: Concordia plot of 90-110% monazite analyses, inset: mean weighted average $^{207}Pb/^{206}Pb$ data. (b) IGC24: Monazite backscatter electron image showing dark core and light rim with $^{207}Pb/^{206}Pb$ age analysis location. (c) IGC29: Concordia plot of 90-110% monazite analyses inset: mean weighted average $^{207}Pb/^{206}Pb$ data. (d) IGC29 (A-B): Monazite backscatter electron images showing dark core and light rim with $^{207}Pb/^{206}Pb$ age analysis location. (e) BC 2011-011: Concordia plot of 90-110% monazite analyses inset: mean weighted average $^{207}Pb/^{206}Pb$ data. (f) BC 2011-011: Thin section image of monazite texturally located within garnet with analysis locations and $^{207}Pb/^{206}Pb$ age data.

10. (a) IGC44: Concordia plot of all zircon analyses, highly discordant zircon grains. (b) IGC44: Zircon CL images with analytical spots and $^{207}Pb/^{206}Pb$ age; A: representative zircon grains of ~2600 Ma population; B: Representative zircon of metamorphic resetting with featureless zones. (c) IGC44: Probability distribution of $^{207}Pb/^{206}Pb$ ages, (grey) concordant zircon analyses and (white) all zircon analyses, maximum depositional age labelled. (d) CG01: Concordia plot of 90-110% monazite analyses, inset: mean weighted average $^{207}Pb/^{206}Pb$ data. (e) CG01: A: Monazite backscatter electron image showing core and with light recrystallised rim with $^{207}Pb/^{206}Pb$ age analysis location; B: Monazite backscatter electron image showing homogeneous chemical zonation and $^{207}Pb/^{206}Pb$ age analysis locations.
11. (a) BP 2011-008: Concordia plot of all 90-110% monazite analyses. (b) BP 2011-008: Concordia plot of younger population of 90-110% monazite analyses, inset: mean weighted average $^{207}Pb/^{206}Pb$ data. (c) BP 2011-008: A: Thin section image of monazite texturally within biotite with analysis locations and $^{207}Pb/^{206}Pb$ age data B: Thin section image of monazite texturally within biotite with analysis locations and $^{207}Pb/^{206}Pb$ age data C: Thin section image of monazite texturally within spinel with analysis locations and $^{207}Pb/^{206}Pb$ age data.

12. (a) SP6: Concordia plot of all 90-110% monazite analyses; inset: mean weighted average $^{207}Pb/^{206}Pb$ data. (b) SP6: Thin section image of monazite texturally within cordierite with analysis locations and $^{207}Pb/^{206}Pb$ age data. (c) SP7: Concordia plot of all 90-110% monazite analyses; inset: mean weighted average $^{207}Pb/^{206}Pb$ data. (d) SP7 (A-C): Homogenous monazite backscatter electron image (for A and C inset of textural location within garnet) and $^{207}Pb/^{206}Pb$ age analysis location.
13. IGC24 (Garnet A): (a) Thin section image of garnet transect. (b) XMg = Mg/(Mg + Fe) diffusional-based cooling estimates calculated with different starting peak temperatures of 800 ºC, 810 ºC and 820 ºC, compared to the measured transect with the best fit given by 810 ºC. (c) Cooling rate associated with the calculated cooling estimates. (d) Transect across garnet displaying end member compositions. Resorption on the rims is interpreted from the increase in X(spss). X(alm) and X(py) are scaled on the primary (left hand) axis, X(grs) and X(spss) are scaled on the secondary (right) axis.
14. ASE-01 (Garnet A): (a) Thin section image of garnet transect. (b) XMg = Mg/(Mg + Fe) diffusional-based cooling estimates calculated using a power law with different peak temperatures of 677 ºC, 667 ºC, 657 ºC, 647 ºC and 627 ºC compared to the measured transect with the best fit given by 657 ºC. (c) Power law cooling rate associated with the calculated cooling estimates. (d) Transect across garnet displaying end member compositions.
15. Calculated P-T pseudosection for sample BC 2011-011. The arrow describes the interpreted evolution of the sample in P-T space.

16. Probability density plots of detrital zircon $^{207}Pb/^{206}Pb$ age populations compared to Eyre Peninsula metasedimentary packages, major peaks highlighted (a) IGC33. (b) IGC31. (c) Mangalo Schist, Cleve Group (Szpunar *et al.* 2011) (d) Darke Peak Group, Cleve Group (Szpunar *et al.* 2011). (e) IGC44 (f) Carnot Gneiss, Sleaford Complex (Szpunar *et al.* 2011).
17. Interpreted subsurface geology of the southern Eyre Peninsula overlain on the total magnetic intensity image (modified from Schwarz 2003; Dutch et al. 2010). Monazite data at sample locations: Red = This study (LA-ICPMS), White = EPMA (2009)Green = EPMA Dutch & Hand (2009), Blue = EPMA Dutch et al. (2010).

    17.1 Shoal Point P-T pseudosection describes a steep decompressional path with associated metamorphic constraints described (Dutch et al. 2010).

    17.2 Black Point P-T pseudosection describes a high pressure assemblage retrogressed through a steep decompressional path with associated metamorphic constraints described (Kelsey et al. 2005).

    17.3 Mine Creek pseudosection P-T pseudosection describes a shallower P-T path with lower cooling rates and with associated metamorphic constraints described (Dutch 2009).

    17.4 BC 2011-011 P-T pseudosection describes a high pressure assemblage retrogressed during near isothermal decompression with associated metamorphic constraints described (this study).

TABLE CAPTIONS

1. Raw bulk geochemical data from analysis for sample BC 2011-011.
2. Summary of garnet and biotite compositions analysed by electron microprobe.
3. Garnet-biotite modelling parameters for samples IGC24 and ASE-01.

IDENT	SiO2	TiO2	Al2O3	Fe2O3	MnO	MgO	CaO	Na2O	K2O	LOI	P2O5
UNITS	%	%	%	%	%	%	%	%	%	%	%
BP 2011-011	66.9	0.45	15.4	5.6	0.07	2.54	2.56	3.42	1.51	0.2	0.03

Table 1

	IGC24	IGC24	IGC24	ASE-01	ASE-01	ASE-01
	Biotite	Garnet Rim	Garnet Core	Biotite	Garnet Rim	Garnet Core
SiO2	35.811	36.6753	37.8115	32.625	36.4219	36.5438
TiO2	3.333	0.0594	0.0201	2.924	0.0396	0.0205
Al2O3	16.694	21.1069	21.5361	17.340	21.0768	21.1661
Cr2O3	0.032	0.0037	0.0027	0.036	0.0235	0.0297
FeO	14.063	32.9701	29.454	20.694	35.2575	33.6195
MnO	0.038	0.6574	0.4611	0.107	3.0993	2.5304
MgO	13.471	6.0761	8.7286	11.766	2.7753	4.3659
ZnO	0.003	0.0813	0.0002	0.077	0.074	0.0191
CaO	0.000	0.6684	0.7114	0.018	1.3092	1.2798
Na2O	0.067	0.0003	0.0096	0.097	0.0003	0.0023
K2O	9.626	0.0247	0.0076	6.238	0.0206	0.0009
V2O3	0.073	0.0002	0.03	0.064	0.0203	0.0731
ZrO2	0.000	0.0002	0.0223	0.041	0.0002	0.0216
SrO	0.000	0	0	0.000	0	0
BaO	0.000	0	0	0.000	0	0
NiO	0.000	0	0	0.000	0	0

Table 2

Sample	IGC24	ASE-01
Temperature Step (K)	1	1
number of nodes	1000	1000
XMg biotite	0.64	0.5
Start temperature (°C)	810	657
End temperature (°C)	300	300

Table 3

Figure 1 Eyre Peninsula. (Inset: Gawler Craton)

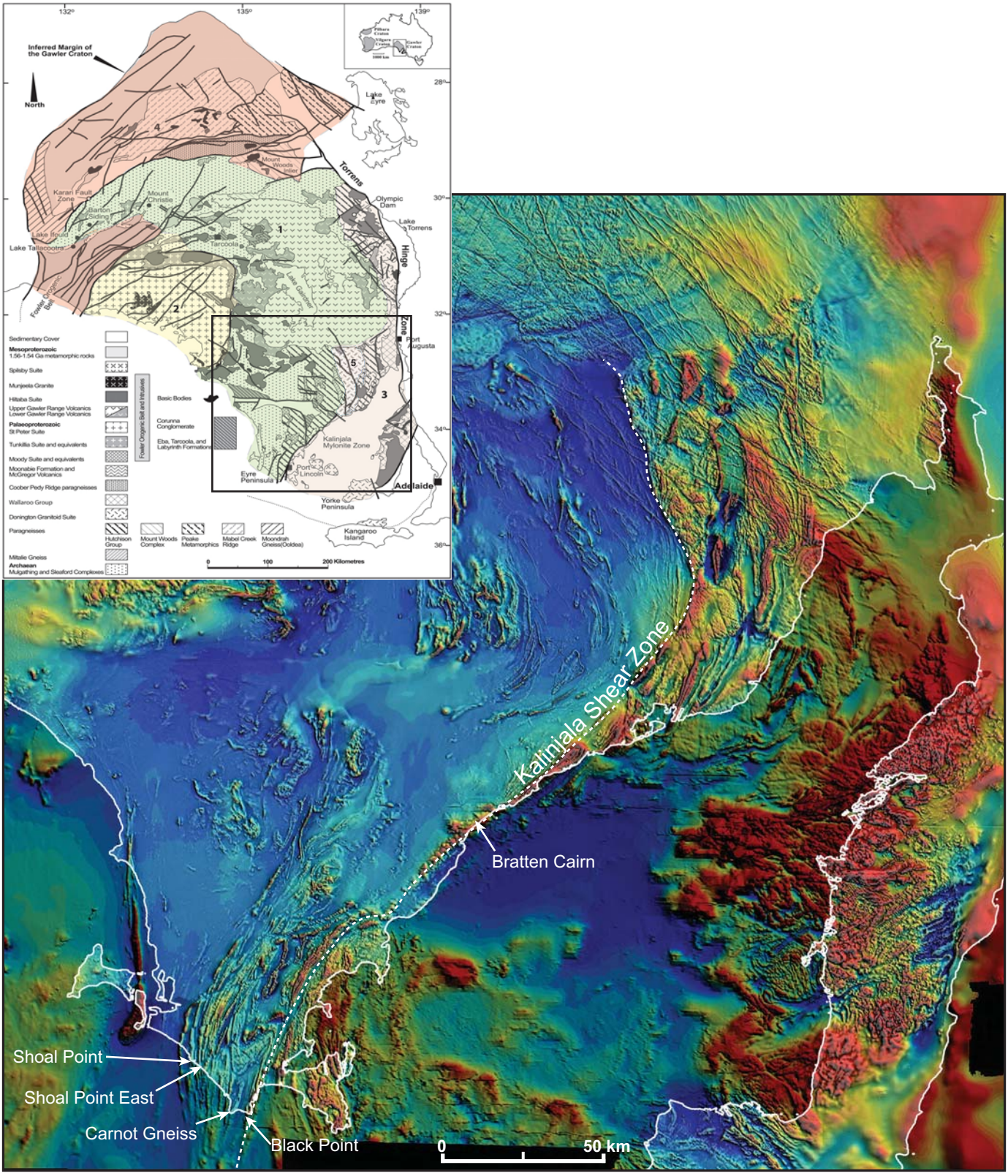

Figure 2 Bratten Cairn

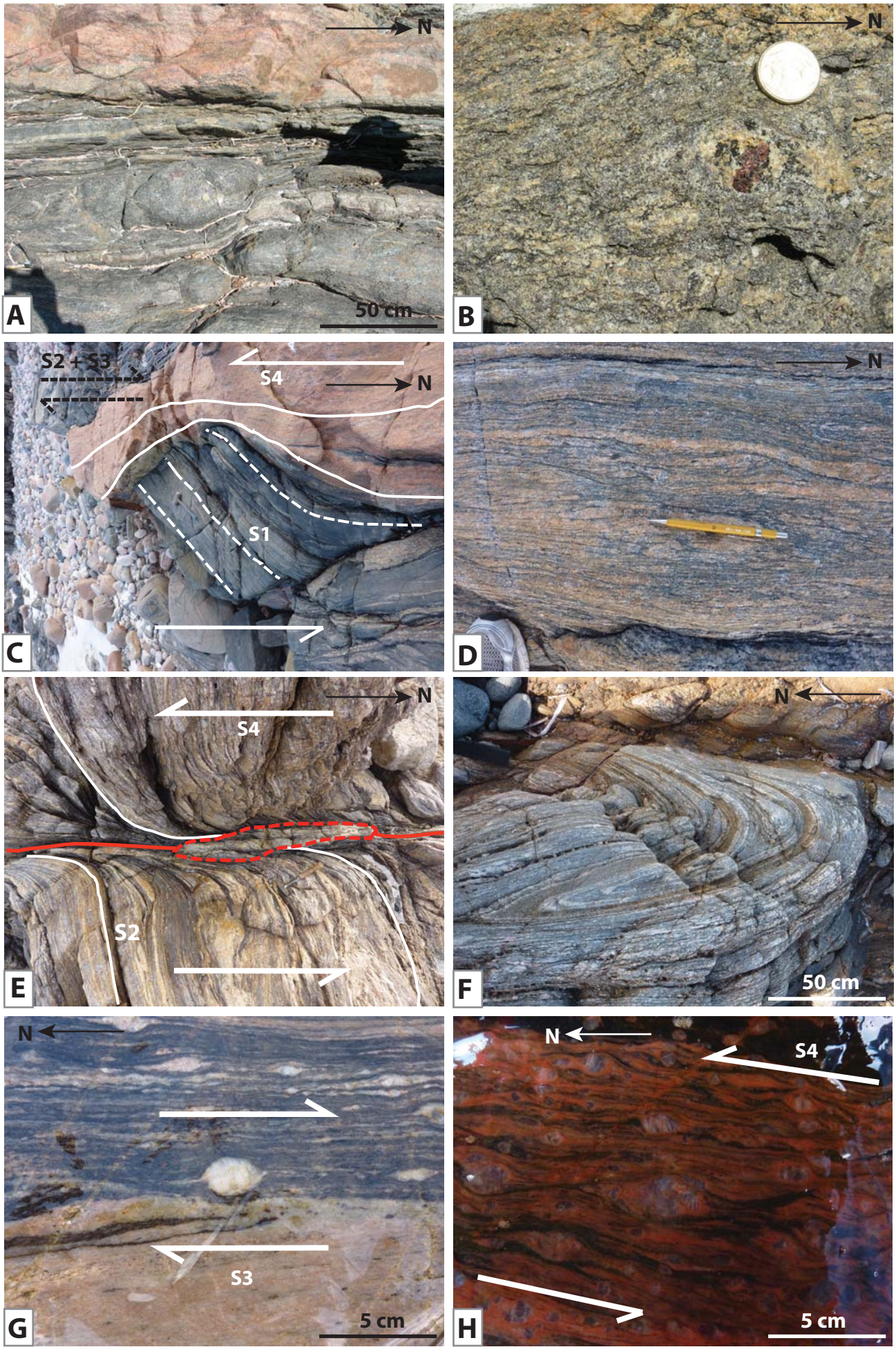

Figure 3 Carnot Gneiss

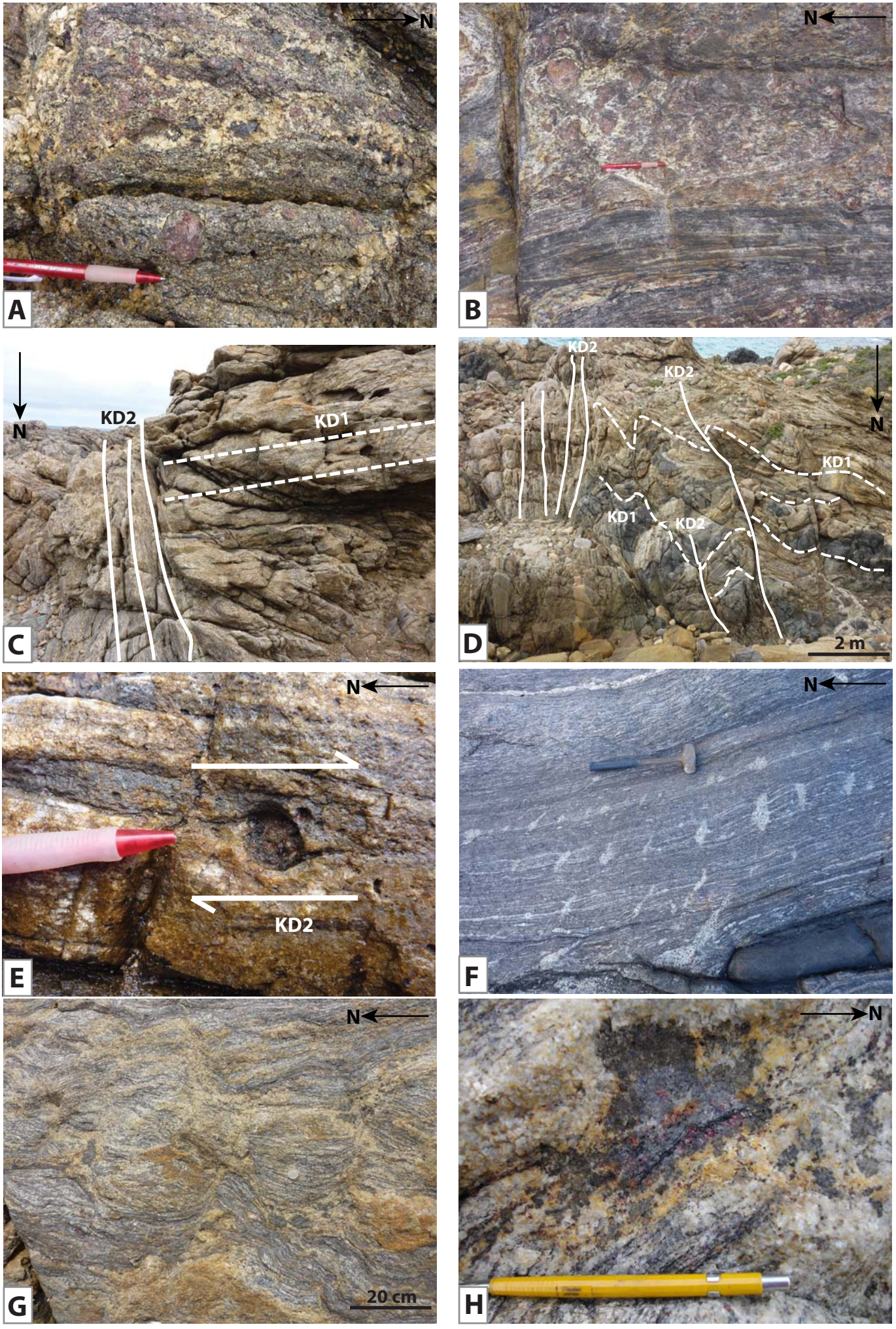

Figure 4 Bratten Cairn

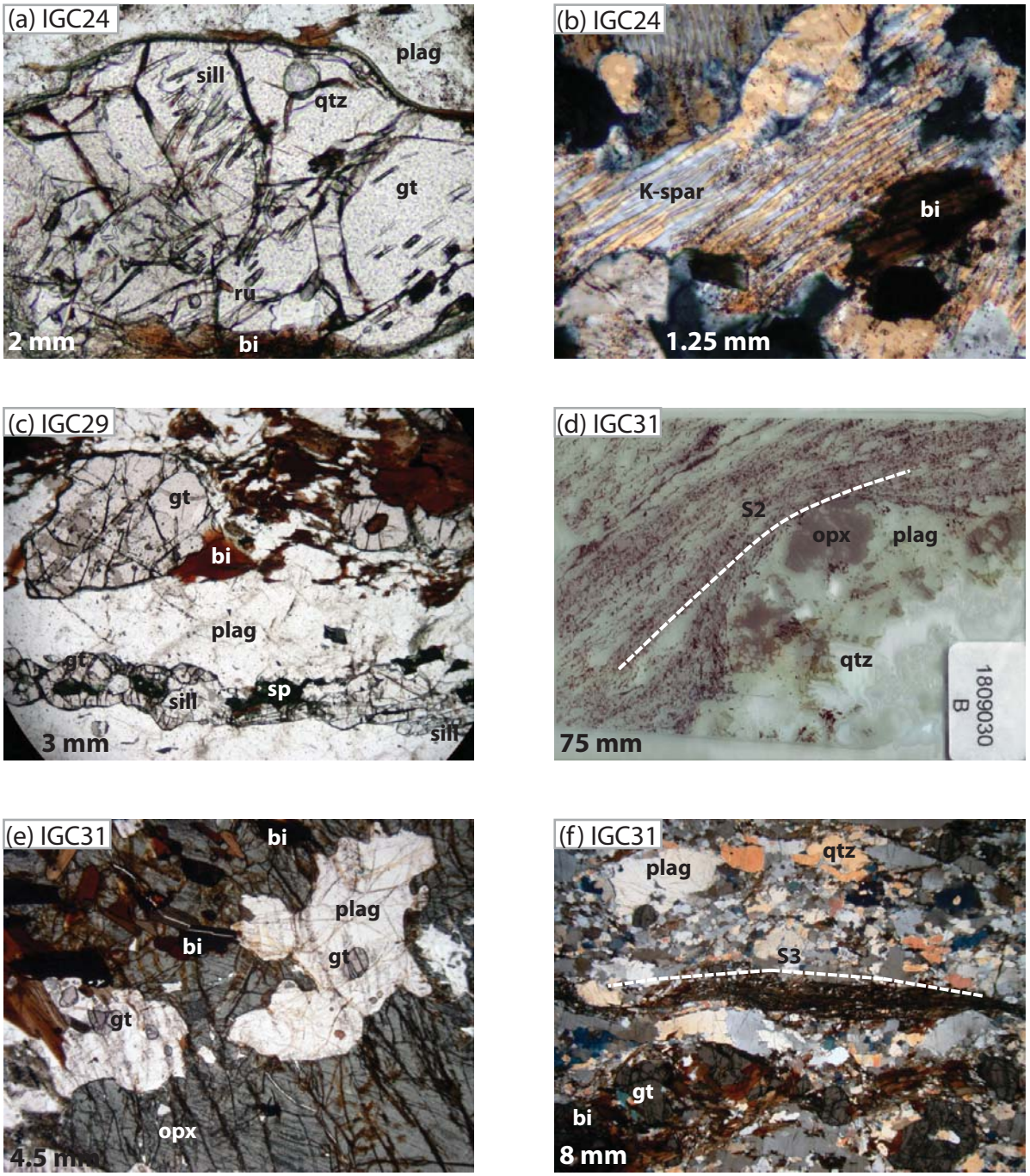

Figure 5 Bratten Cairn

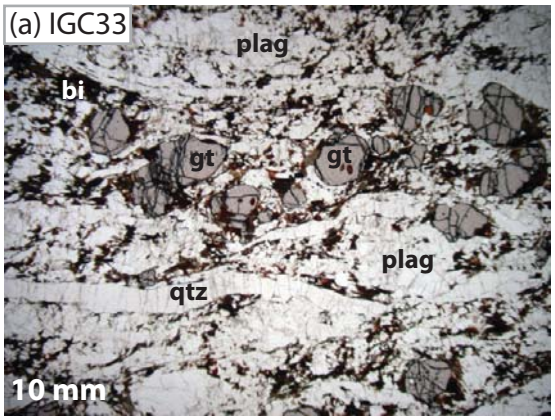

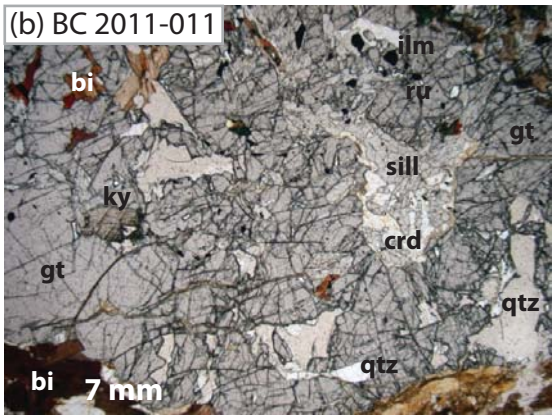

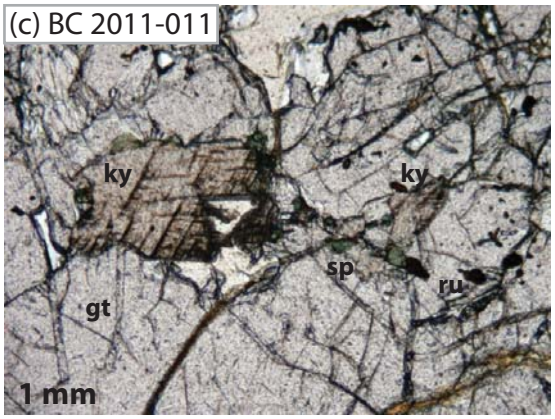

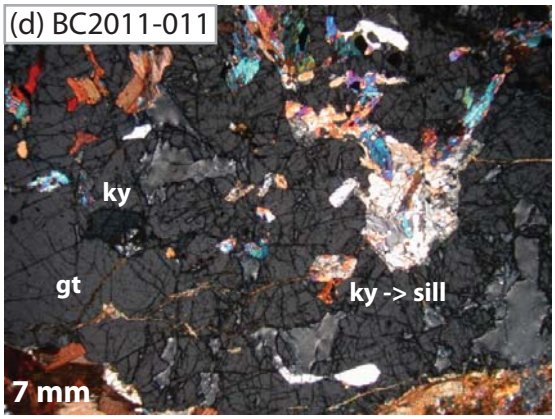

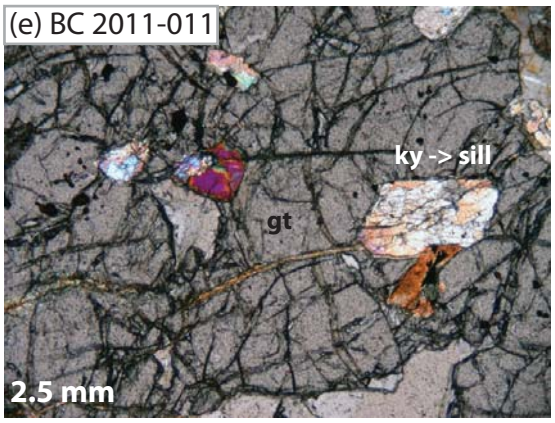

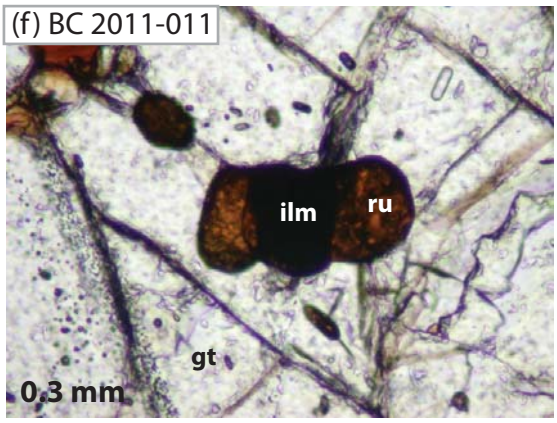

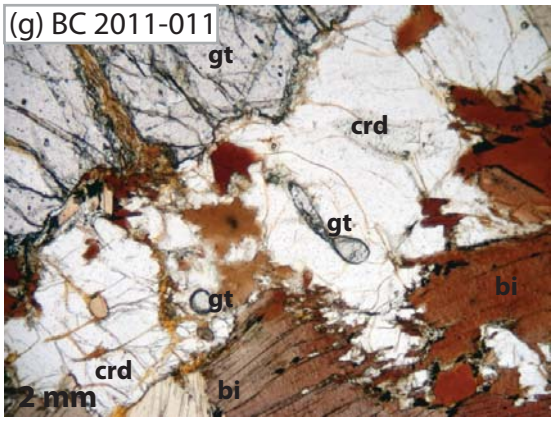

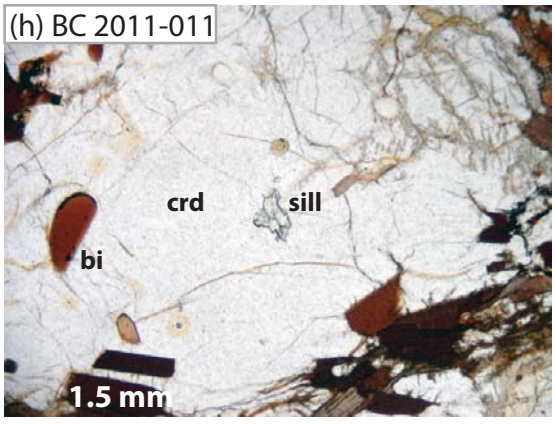

Figure 6 Carnot Gneiss

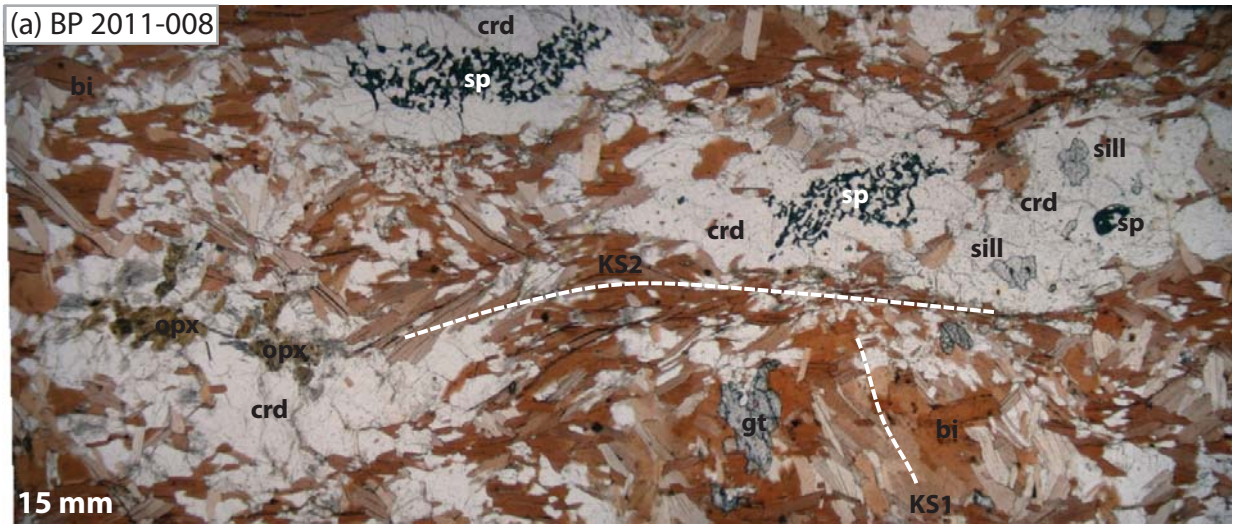

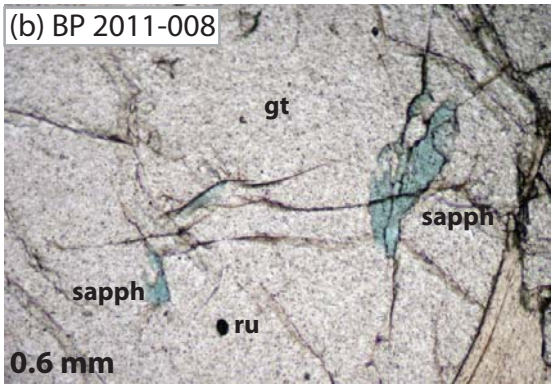

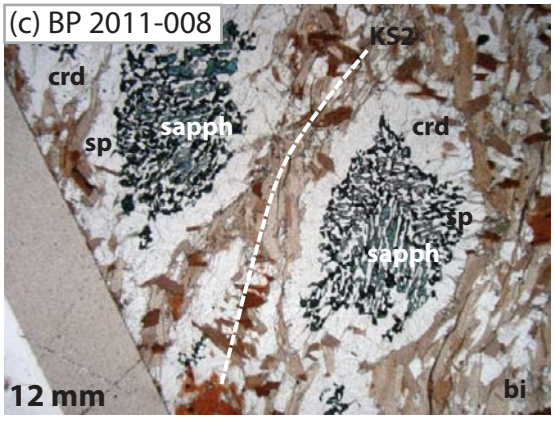

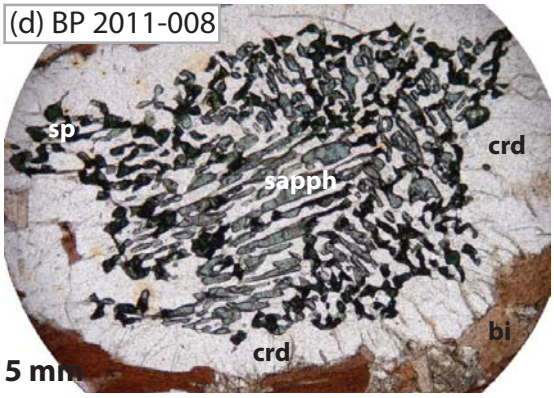

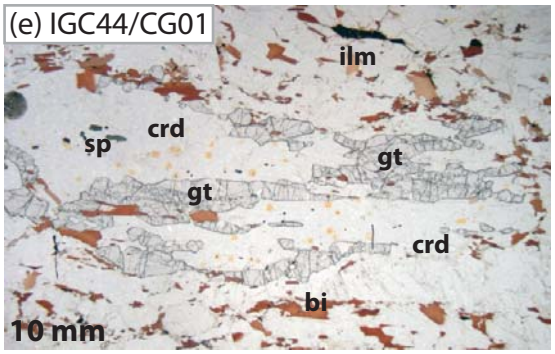

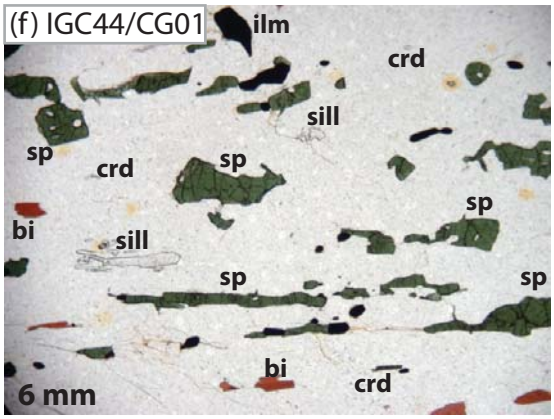

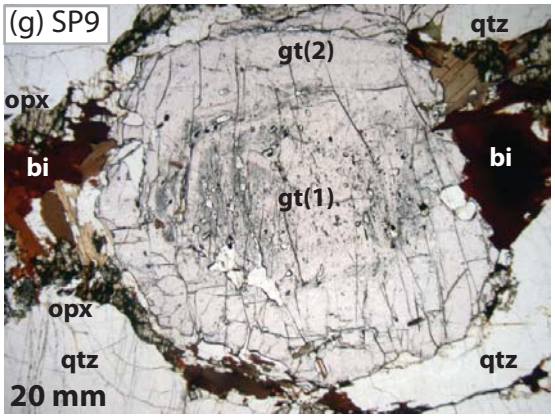

Figure 7

(a) Sample IGC31: Concordia plot of all zircon analyses

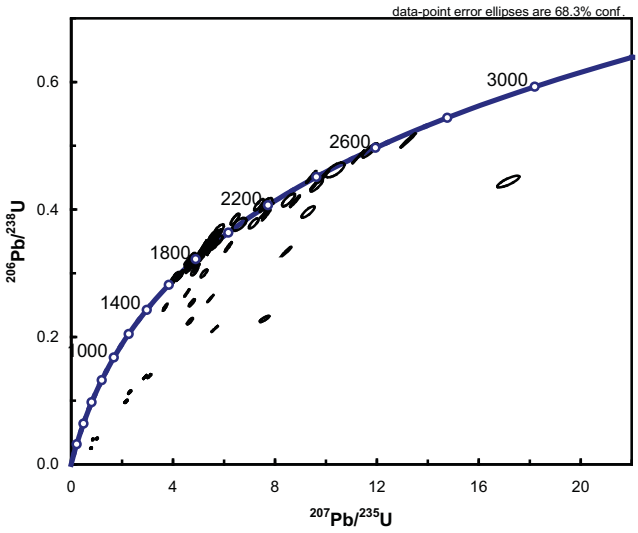

(b) Sample IGC31: Concordia plot of detrital zircon analyses, 90-110% conc.

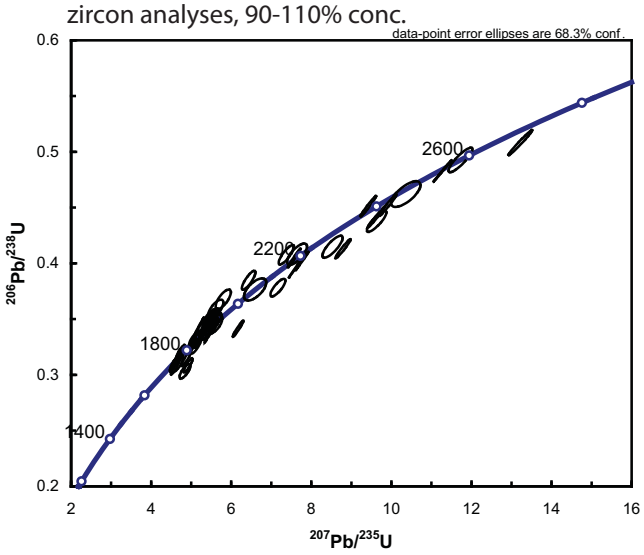

(c) Sample IGC31: Age spectra of detrital zircon grains, 90-110% concordancy (n=53/72)

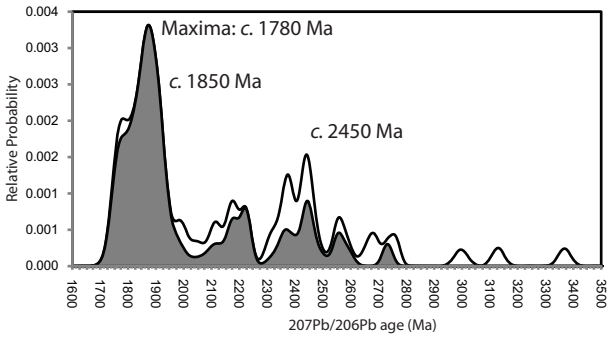

(d) Sample IGC31: (A-D) Zircon CL images with analysis spots

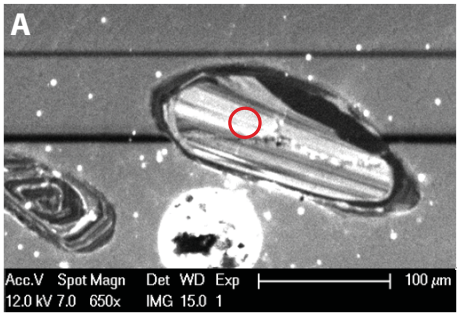

030-86:
1780 ± 20 Ma
99% conc.

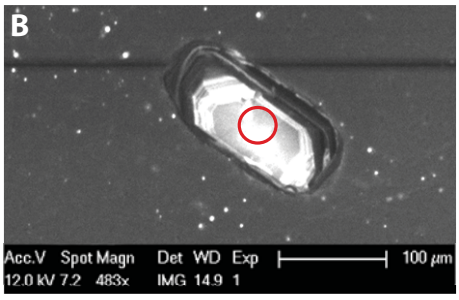

030-73:
1865 ± 19 Ma
99% conc.

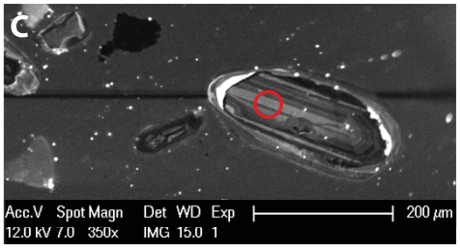

030-48 (0707):
2336 ± 29 Ma
96% conc.

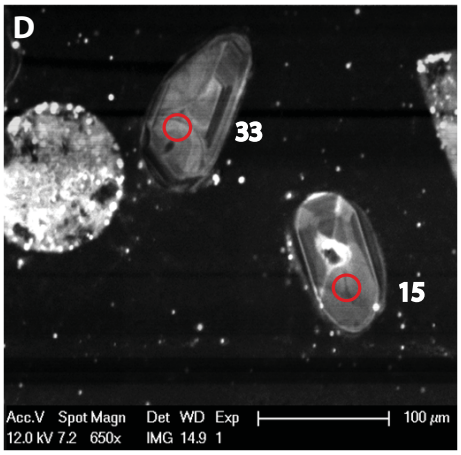

030-33:
1702 ± 26 Ma
99% conc.

303-15:
1883 ± 29 Ma
100% conc.

Figure 8

(a) Sample IGC33: Concordia plot of all zircon analyses

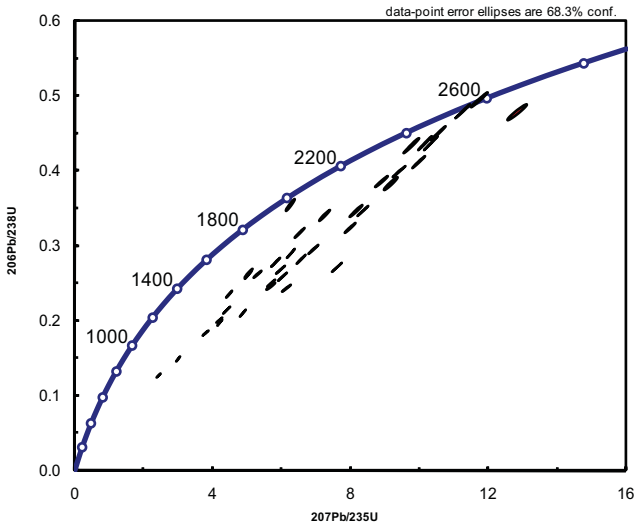

(b) Sample IGC33: Concordia plot of 90-110% concordant analyses

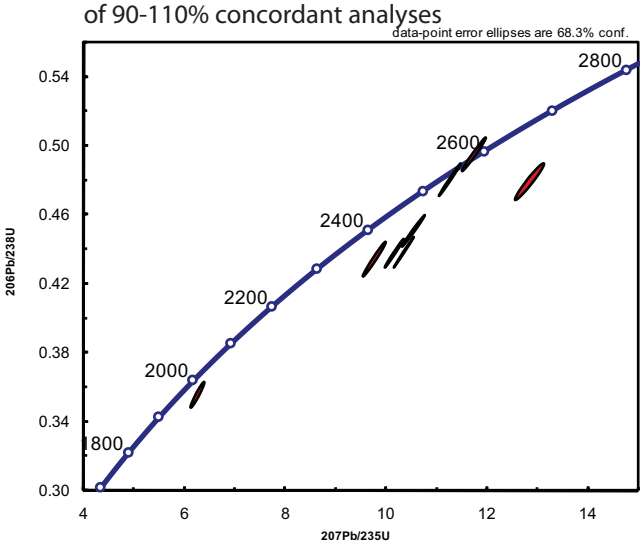

(c) Sample IGC33: Age spectra of detrital zircons, 90-110% concordancy (n=8/38)

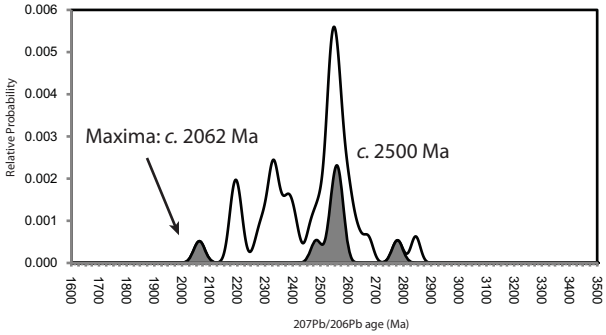

(d) Sample IGC33: (A-C) Zircon CL images with analysis spots

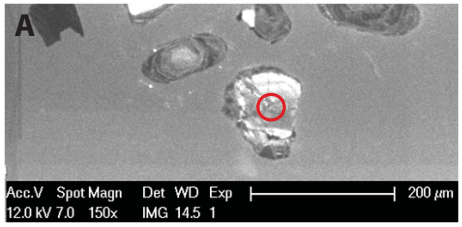

Zr: 033-26
2062 ± 23 Ma
95% conc.

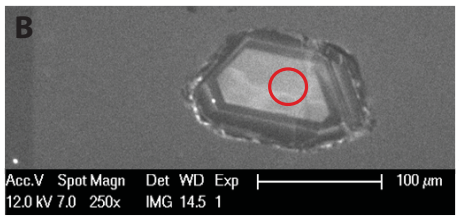

Zr: 033-05
2556 ± 17 Ma
99% conc.

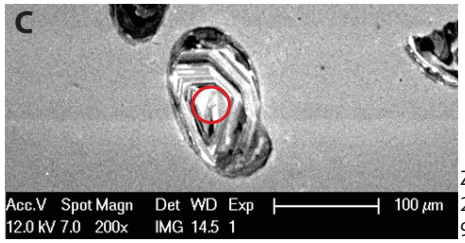

Zr: 033-26
2551 ± 18 Ma
94% conc.

Figure 9

(a) Sample IGC24: Concordia plot of 90-110% concordant analyses

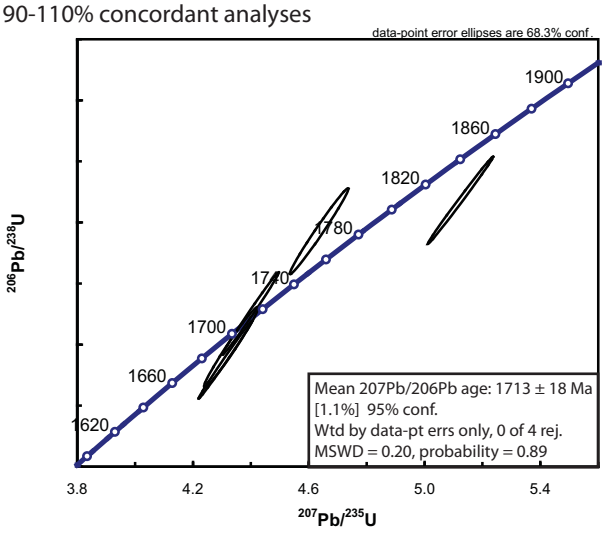

(b) Sample IGC24: Monazite backscatter electron images

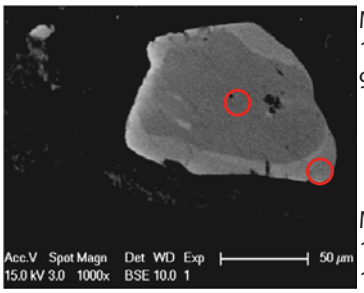

Mnz: 189core
1724 ± 19 Ma
98% conc.

Mnz: 189rim
1713 ± 18 Ma
101% conc.

(c) Sample IGC29: Concordia plot of 90-110% concordant analyses

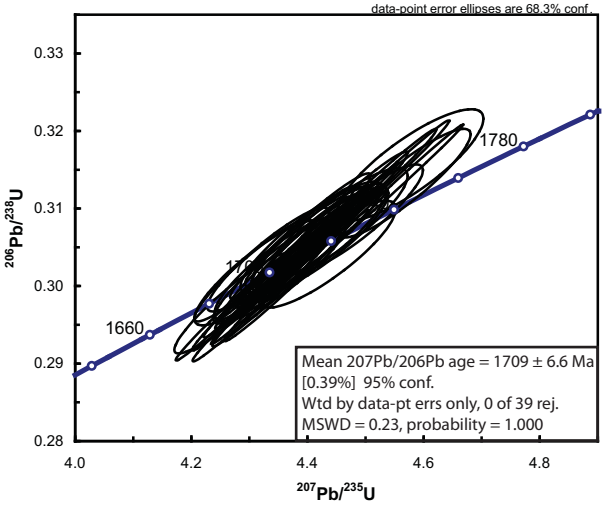

(d) Sample IGC29: (A-B) Monazite backscatter electron images

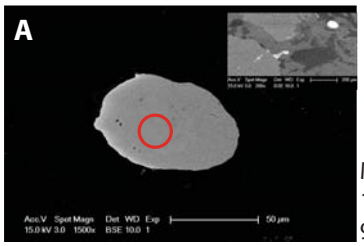

Mnz: 172
1697 ± 23 Ma
99% conc.

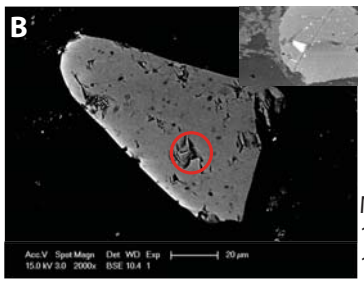

Mnz: B10
1696 ± 22 Ma
100% conc.

(e) Sample BC 2011-011: Concordia plot of 90-110% concordant analyses

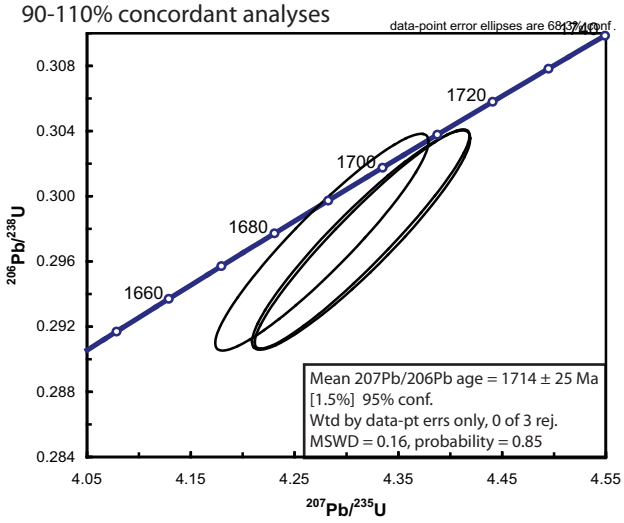

(f) Sample BC 2011-011: Monazite with analysis spots

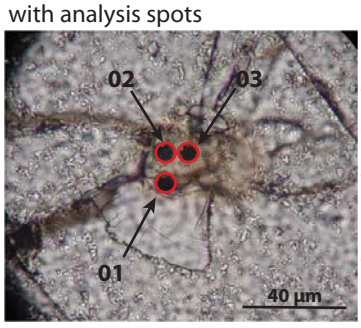

Mnz: 859-01
1704 ± 22 Ma
101% conc.

Mnz: 859-02
1719 ± 22 Ma
101% conc.

Mnz: 859-03
1719 ± 22 Ma
101% conc.

Figure 10

(a) Sample IGC44
Zircon concordia plot of all zircon analyses

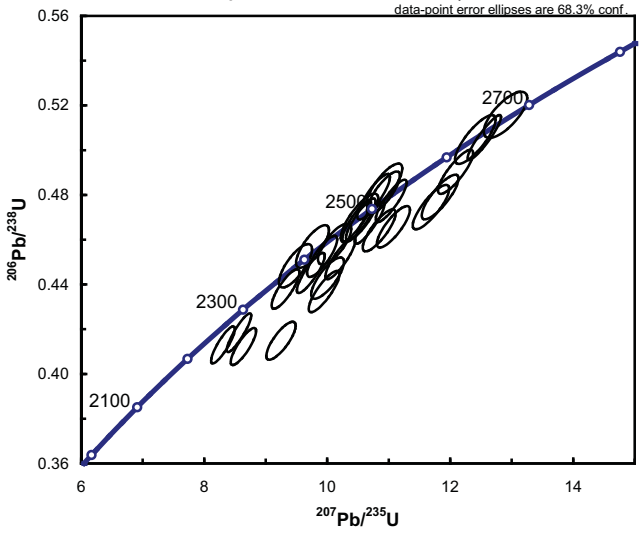

(b) Sample IGC44 (A-B): Zircon CL images with analysis spots

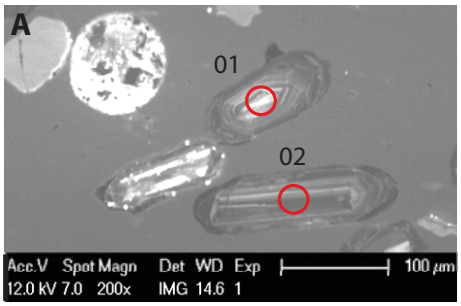

Zr: 044-01
2637 ± 25 Ma
100% conc.
Zr: 044-02
2646 ± 24 Ma
95% conc.

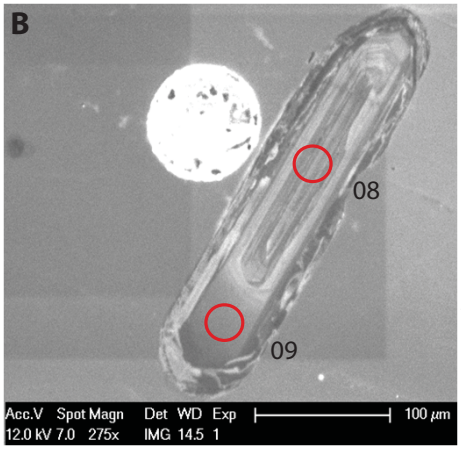

Zr: 044-08
2495 ± 27 Ma
102% conc.
Zr: 044-09
2385 ± 29 Ma
100% conc.

(c) IGC44: Age spectra of all zircon grains
90-110% concordancy (n=30/42)

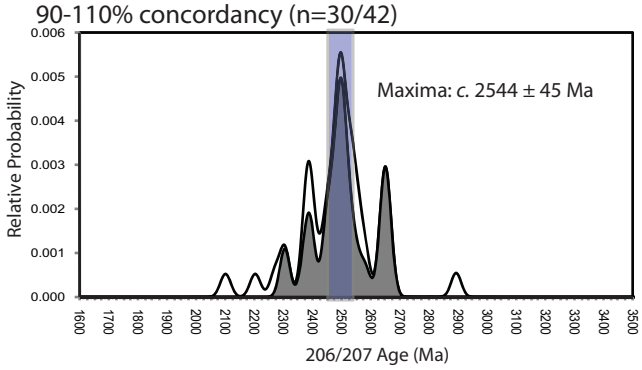

(d) Sample CG01: Monazite concordia
of 90-110% analyses

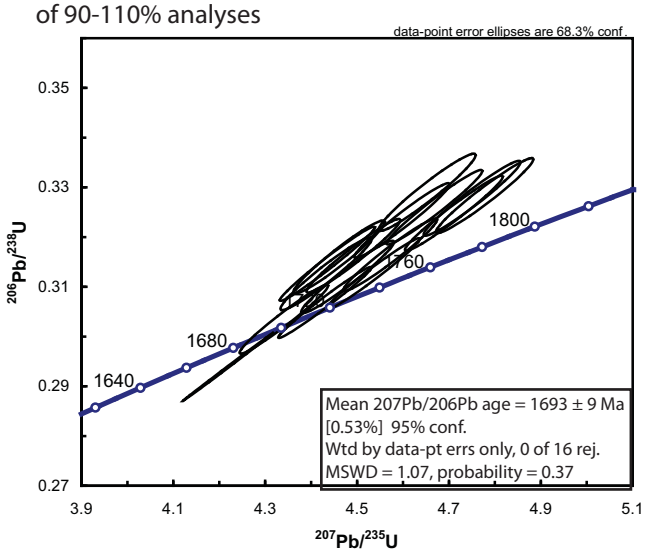

(e) Sample CG01 (A-B): Monazite CL
images with analysis spots

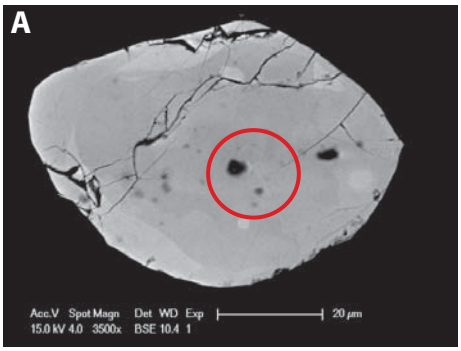

Mnz: CG01-4a
1742 ± 18 Ma
95% conc.

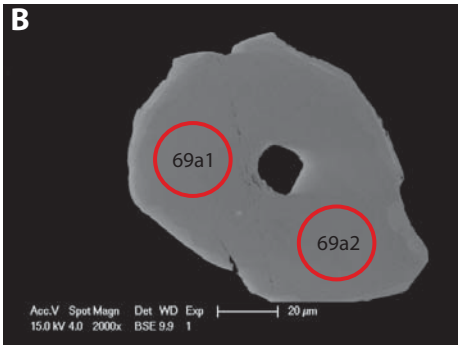

Mnz: CG01-69a1
1717 ± 18 Ma
98% conc.
Mnz: CG01-69a2
1681 ± 18 Ma
97% conc.

Figure 11

(a) Sample BP 2011-008: Concordia plot of all analyses

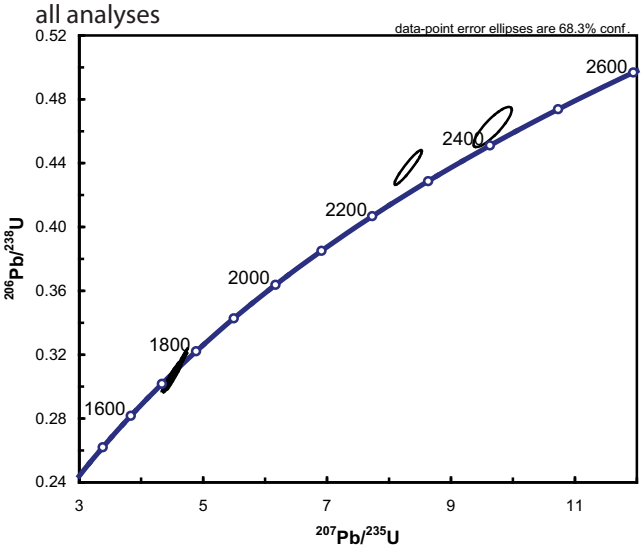

(b) Sample BP 2011-008: Concordia plot of younger population

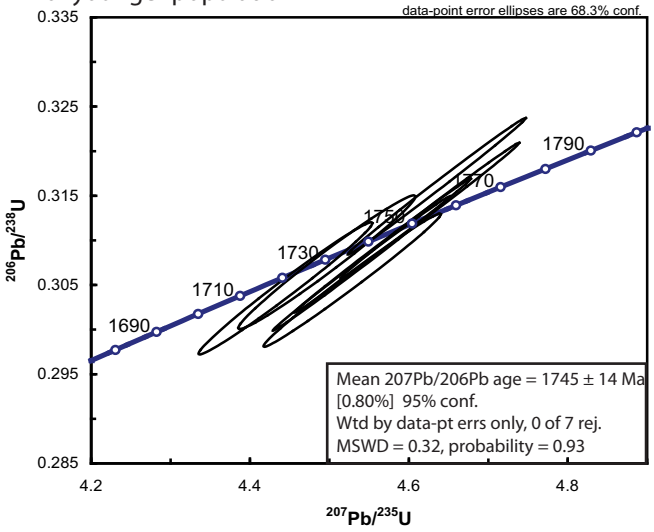

(c) Sample BP 2011-008 (A-C): Monazite with analysis spots

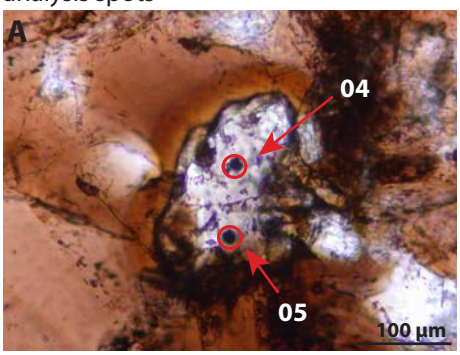

Mnz: 843-04
1752 ± 19 Ma
101% conc.
Mnz: 843-05
1739 ± 18 Ma
99% conc.

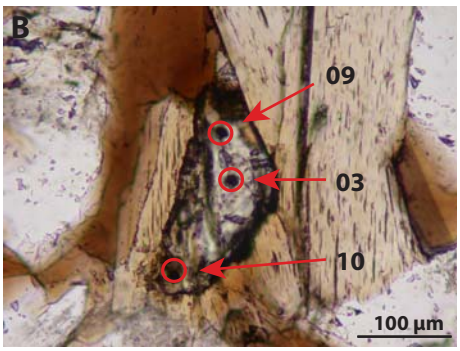

Mnz: 843-09
1752 ± 19 Ma
100% conc.
Mnz: 843-03
1751 ± 18 Ma
100% conc.
Mnz: 843-10
1746 ± 20 Ma
101% conc.

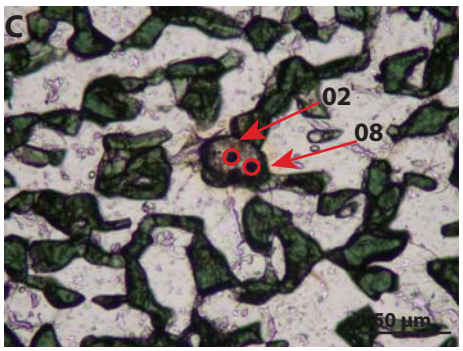

Mnz: 843-02
2201 ± 23 Ma
97% conc.
Mnz: 843-08
2365 ± 31 Ma
98% conc.

Figure 12

(a) Sample SP6: Concordia plot of 90-110% concordant analyses

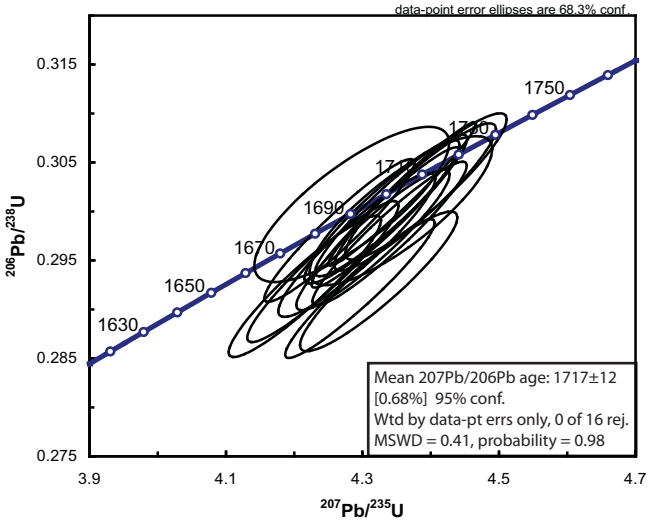

(b) Sample SP6: Thin section photomicrograph of in-situ monazite

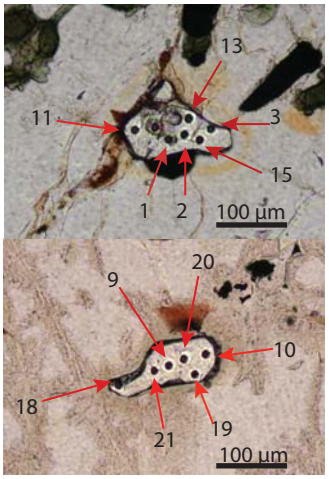

SP6-01 1715 ± 22 Ma
101% conc.
SP6-02 1711 ± 23 Ma
100% conc.
SP6-03 1721 ± 25 Ma
103% conc.
SP6-11 1721 ± 24 Ma
102% conc.
SP6-13 1728 ± 23 Ma
101% conc.
SP6-15 1744 ± 22 Ma
101% conc.
SP6-09 1721 ± 24 Ma
101% conc.
SP6-10 1711 ± 20 Ma
101% conc.
SP6-18 1710 ± 23 Ma
100% conc.
SP6-19 1694 ± 22 Ma
100 % conc
SP6-21 1709 ± 24 Ma
102% conc.

(c) Sample SP7: Concordia plot of 90-110% concordant analyses

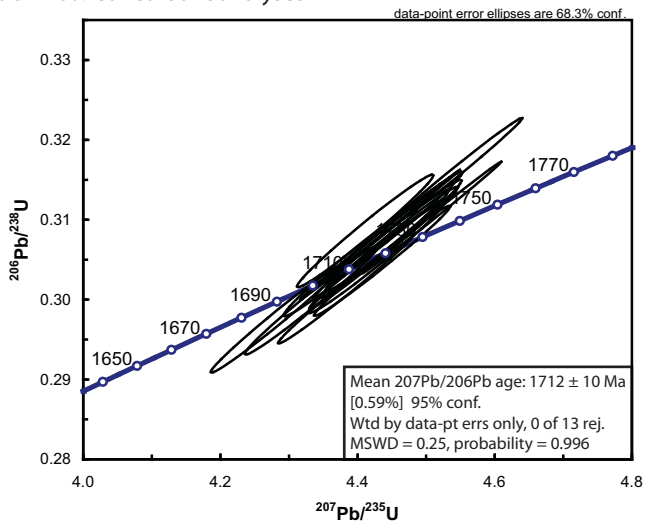

(d) Sample SP7 (A-B): Monazite backscatter electron images

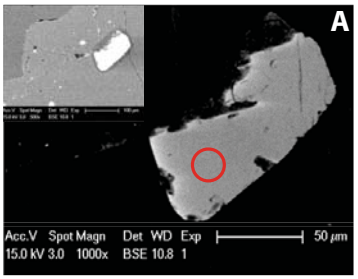

Mnz: 02
1715 ± 18 Ma
100% conc.

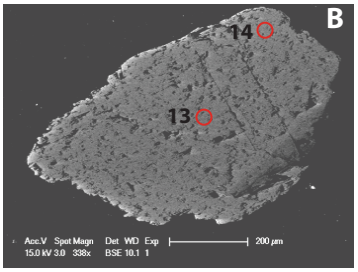

Mnz: 13
1712 ± 18 Ma
100% conc.

Mnz: 14
1711 ± 18 Ma
101% conc.

(e) Sample ASE-01: Concordia plot of 90-110% concordant analyses

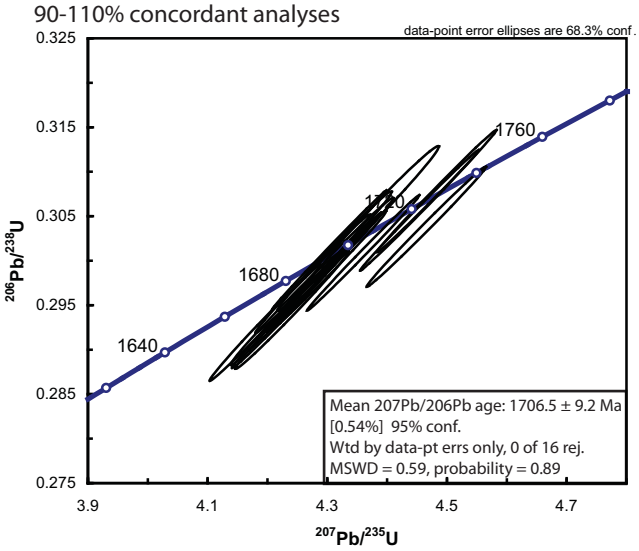

(f) Sample ASE-01: Monazite backscatter electron image

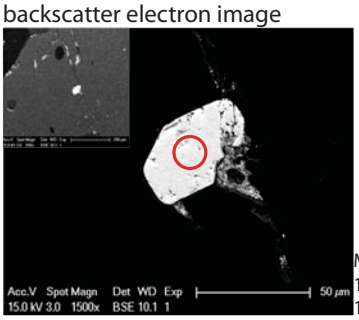

Mnz: 18
1700 ± 19 Ma
101% conc.

Figure 13

(a) Sample IGC24, Garnet A

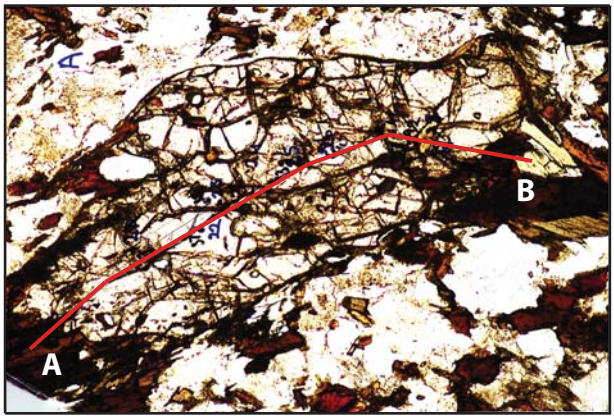

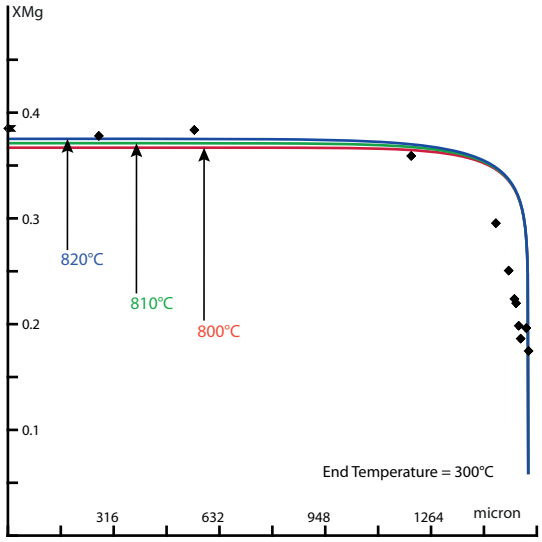

(b) Diffusion profile, Garnet A

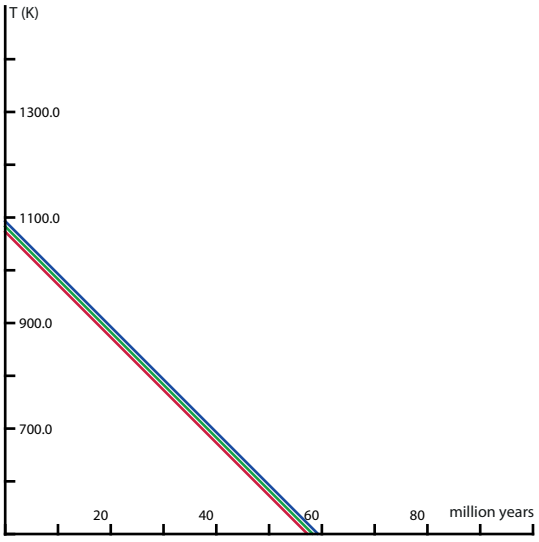

(c) Cooling rate, Garnet A

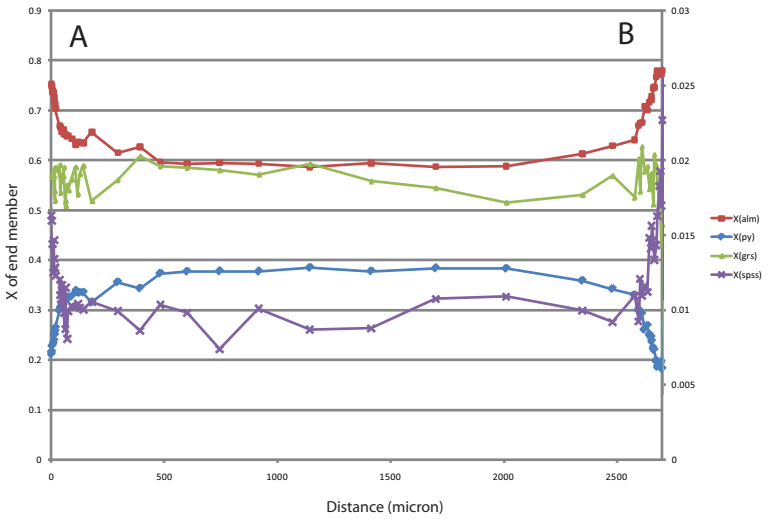

(d) Microprobe traverse, Garnet A

Figure 14

(a) Sample ASE-01 Garnet A

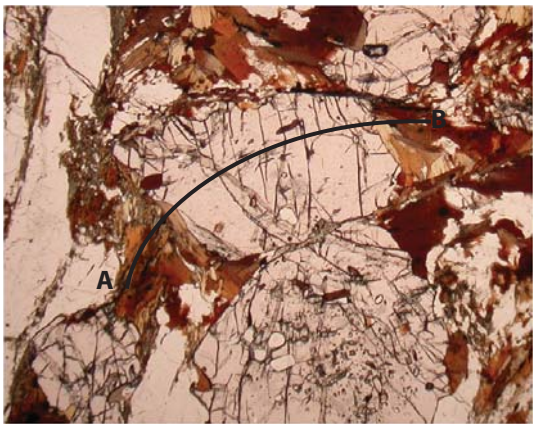

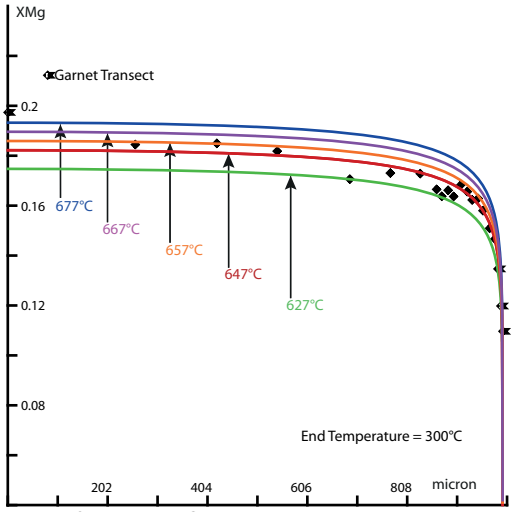

(b) Diffusion profile, Garnet A

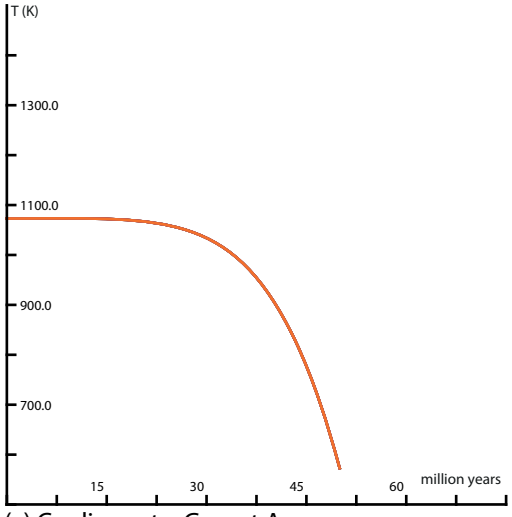

(c) Cooling rate, Garnet A

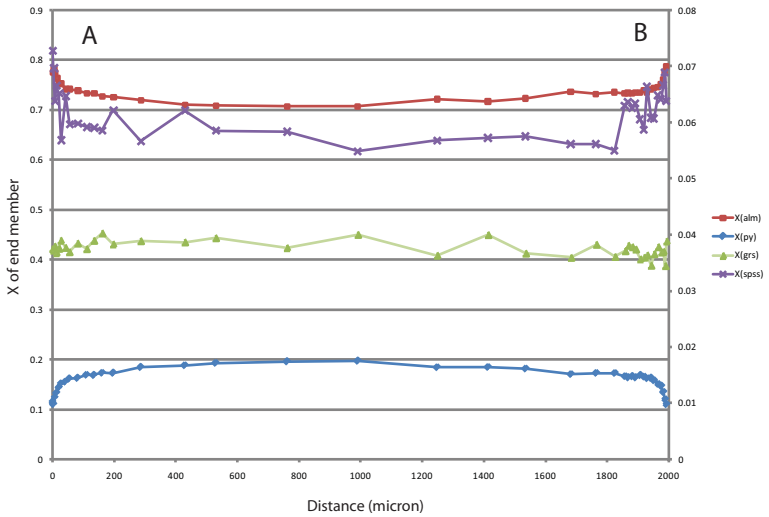

(d) Microprobe traverse, Garnet A

Figure 15

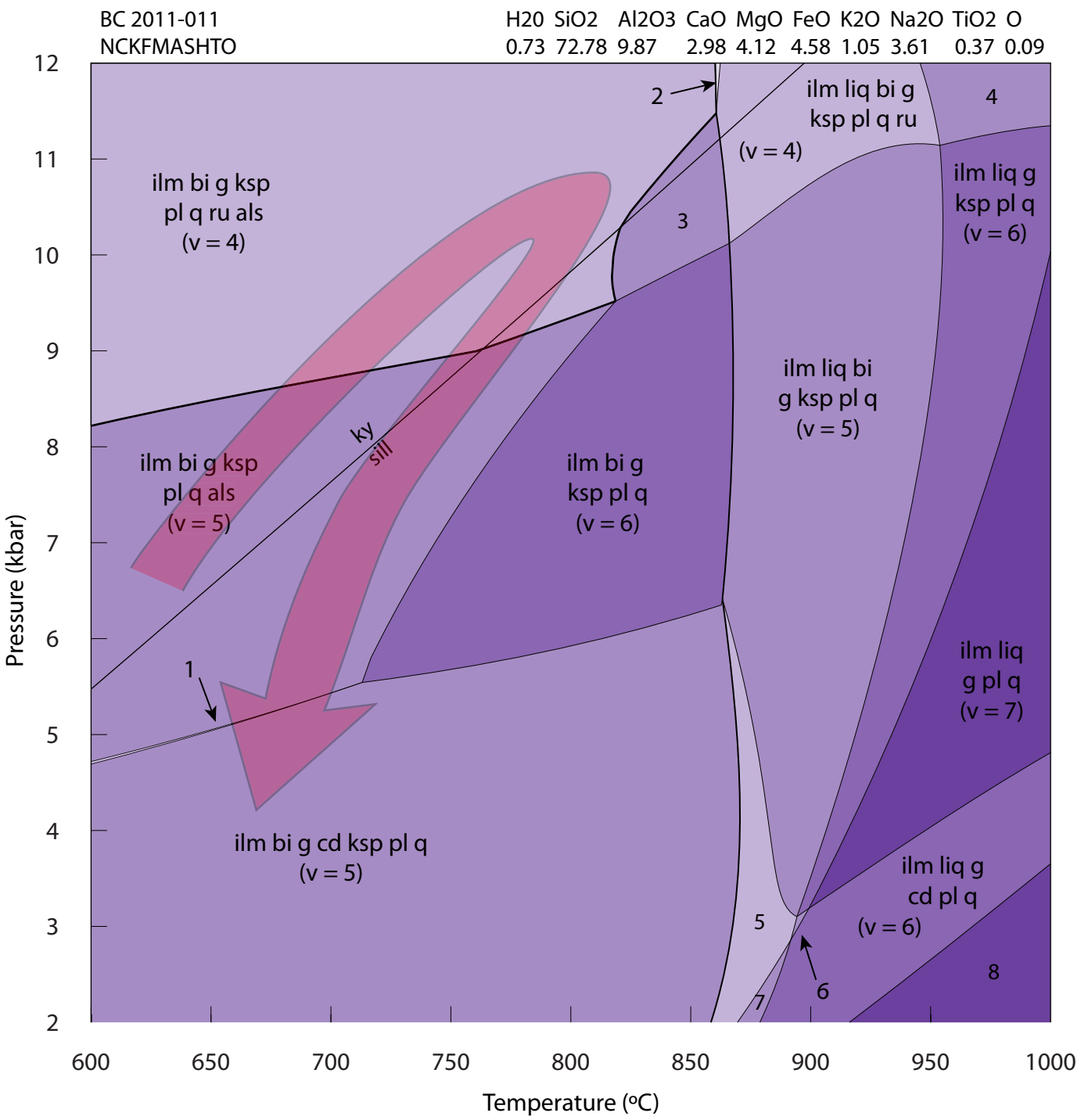

1. ilm bi g cd ksp pl q sill (v = 4)
2. ilm liq bi g ksp pl q ru ky (v = 3)
3. ilm liq bi g ksp pl q ru (v = 5)
4. ilm liq g ksp pl q ru (v = 5)
5. ilm liq bi g cd ksp pl q (v = 4)
6. ilm liq g cd ksp pl q (v = 5)
7. ilm liq bi g cd pl q (v = 5)
8. ilm liq cd pl q (v = 7)

Figure 16

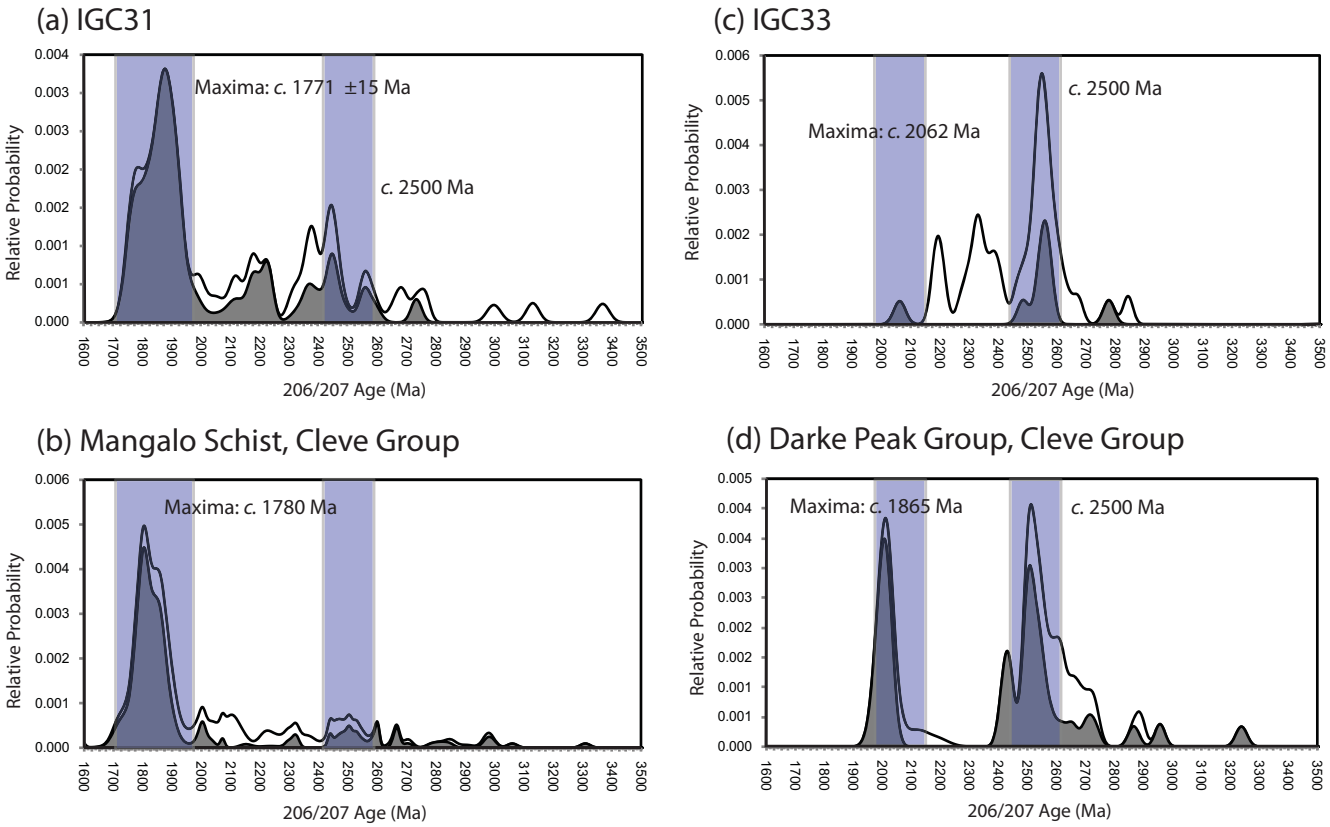
(a) IGC31
Maxima: c. 1771 ±15 Ma
c. 2500 Ma
(c) IGC33
Maxima: c. 2062 Ma
c. 2500 Ma
(b) Mangalo Schist, Cleve Group
Maxima: c. 1780 Ma
(d) Darke Peak Group, Cleve Group
Maxima: c. 1865 Ma
c. 2500 Ma
Relative Probability
206/207 Age (Ma)

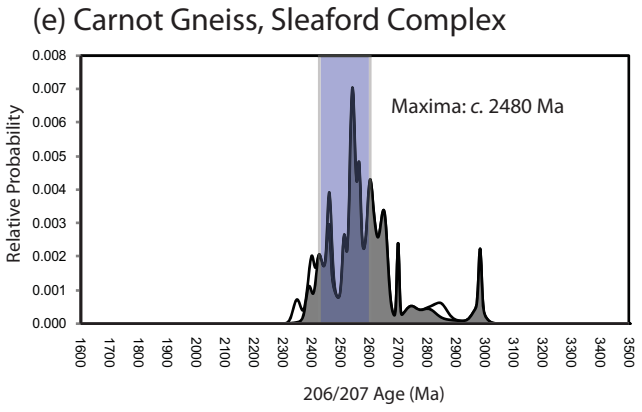
(e) Carnot Gneiss, Sleaford Complex
Maxima: c. 2480 Ma
Relative Probability
206/207 Age (Ma)

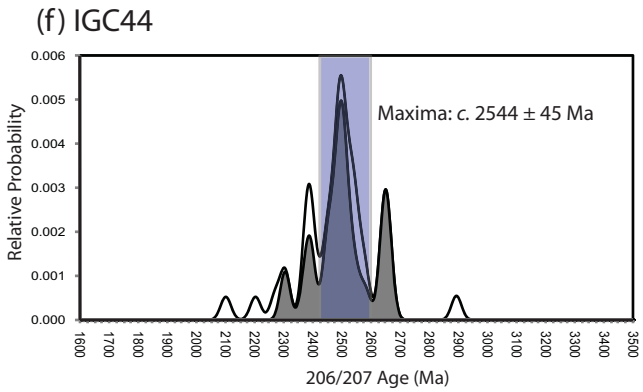
(f) IGC44
Maxima: c. 2544 ± 45 Ma
Relative Probability
206/207 Age (Ma)

Figure 17

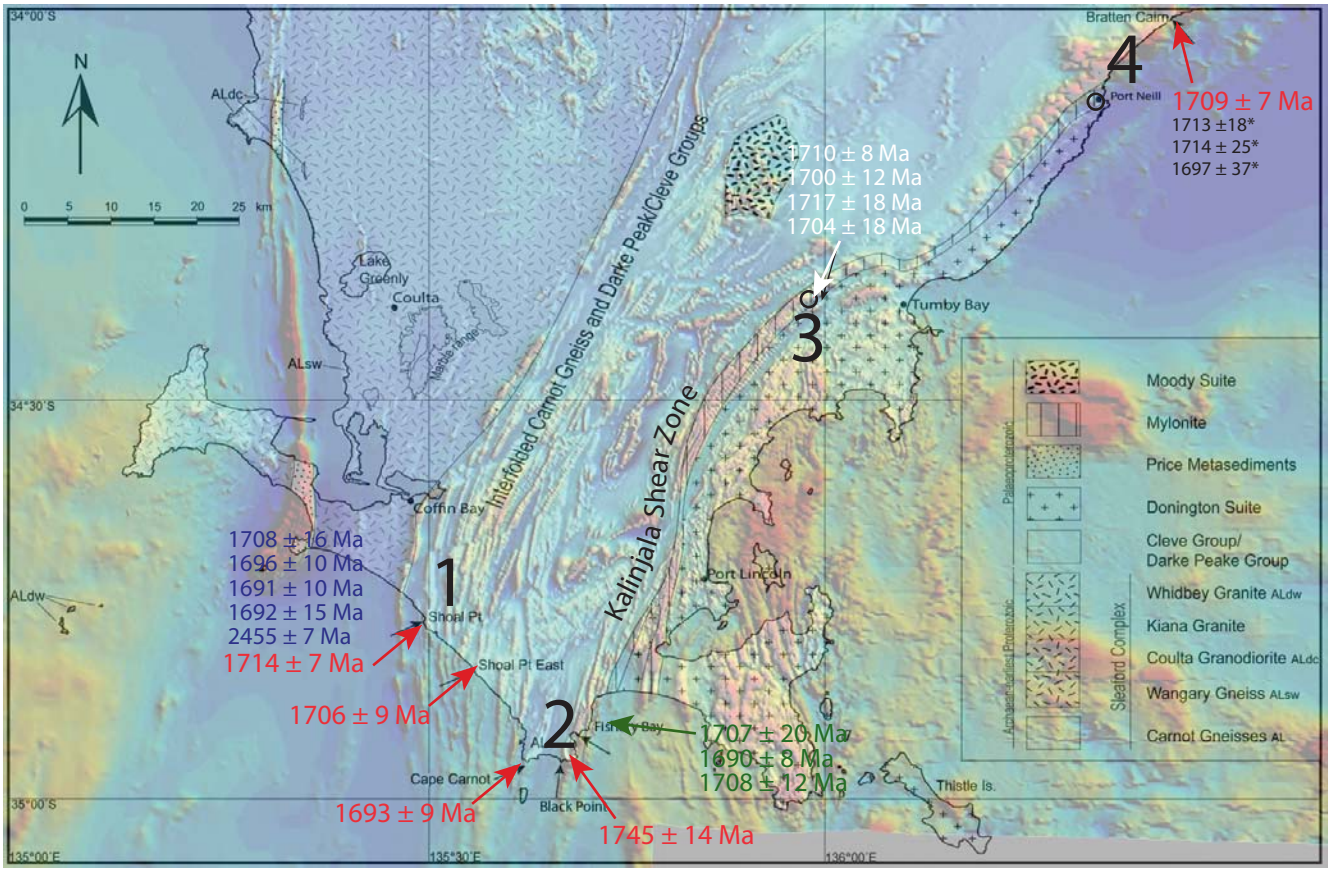

1. Shoal Point

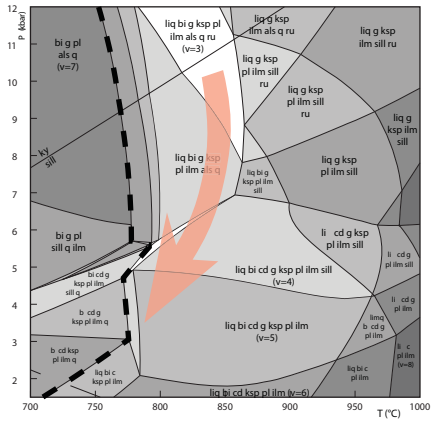

8-9 kbar at 820-850 ºC
Shoal Point East cooling
rate = ~ 10 °CMa-1 (this study)

2. Black Point

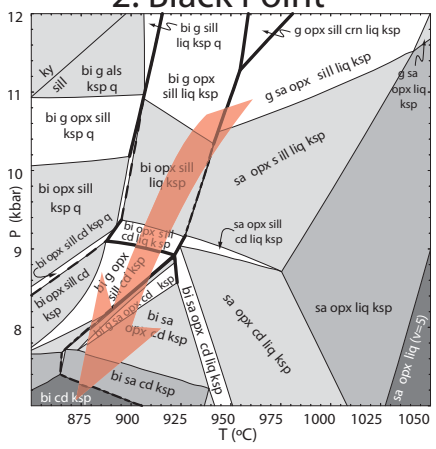

3. Mine Creek

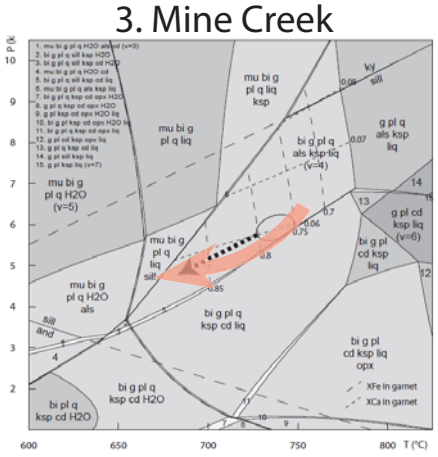

6-7 kbar at ~750 ºC
cooling rate = <10 °CMa-1
(Dutch 2009)

4. Bratten Cairn

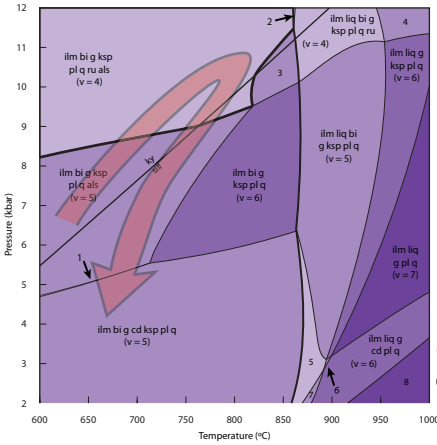

Peak: 9-10kbar, ~810 ºC
cooling rate = ~ 60 °CMa-1 (this study)
cooling rate = ~ 60 °CMa-1 (Dutch 2009, chapter 5)

Appendix 2 A
Zircon LA-ICPMS U-Pb Geochronology Analyses

IGC31	Isotope Ratios									Ages (Ma)								
Spot Name	Pb207/Pb206	± 1σ	Pb206/U238	± 1σ	Pb207/U235	± 1σ	Pb208/Th232	± 1σ	rho	Pb207/Pb206	± 1σ	Pb206/U238	± 1σ	Pb207/U235	± 1σ	Pb208/Th232	± 1σ	Conc. (%)
030-01	0.1726	0.00239	0.4927	0.00725	11.72362	0.197	0.12926	0.00459	0.875691	2583	22.94	2582.4	31.3	2582.6	15.72	2457	82.23	100
030-02	0.1726	0.00239	0.4927	0.00725	11.72362	0.197	0.12926	0.00459	0.846581	2583	22.94	2582.4	31.3	2582.6	15.72	2457	82.23	95
030-03	0.1596	0.00229	0.43777	0.0062	9.63341	0.16116	0.14619	0.00578	0.839267	2451.4	24.09	2340.7	27.79	2400.4	15.39	2757.9	101.96	106
030-04	0.12125	0.00179	0.38485	0.00562	6.4334	0.11194	0.10338	0.00429	0.785565	1974.7	26.02	2098.9	26.14	2036.8	15.29	1988.5	78.64	101
030-05	0.11672	0.00196	0.34753	0.00531	5.59125	0.10875	0.12845	0.00676	0.76586	1906.5	29.83	1922.8	25.41	1914.8	16.75	2442.6	121.16	100
030-06	0.11529	0.00209	0.33937	0.00531	5.3935	0.11019	0.09664	0.00484	0.872549	1884.4	32.31	1883.6	25.54	1883.8	17.5	1864.6	89.16	25
030-07	0.15795	0.00212	0.09891	0.00139	2.15387	0.03469	0.10011	0.0037	0.686334	2433.9	22.59	608	8.15	1166.3	11.17	1928.5	67.95	101
030-08	0.11206	0.00242	0.33195	0.00536	5.12742	0.12063	0.08524	0.00601	0.725783	1833	38.7	1847.8	25.94	1840.7	19.99	1653.4	111.91	108
030-09	0.11439	0.00222	0.36772	0.00578	5.79851	0.12558	0.10304	0.00651	0.700835	1870.2	34.64	2018.7	27.23	1946.2	18.76	1982.3	119.22	99
030-10	0.16259	0.00354	0.46213	0.00759	10.35852	0.24275	0.13192	0.00914	0.565324	2482.8	36.26	2449	33.46	2467.3	21.7	2504.6	163.27	102
030-20	0.10693	0.00324	0.31698	0.00559	4.67257	0.14576	0.09319	0.01021	0.628195	1747.8	54.4	1775	27.38	1762.3	26.09	1800.9	188.77	100
030-21	0.12705	0.00346	0.37665	0.00653	6.59645	0.18205	0.10437	0.00915	0.911287	2057.6	47.23	2060.6	30.6	2058.9	24.33	2006.5	167.5	34
030-22	0.16031	0.00197	0.13866	0.0019	3.06454	0.04608	0.11115	0.00324	0.834242	2459	20.62	837.1	10.77	1423.9	11.51	2130.2	58.94	101
030-23	0.16075	0.00293	0.11696	0.00169	2.59209	0.05102	0.10058	0.00588	0.905976	2463.5	30.5	713	9.76	1298.4	14.42	1937.1	107.97	30
030-24	0.11153	0.00172	0.3297	0.00492	5.06941	0.09068	0.2278	0.01167	0.837104	1824.5	27.65	1836.9	23.84	1831	15.17	4148	192.16	101
030-25	0.14685	0.00183	0.11347	0.00156	2.29721	0.03486	0.05923	0.00181	0.896578	2309.5	21.19	692.9	9.05	1211.4	10.73	1163	34.48	67
030-26	0.10666	0.00157	0.31512	0.00443	4.63386	0.07782	0.09318	0.00341	0.806654	1743.1	26.63	1765.8	21.73	1755.4	14.03	1800.6	63.02	100
030-27	~~0.13542~~	~~0.00174~~	~~0.25385~~	~~0.00353~~	~~4.73955~~	~~0.07351~~	~~0.06067~~	~~0.00195~~	0.791329	~~2169.5~~	~~22.21~~	~~1458.3~~	~~18.14~~	~~1774.3~~	~~13~~	~~1190.5~~	~~37.2~~	100
030-28	0.11224	0.00181	0.33105	0.00491	5.12276	0.09419	0.08712	0.00419	0.833936	1836.1	28.94	1843.5	23.78	1839.9	15.62	1688.3	77.83	104
030-29	0.11604	0.00189	0.34287	0.00495	5.48511	0.10007	0.10784	0.00546	0.82213	1896.1	28.96	1900.5	23.77	1898.3	15.67	2070	99.7	105
030-30	0.1312	0.00194	0.40771	0.00576	7.37443	0.12493	0.11858	0.00509	0.719759	2114.1	25.74	2204.5	26.36	2157.9	15.15	2264.9	91.94	101
030-31	0.11574	0.00173	0.36133	0.00503	5.7658	0.09763	0.10627	0.00482	0.893197	1891.5	26.62	1988.5	23.82	1941.3	14.65	2041.3	88.05	104
030-32	0.13581	0.0027	0.40826	0.00628	7.64381	0.16336	0.11769	0.00819	0.884752	2174.4	34.22	2207	28.76	2190	19.19	2248.9	148.02	101
030-33	0.1142	0.00147	0.35063	0.00485	5.52104	0.0855	0.0963	0.00306	0.844726	1867.2	23.05	1937.6	23.15	1903.9	13.31	1858.2	56.43	99
030-34	0.11436	0.00148	0.34231	0.00466	5.39818	0.08306	0.09815	0.00327	0.824115	1869.8	23.11	1897.8	22.39	1884.6	13.18	1892.5	60.16	98
030-35	0.1043	0.00149	0.29778	0.00417	4.28286	0.071	0.0881	0.00342	0.800116	1702.1	26.12	1680.3	20.7	1690.1	13.65	1706.6	63.62	94
030-35 0707	0.11383	0.00166	0.32578	0.00448	5.11371	0.08533	0.09834	0.00419	0.858548	1861.4	26.17	1817.9	21.81	1838.4	14.17	1895.9	77.13	100
030-36 0707	0.1374	0.00211	0.37823	0.0052	7.16588	0.12313	0.10064	0.00457	0.855549	2194.6	26.51	2068	24.34	2132.3	15.31	1938.1	83.92	98
030-37 0707	0.11134	0.00152	0.32616	0.00434	5.00688	0.0776	0.09158	0.00328	0.857692	1821.4	24.58	1819.7	21.07	1820.5	13.12	1771.2	60.78	102
030-38 0707	0.10381	0.00143	0.29461	0.00397	4.21697	0.06642	0.08066	0.00311	0.753307	1693.4	25.12	1664.5	19.76	1677.3	12.93	1567.9	58.11	105
030-39 0707	0.10719	0.00146	0.32022	0.00427	4.73273	0.07358	0.09296	0.00363	0.8341	1752.2	24.59	1790.8	20.83	1773.1	13.03	1796.6	67.14	102
030-40 0707	0.11278	0.00203	0.35077	0.00524	5.45469	0.10817	0.08408	0.00484	0.82271	1844.8	32.23	1938.3	25	1893.5	17.02	1631.8	90.16	70
030-41 0707	0.10755	0.00155	0.3198	0.00438	4.74234	0.07787	0.08053	0.00341	0.782051	1758.4	26.12	1788.7	21.38	1774.8	13.77	1565.5	63.87	104
030-42 0707	0.28038	0.00415	0.44392	0.00606	17.16101	0.28475	0.05564	0.00254	0.754653	3365	22.9	2368.2	27.07	2943.9	15.92	1094.4	48.57	104
030-43 0707	0.11244	0.00186	0.34509	0.00498	5.34933	0.09871	0.09244	0.00489	0.786008	1839.1	29.72	1911.1	23.85	1876.8	15.79	1786.9	90.4	103
030-44 0707	0.11382	0.00199	0.3506	0.00509	5.50163	0.10584	0.09303	0.00544	0.75325	1861.2	31.28	1937.5	24.32	1900.9	16.53	1798	100.67	105
030-45 0707	0.1135	0.00183	0.34493	0.00492	5.39756	0.09795	0.08775	0.00461	0.845471	1856.3	28.91	1910.4	23.59	1884.5	15.55	1700	85.72	56
030-46 0707	0.10592	0.00184	0.32472	0.00469	4.74171	0.09092	0.1158	0.007	0.869247	1730.3	31.62	1812.8	22.84	1774.6	16.08	2214.7	126.87	98
030-47 0707	0.15043	0.00218	0.22483	0.00312	4.66262	0.07653	0.10814	0.00454	0.84333	2350.8	24.56	1307.4	16.41	1760.6	13.72	2075.4	82.75	5
030-48 0707	0.10491	0.00143	0.29776	0.0041	4.30663	0.06822	0.1718	0.00863	0.805191	1712.7	24.9	1680.2	20.37	1694.6	13.05	3204.5	148.94	96
030-49 0707	0.22182	0.00339	0.02549	0.00038	0.77953	0.01378	0.27622	0.01278	0.849663	2994	24.36	162.2	2.38	585.2	7.86	4929.8	202.44	99
030-50 0707	0.14912	0.00258	0.41492	0.0065	8.52957	0.16595	0.11208	0.00561	0.828642	2335.9	29.33	2237.4	29.61	2289.1	17.68	2147.2	101.95	84
030-51 0707	0.11027	0.00161	0.31982	0.00463	4.86196	0.08284	0.09186	0.00392	0.810051	1803.8	26.34	1788.8	22.63	1795.7	14.35	1776.4	72.54	103
030-52 0707	0.17025	0.00266	0.39624	0.00591	9.30133	0.16742	0.12038	0.00566	0.813351	2560.1	25.87	2151.7	27.28	2368.2	16.5	2297.5	102.04	83
030-53 0707	0.10563	0.00162	0.31865	0.00443	4.64038	0.07964	0.11173	0.00707	0.712586	1725.3	27.96	1783.1	21.66	1756.6	14.34	2140.7	128.48	98
030-54 0707	0.12605	0.00188	0.29978	0.00403	5.2099	0.08611	0.07146	0.00316	0.864258	2043.7	26.17	1690.2	19.97	1854.2	14.08	1395.1	59.65	10
030-55 0707	0.10847	0.00235	0.30982	0.00513	4.6328	0.10765	0.54704	0.04151	0.856685	1773.8	39.13	1739.8	25.23	1755.2	19.41	8819.4	542.32	42
030-56	0.18068	0.00249	0.04062	0.00056	1.01181	0.01614	0.19431	0.00756	0.996632	2659.1	22.63	256.7	3.46	709.8	8.15	3589.1	127.86	35
030-57	0.24103	0.00336	0.22839	0.00315	7.58968	0.12219	0.20255	0.0081	0.928739	3126.8	22	1326.1	16.53	2183.6	14.44	3728	136.15	97

Appendix 2 A
Zircon LA-ICPMS U-Pb Geochronology Analyses

030-58	0.15306	0.00155	0.1372	0.00182	2.89472	0.03827	0.11047	0.0012	0.973259	2380.3	17.18	828.8	10.31	1380.5	9.98	2117.9	21.91	69
030-59	0.10878	0.00132	0.30644	0.00398	4.59369	0.06424	0.43222	0.02168	0.996219	1779	21.93	1723.2	19.64	1748.1	11.66	7260.8	305.97	45
030-60	0.18347	0.00207	0.3339	0.00471	8.44511	0.1224	2.52188	0.04337	0.977584	2684.5	18.55	1857.3	22.78	2280	13.16	******	248.91	77
030-61	0.19218	0.00195	0.21268	0.00287	5.63398	0.07574	0.1636	0.00171	0.971346	2760.9	16.57	1243.1	15.24	1921.3	11.59	3062.5	29.67	93
030-62	0.12247	0.00133	0.26886	0.00361	4.53879	0.06234	0.34842	0.00549	0.998137	1992.5	19.13	1535	18.34	1738.1	11.43	6042.1	82.32	98
030-63	0.1544	0.00172	0.41294	0.00568	8.78765	0.12444	0.1345	0.0016	0.998871	2395.2	18.87	2228.4	25.9	2316.2	12.91	2550.6	28.45	97
030-64	0.1402	0.00141	0.4019	0.00542	7.7655	0.10453	0.13021	0.00143	0.925357	2229.7	17.29	2177.8	24.9	2204.2	12.11	2474	25.6	80
030-65	0.13934	0.0014	0.39566	0.00541	7.59999	0.1038	0.12722	0.00131	0.999357	2219	17.34	2149	24.97	2184.9	12.25	2420.5	23.41	10
030-66	0.10851	0.00136	0.24658	0.00357	3.6885	0.05771	0.1946	0.00686	0.967807	1774.4	22.74	1420.8	18.46	1568.9	12.5	3594	116.09	90
030-67	0.15724	0.00165	0.03918	0.00053	0.8492	0.01148	0.11155	0.00123	0.988667	2426.2	17.69	247.7	3.26	624.2	6.3	2137.6	22.42	101
030-68	0.13109	0.00146	0.3413	0.00471	6.16794	0.08795	0.1114	0.00133	0.951617	2112.6	19.43	1892.9	22.65	1999.9	12.46	2134.8	24.13	101
030-69	0.13571	0.00143	0.40484	0.00544	7.57315	0.10293	0.12149	0.00138	0.98348	2173.1	18.2	2191.3	24.96	2181.7	12.19	2317.5	24.83	94
030-70	0.10807	0.00125	0.31787	0.00439	4.7358	0.06873	0.15423	0.00441	0.998883	1767.1	20.99	1779.3	21.48	1773.6	12.17	2899.1	77.24	99
030-71	0.142	0.00153	0.39102	0.00532	7.65362	0.10588	0.14344	0.00195	0.990222	2251.7	18.48	2127.6	24.63	2191.2	12.42	2709.2	34.47	97
030-72	0.16941	0.00171	0.4827	0.00639	11.27181	0.14905	0.13694	0.00142	0.999382	2551.8	16.83	2539	27.8	2545.9	12.33	2594	25.28	101
030-73	0.15816	0.00169	0.44175	0.00621	9.62981	0.13671	0.1283	0.00158	0.97901	2436	18	2358.5	27.76	2400	13.06	2439.9	28.37	99
030-74	0.11092	0.00113	0.32837	0.00445	5.02089	0.068	0.10436	0.00118	0.945588	1814.5	18.38	1830.5	21.57	1822.9	11.47	2006.3	21.54	99
030-75	0.11403	0.00122	0.33108	0.00444	5.20434	0.07129	0.10111	0.00113	0.984706	1864.6	19.21	1843.6	21.51	1853.3	11.67	1946.8	20.7	97
030-76	0.10756	0.00126	0.31013	0.00424	4.59802	0.06648	0.17305	0.00867	0.981978	1758.4	21.18	1741.3	20.87	1748.9	12.06	3226	149.37	102
030-77	0.18862	0.00211	0.50834	0.0074	13.22102	0.19545	0.14169	0.00184	0.923238	2730.2	18.3	2649.5	31.63	2695.6	13.95	2678.4	32.5	96
030-78	0.11581	0.00123	0.34858	0.00471	5.5647	0.07657	0.10103	0.00121	0.980036	1892.5	19.05	1927.8	22.52	1910.7	11.84	1945.3	22.22	98
030-79	0.11238	0.00145	0.31505	0.00463	4.8819	0.07771	0.65931	0.02501	0.887791	1838.3	23.16	1765.5	22.69	1799.1	13.41	******	304.68	92
030-80	0.15901	0.00173	0.4521	0.00627	9.90805	0.14021	0.13676	0.00165	0.981516	2445.1	18.29	2404.6	27.84	2426.3	13.05	2590.8	29.32	102
030-81	0.1157	0.00154	0.30845	0.00416	4.91923	0.07473	0.27554	0.00864	0.979993	1890.8	23.75	1733.1	20.5	1805.6	12.82	4919	136.94	99
030-82	0.15148	0.0016	0.45124	0.00598	9.42235	0.12722	0.1312	0.00148	0.996233	2362.7	17.95	2400.7	26.55	2380	12.39	2491.7	26.44	106
030-83	0.11726	0.00126	0.34317	0.00475	5.54654	0.07834	0.10562	0.0012	0.944585	1914.9	19.19	1901.9	22.82	1907.8	12.15	2029.4	21.92	101
030-84	0.10979	0.00115	0.34398	0.00482	5.20496	0.07321	0.09649	0.00117	0.987303	1795.9	18.9	1905.8	23.1	1853.4	11.98	1861.8	21.66	63
030-85	0.10709	0.00128	0.31644	0.00447	4.67013	0.06984	0.1486	0.00676	0.996715	1750.5	21.58	1772.3	21.89	1761.9	12.51	2800.3	119	97
030-86	0.15232	0.00163	0.26027	0.00357	5.46609	0.07594	0.10465	0.00122	0.967498	2372.1	18.09	1491.2	18.24	1895.3	11.92	2011.6	22.4	99
303-11	0.11769	0.0012	0.33613	0.00468	5.45057	0.07564	0.09851	0.00105	0.642134	1921.4	18.22	1868	22.56	1892.8	11.91	1899.1	19.24	100
303-12	0.10883	0.00119	0.31459	0.00421	4.72019	0.06529	0.09729	0.00133	0.752075	1779.9	19.85	1763.2	20.63	1770.8	11.59	1876.6	24.54	100
303-13	0.11649	0.0023	0.35064	0.00553	5.6309	0.12347	0.09445	0.0061	0.713161	1903	35.12	1937.7	26.41	1920.8	18.91	1824.2	112.75	101
303-14	0.11698	0.0028	0.34487	0.00567	5.5621	0.14241	0.09683	0.00841	0.733068	1910.5	42.34	1910	27.2	1910.3	22.04	1868.2	154.96	100
303-15	0.10036	0.00183	0.28835	0.00446	3.98907	0.08204	0.12914	0.00775	0.79449	1630.7	33.44	1633.3	22.34	1632	16.7	2455	138.65	100
303-16	0.10142	0.00204	0.29501	0.00466	4.12427	0.09135	0.13652	0.00922	0.765183	1650.3	36.76	1666.5	23.2	1659.1	18.1	2586.6	163.97	90
303-17	0.11064	0.00218	0.32254	0.0051	4.91896	0.1061	0.10796	0.0067	0.750729	1809.9	35.33	1802.1	24.85	1805.5	18.2	2072.2	122.23	100
303-18	0.11522	0.00187	0.33924	0.00495	5.38882	0.09897	0.09762	0.00492	0.693275	1883.3	28.89	1883	23.83	1883.1	15.73	1882.7	90.57	107
303-19	0.11587	0.00195	0.30311	0.00427	4.84238	0.08915	0.29487	0.0164	0.70106	1893.5	29.9	1706.7	21.1	1792.3	15.49	5223.1	255.94	100

Appendix 2 A
Zircon LA-ICPMS U-Pb Geochronology Analyses

IGC31	Isotope Ratios									Ages (Ma)								
Spot Name	Pb207/Pb206	± 1σ	Pb206/U238	± 1σ	Pb207/U235	± 1σ	Pb208/Th232	± 1σ	rho	Pb207/Pb206	± 1σ	Pb206/U238	± 1σ	Pb207/U235	± 1σ	Pb208/Th232	± 1σ	Conc. (%)
032-01	0.16796	0.00172	0.2599	0.00339	6.01664	0.07819	0.04185	0.0004	0.996331	2537.4	17.12	1489.3	17.32	1978.3	11.31	828.7	7.8	59
032-02	0.15334	0.00158	0.19894	0.00257	4.20497	0.05436	0.02195	0.00022	0.999297	2383.5	17.47	1169.6	13.82	1675	10.6	438.8	4.37	49
032-03	0.14947	0.00152	0.2029	0.00254	4.18014	0.05227	0.02379	0.00024	0.998872	2339.9	17.33	1190.9	13.61	1670.1	10.25	475.3	4.73	51
032-04	0.17492	0.00184	0.41384	0.00523	9.97682	0.12703	0.05856	0.00059	0.992556	2605.3	17.39	2232.5	23.84	2432.6	11.75	1150.3	11.24	86
032-05	0.16981	0.00177	0.48102	0.0061	11.25745	0.14361	0.12125	0.00138	0.994082	2555.8	17.32	2531.7	26.56	2544.7	11.9	2313.1	24.86	99
032-06	0.17049	0.00176	0.40012	0.00504	9.40198	0.11884	0.09575	0.00098	0.996545	2562.4	17.19	2169.6	23.21	2378	11.6	1848.2	18.08	85
032-07	0.16387	0.00165	0.25163	0.00322	5.68255	0.07219	0.03099	0.00029	0.992751	2495.9	16.84	1446.9	16.57	1928.7	10.97	616.8	5.71	58
032-08	0.14842	0.0015	0.18538	0.00239	3.79177	0.04853	0.00237	0.00003	0.992735	2327.8	17.2	1096.3	12.98	1591	10.28	47.8	0.53	47
032-09	0.17267	0.00201	0.38477	0.00529	9.15197	0.1312	0.09584	0.00124	0.959037	2583.7	19.29	2098.5	24.62	2353.3	13.12	1849.9	22.91	81
032-10	0.17026	0.00191	0.34769	0.00496	8.15514	0.11856	0.05114	0.00069	0.981257	2560.2	18.69	1923.5	23.71	2248.4	13.15	1008.1	13.28	75
032-11	0.16916	0.00177	0.29722	0.00375	6.92712	0.0882	0.0295	0.00033	0.990917	2549.3	17.44	1677.5	18.65	2102.1	11.3	587.7	6.47	66
032-12	0.16657	0.00189	0.24797	0.00337	5.68944	0.07997	0.03224	0.00045	0.966881	2523.5	18.92	1428	17.39	1929.8	12.14	641.3	8.82	57
032-13	0.16049	0.00166	0.26957	0.00357	5.96079	0.07908	0.02377	0.00023	0.998237	2460.9	17.34	1538.6	18.14	1970.1	11.54	474.8	4.49	63
032-14	0.20195	0.00208	0.27314	0.00364	7.59954	0.10118	0.02544	0.00024	0.999059	2842	16.68	1556.7	18.43	2184.8	11.95	507.8	4.76	55
032-15	0.14581	0.00156	0.26351	0.00351	5.29398	0.07177	0.03068	0.00032	0.982538	2297.4	18.3	1507.8	17.91	1867.9	11.58	610.9	6.32	66
032-16	0.18196	0.00194	0.24481	0.00319	6.13705	0.08092	0.02041	0.00021	0.988247	2670.9	17.59	1411.6	16.5	1995.5	11.51	408.4	4.17	53
032-17	0.16674	0.00181	0.38689	0.00498	8.88869	0.11676	0.06275	0.00063	0.979908	2525.2	18.11	2108.4	23.17	2326.6	11.99	1230	11.93	83
032-18	0.17785	0.0019	0.32559	0.00424	7.97872	0.1054	0.02344	0.00026	0.985797	2632.9	17.66	1817	20.61	2228.6	11.92	468.3	5.17	69
032-19	0.16792	0.00175	0.43867	0.00557	10.15765	0.12812	0.11998	0.00133	0.993359	2537	17.38	2344.7	24.96	2449.2	11.66	2290.3	24.01	92
032-20	0.1485	0.00162	0.31899	0.0042	6.52971	0.08678	0.05783	0.00059	0.99071	2328.7	18.62	1784.8	20.54	2049.9	11.7	1136.4	11.23	77
032-21	0.13675	0.00139	0.23672	0.00306	4.46241	0.05704	0.01146	0.00012	0.988834	2186.4	17.53	1369.6	15.96	1724	10.6	230.3	2.46	63
032-22	0.14395	0.0016	0.15089	0.0021	2.99435	0.04193	0.02877	0.00034	0.993886	2275.2	19.03	905.9	11.74	1406.2	10.66	573.2	6.75	40
032-23	0.17087	0.00183	0.43893	0.00574	10.33921	0.13498	0.0935	0.00103	0.99831	2566.2	17.84	2345.8	25.7	2465.6	12.09	1806.7	19.05	91
032-24	0.17418	0.00184	0.34788	0.00457	8.3528	0.10926	0.06275	0.00064	0.995732	2598.3	17.54	1924.5	21.85	2270.1	11.86	1230.1	12.18	74
032-25	0.13635	0.00142	0.12868	0.00173	2.41922	0.03236	0.007	0.00008	0.994943	2181.3	17.95	780.3	9.88	1248.3	9.61	141	1.53	36
032-26	0.16936	0.00188	0.45135	0.00617	10.53989	0.14528	0.08927	0.00099	0.991749	2551.3	18.49	2401.3	27.39	2483.4	12.78	1728.3	18.42	94
032-27	0.16809	0.00172	0.28346	0.00365	6.56665	0.08413	0.05178	0.00052	0.994961	2538.7	17.03	1608.8	18.31	2054.9	11.29	1020.4	9.92	63
032-28	0.13827	0.00142	0.26312	0.0035	5.01528	0.06638	0.01319	0.00017	0.995011	2205.6	17.74	1505.8	17.84	1821.9	11.21	264.8	3.39	68
032-29	0.16265	0.00188	0.43495	0.00655	9.75571	0.14939	0.10822	0.00164	0.983421	2483.4	19.38	2328	29.41	2412	14.1	2076.9	29.83	94
032-30	0.15373	0.00169	0.34205	0.00459	7.24902	0.09936	0.06443	0.00101	0.979018	2387.8	18.59	1896.5	22.05	2142.6	12.23	1262.1	19.21	79
032-31	0.17177	0.00185	0.49609	0.00643	11.74195	0.15445	0.14281	0.00202	0.985378	2575	17.86	2597	27.7	2584	12.31	2698.1	35.79	101
032-32	0.16713	0.00178	0.21156	0.00299	4.86944	0.06928	0.04901	0.0007	0.993365	2529.1	17.77	1237.1	15.91	1797	11.98	967	13.49	49
032-33	0.19401	0.00232	0.48008	0.00697	12.83546	0.19284	0.15012	0.00241	0.966348	2776.4	19.44	2527.6	30.37	2667.6	14.15	2826.9	42.37	91
032-34	0.12736	0.00147	0.35624	0.00499	6.25288	0.09124	0.12095	0.00203	0.959959	2061.8	20.23	1964.3	23.73	2011.9	12.77	2307.7	36.67	95
032-35	0.14781	0.00155	0.21557	0.00304	4.39196	0.06193	0.02183	0.0003	0.999902	2320.7	17.89	1258.4	16.11	1710.8	11.66	436.4	5.95	54
032-36	0.15134	0.00156	0.27964	0.00398	5.83335	0.08255	0.05186	0.00065	0.994295	2361.2	17.44	1589.5	20.05	1951.4	12.27	1022	12.47	67
032-37	0.15575	0.00162	0.29178	0.00409	6.26417	0.08738	0.04614	0.00058	0.995132	2410	17.53	1650.4	20.41	2013.5	12.21	911.7	11.18	68
032-38	0.13797	0.00155	0.26505	0.00393	5.04138	0.07629	0.04907	0.00082	0.979821	2201.9	19.41	1515.6	20.05	1826.3	12.82	968.3	15.73	69

Appendix 2 A
Zircon LA-ICPMS U-Pb Geochronology Analyses

IGC44	Isotope Ratios									Ages (Ma)								
Spot Name	Pb207/Pb206	± 1σ	Pb206/U238	± 1σ	Pb207/U235	± 1σ	Pb208/Th232	± 1σ	rho	Pb207/Pb206	± 1σ	Pb206/U238	± 1σ	Pb207/U235	± 1σ	Pb208/Th232	± 1σ	Conc. (%)
044-01	0.17833	0.00275	0.50474	0.00718	12.40817	0.21694	0.12674	0.00584	0.813626	2637.4	25.37	2634.1	30.77	2635.8	16.43	2411.9	104.78	100
044-02	0.17921	0.00263	0.47906	0.00659	11.8356	0.19705	0.12575	0.00547	0.826246	2645.6	24.19	2523.2	28.73	2591.5	15.59	2394.2	98.17	95
044-03	0.17864	0.00265	0.47457	0.00654	11.68727	0.19513	0.06793	0.00292	0.825404	2640.2	24.45	2503.6	28.59	2579.7	15.62	1328.5	55.19	95
044-04	0.16463	0.00242	0.48097	0.00627	10.91641	0.17614	0.12112	0.00542	0.807926	2503.8	24.52	2531.5	27.3	2516	15.01	2310.8	97.74	101
044-05	0.16026	0.00267	0.45802	0.00598	10.11977	0.17825	0.13114	0.00712	0.741238	2458.5	27.93	2430.8	26.46	2445.8	16.28	2490.6	127.18	99
044-06	0.18139	0.00313	0.5158	0.0068	12.89855	0.23332	0.11876	0.00665	0.728814	2665.6	28.27	2681.3	28.92	2672.3	17.05	2268.2	120.12	101
044-07	0.16391	0.00261	0.44283	0.00609	10.00639	0.17558	0.08829	0.0044	0.783759	2496.4	26.55	2363.3	27.23	2435.4	16.2	1710.2	81.81	95
044-08	0.16382	0.0026	0.48394	0.00665	10.9299	0.19163	0.12149	0.00609	0.783759	2495.5	26.5	2544.4	28.9	2517.2	16.31	2317.5	109.81	102
044-09	0.15345	0.00263	0.44834	0.00639	9.48445	0.1779	0.13643	0.00802	0.759853	2384.7	28.86	2387.9	28.45	2386	17.23	2585	142.71	100
044-10	0.16826	0.00282	0.1182	0.00167	2.74172	0.05045	0.17926	0.00979	0.767823	2540.4	27.83	720.2	9.62	1339.8	13.69	3332.7	167.76	28
044-11	0.15493	0.00256	0.45697	0.00629	9.76089	0.17603	0.12606	0.00675	0.763248	2401.1	27.81	2426.2	27.84	2412.5	16.61	2399.6	121.19	101
044-13	0.1801	0.00217	0.5056	0.00664	12.55398	0.1797	0.13335	0.0037	0.892016	2653.7	19.81	2637.8	28.44	2646.8	13.46	2530	65.94	97
044-14	0.16257	0.00271	0.46963	0.00721	10.52478	0.20105	0.12027	0.00584	0.917475	2482.6	27.83	2482	31.62	2482.1	17.71	2295.4	105.38	99
044-15	0.16281	0.00226	0.47917	0.00671	10.75525	0.17489	0.12273	0.0047	0.80369	2485	23.17	2523.6	29.23	2502.2	15.11	2339.8	84.53	100
044-16	0.16582	0.00215	0.46754	0.00618	10.68903	0.15987	0.14999	0.0048	0.861169	2515.9	21.62	2472.8	27.16	2496.5	13.89	2824.6	84.34	102
044-17	0.16223	0.00207	0.46847	0.00606	10.47828	0.15385	0.10477	0.00349	0.883774	2479	21.36	2476.8	26.62	2478	13.61	2014	63.77	98
044-18	0.16309	0.00214	0.46901	0.00615	10.5459	0.15866	0.1111	0.00387	0.881015	2487.9	21.93	2479.2	26.99	2484	13.95	2129.4	70.42	100
044-19	0.16873	0.0023	0.23481	0.00317	5.46251	0.08591	0.09594	0.00347	0.871584	2545.1	22.64	1359.7	16.57	1894.7	13.5	1851.7	64.02	100
044-20	0.15388	0.00266	0.40977	0.00599	8.69376	0.16675	0.10005	0.00546	0.858403	2389.4	29.18	2213.9	27.39	2306.4	17.47	1927.3	100.4	53
044-21	0.12921	0.00186	0.21224	0.00279	3.78121	0.06049	0.02624	0.00111	0.762129	2087.3	25.1	1240.7	14.82	1588.8	12.85	523.5	21.94	93
044-22	0.14037	0.00198	0.2443	0.00325	4.72811	0.07528	0.03054	0.0012	0.821721	2231.8	24.16	1409	16.85	1772.2	13.34	608.1	23.62	59
044-23	0.1703	0.00221	0.29598	0.00385	6.94931	0.10326	0.2183	0.00711	0.835541	2560.6	21.51	1671.4	19.14	2105	13.19	3991	117.91	63
044-24	0.2071	0.00375	0.17089	0.0023	4.87923	0.09215	1.05603	0.06293	0.875403	2883	29.14	1017	12.66	1798.7	15.92	******	618.67	65
044-25	0.07274	0.03362	0.43255	0.045	4.33702	1.98018	0.29523	0.14606	0.712635	1006.8	731.24	2317.2	202.49	1700.4	376.74	5228.7	2279.31	35
044-26	0.15861	0.00212	0.4451	0.0059	9.73297	0.14914	0.11423	0.00394	0.227857	2440.9	22.43	2373.4	26.33	2409.8	14.11	2186.2	71.55	230
044-27	0.14586	0.00195	0.41299	0.00545	8.30499	0.12732	0.10685	0.00384	0.865059	2297.9	22.79	2228.6	24.86	2264.9	13.89	2051.9	70.2	97
044-28	0.16519	0.00238	0.43682	0.00609	9.94832	0.1652	0.1077	0.00425	0.860794	2509.5	24.04	2336.4	27.34	2430	15.32	2067.5	77.55	97
044-29	0.17883	0.00246	0.4903	0.00649	12.08834	0.18847	0.12183	0.00454	0.839565	2642.1	22.7	2572	28.09	2611.3	14.62	2323.6	81.86	93
044-30	0.14332	0.00195	0.34538	0.00459	6.82425	0.10615	0.22282	0.00869	0.848999	2267.7	23.3	1912.5	21.97	2088.9	13.78	4066	143.62	97
044-31	0.17291	0.00232	0.30323	0.00398	7.2287	0.11014	0.02627	0.00094	0.854379	2586	22.19	1707.3	19.69	2140.1	13.59	524.1	18.49	84
044-32	0.15197	0.00213	0.41225	0.00545	8.63738	0.13588	0.11462	0.0045	0.861442	2368.2	23.67	2225.2	24.9	2300.5	14.32	2193.4	81.55	66
044-33	0.16203	0.00249	0.39498	0.00558	8.82398	0.15175	0.09043	0.00391	0.840354	2476.9	25.74	2145.9	25.77	2320	15.68	1749.9	72.48	94
044-34	0.16402	0.00225	0.45166	0.00611	10.21405	0.16097	0.10039	0.00373	0.821476	2497.5	22.93	2402.6	27.13	2454.4	14.58	1933.7	68.58	87
044-35	0.16776	0.00222	0.4773	0.00626	11.04007	0.16676	0.1135	0.00395	0.858386	2535.5	22.04	2515.5	27.33	2526.5	14.06	2173	71.73	96
044-36	0.15304	0.00211	0.31967	0.00424	6.74522	0.10511	0.09221	0.0035	0.868286	2380.2	23.25	1788.1	20.69	2078.6	13.78	1782.8	64.7	99
044-37	0.17249	0.0025	0.46574	0.00611	11.07637	0.17716	0.15074	0.00632	0.85117	2582	23.99	2464.8	26.89	2529.6	14.9	2838	111	75
044-38	0.16947	0.0025	0.46418	0.00619	10.84591	0.17645	0.11697	0.0049	0.820218	2552.4	24.46	2458	27.26	2510	15.12	2235.8	88.75	95
044-39	0.15896	0.00231	0.45253	0.00606	9.91796	0.16095	0.11052	0.0046	0.819688	2444.7	24.38	2406.5	26.89	2427.2	14.97	2118.8	83.76	96
044-40	0.15855	0.00231	0.26265	0.00348	5.74132	0.09294	0.11911	0.00504	0.825195	2440.2	24.49	1503.4	17.76	1937.6	14	2274.5	90.98	98
044-41	0.14848	0.00191	0.41843	0.00572	8.56574	0.13127	0.14606	0.005	0.818485	2328.5	21.92	2253.3	25.98	2292.9	13.93	2755.5	88.26	62
044-41	0.15439	0.0022	0.43798	0.00581	9.32276	0.149	0.11975	0.00483	0.830004	2395.1	24.06	2341.6	26.07	2370.3	14.66	2286	87.19	98
044-42	0.1617	0.00251	0.41481	0.00559	9.24769	0.15713	0.12422	0.00582	0.793116	2473.5	25.93	2236.9	25.45	2362.8	15.57	2366.6	104.6	90

Appendix 2 B

Monazite U-Pb LA-ICPMS Analyses

IGC24	Isotope Ratios							Ages (Ma)						
Spot Name	b207/Pb20	± 1σ	Pb206/U23	± 1σ	Pb207/U23	± 1σ	rho	b207/Pb20	± 1σ	Pb206/U23	± 1σ	Pb207/U23	± 1σ	Conc. (%)
109	0.10454	0.00108	0.29751	0.0042	4.31189	0.06107	0.996753	1706.3	18.86	1679	20.88	1695.6	11.67	101
140	0.11471	0.00118	0.32362	0.00473	5.12384	0.07465	0.996801	1875.3	18.41	1807.4	23.04	1840.1	12.38	102
189core	0.1049	0.00105	0.29958	0.00436	4.33179	0.06181	0.980432	1712.5	18.26	1689.2	21.61	1699.4	11.77	101
189rim	0.10557	0.00107	0.31857	0.00465	4.63586	0.06681	0.987332	1724.3	18.55	1782.8	22.74	1755.7	12.04	98
76a	0.10456	0.00108	0.3051	0.00446	4.39946	0.064	0.995149	1706.6	18.85	1716.5	22.01	1712.2	12.04	100
76b	0.1279	0.00132	0.32881	0.00481	5.79777	0.08423	0.993129	2069.3	18.07	1832.6	23.36	1946.1	12.58	106

IGC29	Isotope Ratios							Ages (Ma)						
Spot Name	b207/Pb20	± 1σ	Pb206/U23	± 1σ	Pb207/U23	± 1σ	rho	b207/Pb20	± 1σ	Pb206/U23	± 1σ	Pb207/U23	± 1σ	Conc. (%)
1809028_1	0.10516	0.00106	0.29916	0.0046	4.3358	0.06572	0.985766	1717.1	18.33	1687.1	22.81	1700.2	12.51	101
1809028_1	0.10486	0.0011	0.30566	0.00477	4.41705	0.06909	0.997693	1711.8	19.14	1719.3	23.56	1715.5	12.95	100
1809028_1	0.10542	0.00106	0.29989	0.00462	4.35699	0.06623	0.986707	1721.7	18.38	1690.8	22.9	1704.2	12.55	101
1809028_1	0.10501	0.00106	0.29723	0.00459	4.30146	0.06556	0.986968	1714.5	18.49	1677.6	22.8	1693.6	12.56	101
1809028_1	0.10557	0.00111	0.31342	0.0049	4.55977	0.07153	0.996607	1724.2	19.24	1757.5	24.03	1741.9	13.06	99
1809028_1	0.10469	0.00113	0.31289	0.00486	4.51451	0.07096	0.988193	1708.9	19.76	1754.9	23.88	1733.6	13.07	99
1809028_1	0.10393	0.00123	0.30727	0.0048	4.40065	0.07143	0.962404	1695.5	21.62	1727.3	23.65	1712.5	13.43	99
1809028_1	0.10514	0.0011	0.30524	0.00477	4.42279	0.06903	0.998768	1716.7	19.08	1717.3	23.54	1716.6	12.93	100
1809028_1	0.10413	0.00114	0.30431	0.00478	4.3671	0.06999	0.980096	1699	20.11	1712.7	23.63	1706.1	13.24	100
1809028_1	0.10449	0.00114	0.30435	0.00473	4.38276	0.06898	0.987444	1705.4	20	1712.8	23.36	1709.1	13.01	100
1809028_1	0.10445	0.00113	0.30045	0.00468	4.32481	0.06828	0.986614	1704.6	19.83	1693.5	23.2	1698.1	13.02	100
1809028_1	0.10466	0.00109	0.30871	0.00477	4.45315	0.06856	0.996405	1708.4	19.09	1734.4	23.47	1722.3	12.77	99
1809028_3	0.10472	0.00113	0.30406	0.00475	4.38862	0.06954	0.985888	1709.5	19.76	1711.4	23.5	1710.2	13.1	100
1809028_3	0.10449	0.00118	0.30998	0.00486	4.46378	0.07181	0.974587	1705.3	20.57	1740.6	23.91	1724.3	13.35	99
1809028_8	0.10385	0.00118	0.30561	0.00478	4.37378	0.07058	0.96925	1694	20.82	1719.1	23.62	1707.4	13.34	99
1809028_A	0.10427	0.00106	0.29739	0.00462	4.27275	0.06576	0.990692	1701.4	18.61	1678.3	22.95	1688.1	12.66	101
1809028_A	0.10502	0.00107	0.29953	0.00464	4.33488	0.0666	0.991789	1714.7	18.56	1689	23.02	1700	12.68	101
1809028_A	0.10489	0.00108	0.31403	0.00485	4.53916	0.06952	0.991662	1712.4	18.78	1760.5	23.77	1738.2	12.74	99
1809028_A	0.10449	0.00106	0.29869	0.00461	4.30101	0.06553	0.987164	1705.4	18.51	1684.8	22.86	1693.6	12.55	101
1809028_E	0.10549	0.00111	0.30263	0.00473	4.39971	0.06908	0.995453	1722.9	19.22	1704.4	23.4	1712.3	12.99	100
1809028_E	0.10537	0.00111	0.30519	0.00476	4.43189	0.06956	0.993725	1720.8	19.25	1717	23.53	1718.3	13	100
1809028_E	0.10425	0.00111	0.30301	0.00474	4.35347	0.06847	0.994619	1701	19.46	1706.2	23.43	1703.6	12.99	100
1809028_E	0.10453	0.00113	0.30164	0.00472	4.34526	0.06885	0.987563	1706	19.83	1699.4	23.37	1702	13.08	100
BC105	0.1044	0.00134	0.30182	0.0044	4.3435	0.06964	0.909255	1703.8	23.36	1700.3	21.8	1701.7	13.23	100
BC106	0.1045	0.0015	0.3023	0.00451	4.35417	0.07551	0.860279	1705.6	26.21	1702.7	22.32	1703.7	14.32	100
BC109A	0.10498	0.00143	0.30595	0.00449	4.42788	0.0737	0.881707	1714	24.86	1720.7	22.15	1717.6	13.79	100
BC109B	0.10547	0.00132	0.38617	0.00555	5.61677	0.08815	0.915754	1722.6	22.84	2105	25.8	1918.7	13.53	91
BC110	0.10446	0.00143	0.30664	0.0045	4.41582	0.0737	0.879281	1704.8	24.92	1724.1	22.2	1715.3	13.82	99
BC112	0.10523	0.00161	0.31562	0.00474	4.5774	0.08297	0.828536	1718.4	27.9	1768.3	23.24	1745.2	15.1	99
BC123	0.10488	0.0015	0.30822	0.0046	4.45542	0.07727	0.860547	1712.2	26.12	1732	22.65	1722.7	14.38	99
BC24	0.10342	0.00124	0.30206	0.00437	4.30541	0.0663	0.939484	1686.4	21.99	1701.5	21.63	1694.4	12.69	100

Appendix 2 B

Monazite U-Pb LA-ICPMS Analyses

BC27	0.1038	0.00145	0.30173	0.00448	4.31647	0.07334	0.873871	1693.1	25.53	1699.9	22.2	1696.5	14.01	100
BC36	0.1058	0.00156	0.30411	0.00455	4.4343	0.07789	0.851773	1728.3	26.77	1711.6	22.51	1718.8	14.55	100
BC37	0.10543	0.0014	0.30875	0.00457	4.48638	0.07425	0.894353	1721.9	24.24	1734.6	22.49	1728.5	13.74	100
BC37B	0.10474	0.00151	0.30622	0.00459	4.42004	0.07675	0.863231	1709.7	26.37	1722.1	22.66	1716.1	14.38	100
BC39	0.10579	0.00139	0.31327	0.00462	4.56727	0.07496	0.898567	1728.1	23.86	1756.8	22.66	1743.3	13.67	99
BC46	0.10404	0.00128	0.29777	0.00427	4.27098	0.06611	0.926419	1697.4	22.48	1680.2	21.2	1687.8	12.74	100
BC69	0.10419	0.00137	0.306	0.0045	4.39401	0.07228	0.893993	1700	24.11	1721	22.19	1711.2	13.61	99
BC8	0.10445	0.00121	0.30547	0.00434	4.39782	0.06553	0.953495	1704.7	21.12	1718.4	21.41	1711.9	12.33	100
BC86	0.10359	0.00132	0.30342	0.00442	4.33236	0.06922	0.91174	1689.3	23.24	1708.2	21.86	1699.5	13.18	99

BC 2011-01	Isotope Ratios							Ages (Ma)						
Spot Name	b207/Pb20	± 1σ	Pb206/U23	± 1σ	Pb207/U23	± 1σ	rho	b207/Pb20	± 1σ	Pb206/U23	± 1σ	Pb207/U23	± 1σ	Conc. (%)
859-01	0.10442	0.00127	0.29718	0.00439	4.27632	0.06787	0.930759	1704.1	22.23	1677.3	21.84	1688.8	13.06	101
859-02	0.10529	0.00124	0.29738	0.00444	4.31509	0.06831	0.943141	1719.4	21.56	1678.3	22.06	1696.2	13.05	101
859-03	0.10529	0.00128	0.29731	0.00444	4.3142	0.06943	0.927954	1719.4	22.24	1678	22.09	1696.1	13.27	101

CG01	Isotope Ratios							Ages (Ma)						
Spot Name	b207/Pb20	± 1σ	Pb206/U23	± 1σ	Pb207/U23	± 1σ	rho	b207/Pb20	± 1σ	Pb206/U23	± 1σ	Pb207/U23	± 1σ	Conc. (%)
69a1	0.10516	0.00104	0.3248	0.00498	4.71069	0.0703	0.973324	1717.2	18.02	1813.1	24.22	1769.1	12.5	98
69a2	0.10314	0.00101	0.32332	0.00497	4.59777	0.06863	0.971053	1681.3	17.99	1805.9	24.23	1748.9	12.45	97
70a1	0.1028	0.001	0.3126	0.0048	4.43246	0.06547	0.961934	1675.2	17.88	1753.5	23.56	1718.4	12.24	98
70a2	0.10236	0.00099	0.31599	0.00484	4.46093	0.06561	0.960224	1667.4	17.83	1770.1	23.73	1723.7	12.2	97
cg0149	0.10513	0.00105	0.31259	0.00476	4.53443	0.06774	0.981049	1716.6	18.32	1753.4	23.39	1737.3	12.43	99
cg014a	0.10658	0.00106	0.35365	0.00541	5.2158	0.07815	0.979455	1741.7	18.17	1952	25.77	1855.2	12.77	95
cg0150a	0.10328	0.00102	0.32601	0.00495	4.6684	0.06895	0.972729	1683.8	18.07	1819	24.06	1761.6	12.35	97
cg0152	0.1051	0.00103	0.32834	0.00497	4.7777	0.0699	0.966553	1716.1	17.96	1830.4	24.14	1781	12.28	97
cg0152a	0.10459	0.00108	0.30687	0.00472	4.4301	0.06715	0.985473	1707.2	18.89	1725.3	23.26	1718	12.56	100
cg0159a	0.10374	0.00103	0.30349	0.00457	4.34063	0.06361	0.973197	1692	18.11	1708.6	22.62	1701.1	12.09	100
cg0159b	0.10406	0.00115	0.29387	0.00452	4.2186	0.06486	0.999598	1697.8	20.23	1660.8	22.52	1677.6	12.62	101
cg0159c	0.10476	0.00104	0.31647	0.0048	4.57249	0.06718	0.968676	1710.2	18.1	1772.5	23.52	1744.3	12.24	98
cg0171a	0.10509	0.00103	0.3278	0.00497	4.75045	0.06964	0.966889	1715.9	17.93	1827.7	24.14	1776.2	12.3	97
cg0173a	0.10257	0.001	0.32901	0.00512	4.65259	0.06962	0.961564	1671.1	17.95	1833.6	24.85	1758.8	12.51	96
cg0173b	0.1023	0.00107	0.31465	0.00493	4.43536	0.06829	0.982673	1666.3	19.16	1763.5	24.15	1719	12.76	97
cg0174x1	0.10301	0.00101	0.31625	0.00489	4.49225	0.06726	0.96831	1679.1	18.08	1771.4	23.93	1729.5	12.44	98
cg0174x2	0.10408	0.00101	0.31199	0.00481	4.47942	0.06673	0.966262	1698.2	17.85	1750.5	23.64	1727.2	12.37	99

BP 2011-00	Isotope Ratios							Ages (Ma)						
Spot Name	b207/Pb20	± 1σ	Pb206/U23	± 1σ	Pb207/U23	± 1σ	rho	b207/Pb20	± 1σ	Pb206/U23	± 1σ	Pb207/U23	± 1σ	Conc. (%)
843-01	0.10756	0.00114	0.30554	0.00493	4.52865	0.07374	0.990933	1758.5	19.24	1718.7	24.35	1736.2	13.54	101
843-02	0.13793	0.00181	0.4373	0.00721	8.30891	0.14548	0.941665	2201.4	22.62	2338.6	32.34	2265.3	15.87	97
843-03	0.10711	0.00109	0.30941	0.00496	4.56698	0.07335	0.998105	1750.9	18.47	1737.8	24.43	1743.3	13.38	100
843-04	0.10718	0.00109	0.30742	0.00498	4.54027	0.0737	0.997956	1752	18.5	1728	24.53	1738.4	13.51	101
843-05	0.10643	0.00108	0.31607	0.00506	4.63518	0.074	0.997236	1739.2	18.45	1770.5	24.78	1755.6	13.33	99

843-06	0.10588	0.00111	0.30462	0.00489	4.44468	0.07226	0.9874	1729.7	19.2	1714.2	24.15	1720.7	13.48	100
843-07	0.10611	0.00114	0.30756	0.00495	4.49692	0.07362	0.983093	1733.6	19.54	1728.7	24.43	1730.4	13.6	100
843-08	0.15169	0.00278	0.46268	0.00829	9.67238	0.20337	0.852158	2365.1	30.98	2451.4	36.55	2404.1	19.35	98
843-09	0.10715	0.00109	0.31335	0.00502	4.62668	0.07428	0.997865	1751.5	18.5	1757.2	24.62	1754.1	13.4	100
843-10	0.10682	0.0012	0.30389	0.00486	4.47331	0.07426	0.963372	1745.9	20.35	1710.6	24.03	1726	13.78	101

SP6	Isotope Ratios							Ages (Ma)						
Spot Name	b207/Pb20	± 1σ	Pb206/U23	± 1σ	Pb207/U23	± 1σ	rho	b207/Pb20	± 1σ	Pb206/U23	± 1σ	Pb207/U23	± 1σ	Conc. (%)
SP6-01	0.10502	0.00126	0.29939	0.00473	4.33354	0.07157	0.956612	1714.7	21.89	1688.3	23.47	1699.8	13.63	101
SP6-02	0.1048	0.00133	0.30062	0.00478	4.34186	0.07349	0.939415	1710.7	23.11	1694.4	23.67	1701.3	13.97	100
SP6-03	0.10714	0.00146	0.29286	0.00471	4.32371	0.07604	0.914482	1751.3	24.74	1655.8	23.47	1697.9	14.5	103
SP6-04	0.10339	0.00202	0.30072	0.00523	4.28414	0.09419	0.79104	1685.8	35.57	1694.9	25.91	1690.3	18.1	100
SP6-05	0.10535	0.00185	0.30008	0.00502	4.35628	0.08824	0.82588	1720.4	31.92	1691.7	24.89	1704.1	16.73	101
SP6-06	0.10368	0.00185	0.30572	0.00514	4.36665	0.08946	0.820651	1691.1	32.56	1719.6	25.38	1706.1	16.93	99
SP6-07	0.10539	0.00137	0.2971	0.00474	4.31537	0.07408	0.929379	1721.2	23.66	1676.9	23.56	1696.3	14.15	101
SP6-08	0.10537	0.00143	0.30255	0.00493	4.39298	0.078	0.917729	1720.7	24.74	1703.9	24.38	1711	14.69	100
SP6-09	0.10537	0.0014	0.30148	0.00496	4.37713	0.07806	0.922538	1720.8	24.3	1698.6	24.56	1708	14.74	101
SP6-10	0.10578	0.00131	0.29774	0.00484	4.33977	0.07461	0.945536	1727.9	22.57	1680.1	24.03	1701	14.19	101
SP6-11	0.10673	0.0013	0.29212	0.00467	4.29623	0.07233	0.949565	1744.3	22.06	1652.1	23.31	1692.6	13.87	102
SP6-12	1.27074	1.21994	-3.25804	4.45402	*********	637.9166	#VALUE!	5571.9	919.41	-NaN	*******	-NaN	*******	#VALUE!
SP6-13	0.10502	0.00139	0.29657	0.00484	4.29162	0.0759	0.922779	1714.8	24.08	1674.3	24.04	1691.8	14.56	101
SP6-14	0.10881	0.00185	0.29582	0.00495	4.43331	0.08838	0.839367	1779.5	30.73	1670.6	24.63	1718.6	16.52	103
SP6-15	0.10465	0.00133	0.29235	0.00476	4.21551	0.07361	0.932432	1708.2	23.13	1653.3	23.76	1677	14.33	101
SP6-16	0.1048	0.00116	0.30177	0.00481	4.35802	0.07124	0.975067	1710.8	20.17	1700.1	23.83	1704.4	13.5	100
SP6-17	0.10476	0.00132	0.29386	0.00475	4.24205	0.07317	0.937121	1710.2	23.06	1660.8	23.67	1682.2	14.17	101
SP6-18	0.10387	0.00125	0.29806	0.00481	4.26618	0.07255	0.94895	1694.4	22.07	1681.7	23.9	1686.9	13.99	100
SP6-19	0.1047	0.00136	0.29997	0.00483	4.32864	0.07502	0.92906	1709.1	23.63	1691.2	23.93	1698.8	14.29	100
SP6-20	0.10481	0.00147	0.29814	0.00483	4.30418	0.07727	0.902415	1711	25.64	1682.1	23.98	1694.2	14.79	101
SP6-21	0.10701	0.00127	0.29589	0.00479	4.36304	0.07369	0.958486	1749.1	21.42	1670.9	23.81	1705.4	13.95	102

SP7	Isotope Ratios							Ages (Ma)						
Spot Name	b207/Pb20	± 1σ	Pb206/U23	± 1σ	Pb207/U23	± 1σ	rho	b207/Pb20	± 1σ	Pb206/U23	± 1σ	Pb207/U23	± 1σ	Conc. (%)
SP7-01	0.10439	0.00108	0.30693	0.00458	4.41573	0.06579	0.998461	1703.6	18.87	1725.6	22.59	1715.3	12.34	99
SP7-02	0.10504	0.00105	0.3072	0.00459	4.44708	0.0657	0.988778	1715	18.22	1726.9	22.64	1721.2	12.25	100
SP7-03	0.1045	0.00104	0.30481	0.00454	4.39	0.06436	0.984294	1705.5	18.29	1715.1	22.42	1710.5	12.12	100
SP7-04	0.10375	0.00106	0.30859	0.00465	4.41106	0.06553	0.985885	1692.3	18.76	1733.8	22.89	1714.4	12.3	99
SP7-05	0.10488	0.00105	0.30804	0.00459	4.45251	0.06541	0.985902	1712.2	18.38	1731.1	22.63	1722.2	12.18	99
SP7-06	0.10456	0.00105	0.30902	0.00462	4.45329	0.06574	0.9874	1706.7	18.44	1735.9	22.73	1722.3	12.24	99
SP7-07	0.10437	0.00109	0.30919	0.00466	4.44748	0.06706	0.999565	1703.3	19.19	1736.7	22.96	1721.2	12.5	99
SP7-08	0.10433	0.00107	0.3156	0.00472	4.53793	0.0675	0.994583	1702.5	18.77	1768.2	23.15	1738	12.38	98
SP7-09	0.51148	0.00742	0.75787	0.01347	53.41688	0.9333	0.983037	4274.6	21.17	3636.4	49.41	4058.2	17.41	112
SP7-10	0.10524	0.00106	0.30522	0.00456	4.4268	0.06514	0.984931	1718.4	18.33	1717.1	22.5	1717.4	12.19	100

Appendix 2 B

Monazite U-Pb LA-ICPMS Analyses

SP7-11	0.10558	0.00106	0.30487	0.00456	4.4361	0.06567	0.989727	1724.5	18.37	1715.4	22.54	1719.1	12.27	100
SP7-12	0.10512	0.00106	0.3057	0.00454	4.4282	0.06519	0.991273	1716.5	18.37	1719.5	22.43	1717.6	12.19	100
SP7-13	0.10487	0.00105	0.3068	0.00459	4.43397	0.06552	0.987697	1712	18.29	1725	22.65	1718.7	12.24	100
SP7-14	0.10482	0.00105	0.29996	0.00452	4.33341	0.06447	0.987308	1711.2	18.24	1691.1	22.42	1699.7	12.27	101
SP7-15	0.10553	0.00106	0.30138	0.00455	4.38335	0.0656	0.99129	1723.6	18.42	1698.2	22.55	1709.2	12.37	101
SP7-16	0.1044	0.00105	0.29764	0.00448	4.28241	0.06374	0.988865	1703.7	18.37	1679.6	22.26	1690	12.25	101
SP7-17	0.10543	0.00108	0.31028	0.00461	4.50827	0.06687	0.99833	1721.9	18.74	1742.1	22.66	1732.5	12.33	99

ASE-01	Isotope Ratios							Ages (Ma)						
Spot Name	b207/Pb20	± 1σ	Pb206/U23	± 1σ	Pb207/U23	± 1σ	rho	b207/Pb20	± 1σ	Pb206/U23	± 1σ	Pb207/U23	± 1σ	Conc. (%)
ASE01-01	0.10298	0.00172	0.37141	0.00586	5.27119	0.10061	0.826631	1678.5	30.52	2036	27.53	1864.2	16.29	92
ASE01-02	0.10434	0.00105	0.29449	0.00434	4.23472	0.06218	0.996338	1702.6	18.48	1663.9	21.63	1680.8	12.06	101
ASE01-03	0.10573	0.00109	0.30567	0.00448	4.45397	0.06543	0.99769	1727.1	18.84	1719.3	22.12	1722.4	12.18	100
ASE01-04	0.10366	0.00107	0.30121	0.00442	4.30328	0.06306	0.998623	1690.6	18.92	1697.3	21.88	1694	12.07	100
ASE01-05	0.10428	0.00106	0.29876	0.0044	4.29439	0.06312	0.998011	1701.7	18.62	1685.2	21.86	1692.3	12.11	100
ASE01-06	0.10441	0.00109	0.29895	0.0044	4.30234	0.06359	0.995795	1704	19.09	1686.1	21.85	1693.8	12.18	100
ASE01-07	0.10392	0.00109	0.29854	0.00441	4.27586	0.06348	0.994999	1695.3	19.26	1684	21.88	1688.7	12.22	100
ASE01-08	0.10975	0.00127	0.32188	0.00486	4.86903	0.07476	0.983367	1795.2	20.89	1798.9	23.7	1796.9	12.93	100
ASE01-09	0.10665	0.0011	0.30382	0.00447	4.46549	0.06595	0.996198	1743	18.81	1710.2	22.1	1724.6	12.25	101
ASE01-10	0.10567	0.00108	0.30782	0.00455	4.48275	0.06608	0.997266	1726	18.61	1729.9	22.41	1727.8	12.24	100
ASE01-11	0.10406	0.00104	0.30607	0.00452	4.38944	0.06418	0.990086	1697.8	18.27	1721.4	22.31	1710.4	12.09	99
ASE01-12	0.10451	0.00106	0.29445	0.00437	4.24076	0.06255	0.993834	1705.6	18.52	1663.7	21.75	1681.9	12.12	101
ASE01-13	0.1038	0.00111	0.29863	0.00439	4.27103	0.06383	0.983646	1693.2	19.67	1684.5	21.79	1687.8	12.3	100

Appendix 2 B

Monazite U-Pb LA-ICPMS Analyses

ASE01-14	0.10392	0.00104	0.30107	0.00445	4.31206	0.06326	0.992549	1695.3	18.41	1696.6	22.03	1695.7	12.09	100
ASE01-15	0.10431	0.00109	0.2987	0.00439	4.29399	0.06315	0.999349	1702.2	19.04	1684.9	21.8	1692.2	12.11	100
ASE01-16	0.1019	0.00107	0.30274	0.00446	4.25134	0.06252	0.998224	1659.1	19.3	1704.9	22.08	1684	12.09	99
ASE01-17	0.10391	0.00106	0.29302	0.00432	4.19627	0.06156	0.995059	1695.2	18.69	1656.6	21.54	1673.3	12.03	101
ASE01-18	0.10418	0.00108	0.29459	0.00419	4.22972	0.06054	0.993723	1699.9	18.97	1664.4	20.86	1679.8	11.75	101
ASE01-19	0.10514	0.00106	0.30088	0.00429	4.35999	0.06201	0.997499	1716.9	18.48	1695.7	21.28	1704.8	11.75	101
ASE01-20	0.1042	0.00108	0.30054	0.00432	4.31603	0.06245	0.993421	1700.3	18.94	1694	21.43	1696.4	11.93	100
ASE01-21	0.11268	0.00144	0.30657	0.00457	4.75811	0.07545	0.940073	1843.1	23	1723.8	22.52	1777.5	13.3	103